ulm university universität **u**ulm

Faculty of
Naturwissenschaften
Institute of Quantum
Technologies

Quantum-Enhanced Correction for Improved Magnetic Field-Aided Navigation

Master thesis at Deutsches Zentrum für Luft- und Raumfahrt.
Submitted for the degree of Master of Science (MSc) in Wirtschaftsphysik.

Submitted by:
Christos Papadopoulos
christos.papadopoulos@uni-ulm.de
Matriculation number: 1002523

Thesis advisors:
Prof. Dr. Christian Brand
christian.brand@dlr.de
Institute for Quantum Technologies, DLR

Dr. Kai Bongs
kai.bongs@dlr.de
Institute for Quantum Technologies, DLR

Supervisor:
Dr. Maxime Debiossac
Institute for Quantum Technologies, DLR

Ulm, May 07, 2025

Version May 07, 2025

Contents

List of Abbreviations

AC	Alternating Current. 9, 10, 18, 24
AD	Allan Deviation. 44, 45, 66, 84, 88, 89
ARW	Angle Random Walk. 85, 86
AUV	Autonomous Underwater Vehicle. 2
BI	Bias Instability. 84–86
CM	Classical Magnetometer. 16, 19
DOF	Degrees-of-Freedom. 62
ECEF	Earth-centered Earth-fixed. 34
EMAG2	Earth's Magnetic Anomaly Grid. 62, 63
FID	Free Induction Decay. 21, 22
GNSS	Global Navigation Satellite System. 1, 2
IGRF	International Geomagnetic Reference Field. 26–30, 63
IMU	Inertial Measurement Unit. 3, 32, 35, 36, 48, 52, 53, 57, 60, 64–67, 84, 85, 88, 92, 96, 98, 99, 101, 102, 104
INS	Inertial Navigation System. 1–3, 50–52, 55–58, 63, 73–76, 79, 80, 82, 83, 96, 98, 100, 101, 104, 114, 120–122
KF	Kalman Filter. 2, 37
MAE	Mean Absolute Error. 47, 71–74, 76, 78, 79, 81–83
ME	Maximum Absolute Error. 47

MEMS	Micro-Electro-Mechanical Systems. 31, 32, 92
NED	North-East-Down. 62
NV	Nitrogen Vacancy. 2, 20, 23, 24
ODMR	Optically Detected Magnetic Resonance. 23, 24
OPM	Optically Pumped Magnetometer. 2, 12, 20, 22, 24, 49, 68, 103, 105
PDA	Probabilistic Data Association. 51, 52, 54, 57, 70, 71, 83, 98, 99, 119
PDF	Probability Density Function. 38, 39, 54, 73, 74, 76
PSD	Power Spectral Density. 45, 46, 84, 87, 88, 91
QM	Quantum-based Magnetometer. 16, 44
RMSE	Root-Mean-Square-Error. 47
ROI	Region of Interest. 67, 68, 94, 95
SERF	Spin Exchange Relaxation-Free. 20
SNR	Signal-to-Noise Ratio. 46, 102
SQUID	Superconducting Quantum Interference Device. 20, 24
TE	Total Error. 78, 81, 82
TRN	Terrain Referenced Navigation. 1
UKF	Unscented Kalman Filter. 2–4, 37, 38, 52–54, 56–58, 60, 63, 69, 71–73, 78–80, 83, 99, 102, 104, 105, 113
UT	Unscented Transform. 37, 38, 71
VRW	Velocity Random Walk. 84, 86

1 Introduction

1.1 Background and Motivation

Classical magnetometers are widely used in many devices and applications, serving as essential tools in many critical areas. However, with advances in quantum technology, quantum-based magnetometers are now emerging as a viable alternative. These sensors are evolving rapidly, particularly with advances in quantum engineering and miniaturization, allowing the transition from large laboratory setups to compact, portable devices that are beginning to become commercially available. A variety of applications are of interest for these new types of sensors, particularly in the fields of medical applications [1], geomagnetism and space applications [2]. One particularly interesting application is a navigation system that uses magnetic field maps to aid navigation.

Currently, we rely heavily on Global Navigation Satellite System (GNSS) for positioning and navigation on the Earth's surface. The fusion of Inertial Navigation System (INS) position estimates with time signals from multiple GNSS satellites helps correct the accumulating errors in the INS position. However, GNSS signals are increasingly vulnerable to jamming and spoofing, which is the active transmission of signals to prevent or manipulate position [3]. This is particularly true in conflict areas of the world where these strategies are used for war tactics [4]. This vulnerability is due to the weak signals emitted by satellites [5] and highlights the need for a reliable and robust navigation system that can act as a backup in such regions or further in regions where GNSS is not available.

There are several approaches that exploit the concept of using geophysical maps and measurements to correct for accumulated position errors in INS, creating an unspoofable and unjammable navigation system. This is achieved through the self-sufficient architecture of the navigation system, which uses information from pre-recorded maps and on-board measurements of observable features from the same map, resulting in a navigation system that does not rely on signals from satellites. This includes, in particular, the use of terrain contours in navigation applications, also known as Terrain Referenced Navigation (TRN) [6]. Other approaches include the use of gravitational anomaly maps [7] and geomagnetic anomaly maps for navigation [8]. In particular, the development of quantum-based magnetometers with their promising absolute accuracy and high sensitivity [9] has the potential to significantly improve magnetic field-aided navigation as these promise to reliably measure small field deviations, which are needed for accurate position estimates. This makes them ideal candidates to make magnetic fields a viable option for reliable navigation. Some research has been done on navigation systems that use magnetic fields. Research in this area falls into two main categories: simulations and real-world implementations of this navigation method. This thesis presents both simulation studies and a real-world laboratory experiment on magnetic field-aided navigation. So the following highlights some key work in this area.

The work of Wang *et al.* (2023) [10] on *Quantum Diamond Magnetometry for Navigation in GNSS-Denied Environments* implements simulations using the noise characteristics of Nitrogen Vacancy (NV) diamond magnetometers. It introduces a novel approach to overcome the *map matching problem* and address the positional ambiguity caused by locations with similar magnetic measurements on the map. The fusion of position estimates is performed using an advanced Unscented Kalman Filter (UKF) with forward and backward filtering. The study demonstrates that the iterative forward and backward filtering approach achieves divergence-free navigation by using Monte Carlo simulations on their specified simulated flight path.

Further simulation studies using pre-recorded magnetic anomaly maps have been conducted by Canciani (2016) [8]. His work focuses on the use of anomaly maps of the Earth's magnetic field and includes flight simulations. However, instead of using a Kalman Filter (KF) for navigation, he implements a particle filter. In addition, Canciani conducted real experiments using actual flight data, incorporating a Optically Pumped Magnetometer (OPM) to make scalar intensity measurements of the Earth's magnetic field. The data obtained during the flight was fed into his implemented magnetic field-aided navigation algorithm. Canciani demonstrated navigation accuracy to within a few tens of meters at low altitudes using real flight data and a high-quality magnetic anomaly map that he had pre-recorded. He identified altitude and map quality as the two most critical factors affecting navigation accuracy. In addition, his study showed navigation accuracies within a few kilometers during a cross-country flight simulation at an altitude of $3\mathrm{km}$ across North America.

Quintas *et al.* (2018) [11] explored geomagnetic navigation using submerged magnetometers for Autonomous Underwater Vehicle (AUV) navigation. Two Overhauser magnetometers, spaced $1.5\mathrm{m}$ apart, were used to measure the magnetic field. A magnetic field map was pre-recorded over the area of interest, showing a variability of about $4\mathrm{nT}$ within an area of $600\mathrm{m} \times 600\mathrm{m}$. Three trajectories were used to compare the INS position estimation with a magnetic field-aiding algorithm. Results showed that the magnetic field-assisted solution had a positioning error within $10\mathrm{m}$, compared to around $40\mathrm{m}$ for the INS solution in two of the three trajectories. While errors in the aiding algorithm increased in areas with low magnetic field variability, they recovered in areas with more spatial information, demonstrating its ability to limit position error, unlike INS solutions, which accumulate errors over time.

This thesis aims to take the first steps toward developing and implementing a magnetic field-based navigation system by combining simulation-based approaches with a real-world laboratory experiment. To achieve this, a laboratory experiment was planned and implemented. Prior to conducting the experiment, a simulation of the laboratory setup was created. Additionally, flight path simulations, similar to those by Wang *et al.* (2023) [10], were carried out using a similar approach for the magnetic field-aided navigation algorithm.

1.2 Thesis Overview

This thesis begins by presenting the theoretical background necessary for this work. It introduces the basic principles of magnetism and then briefly outlines selected principles of classical and quantum-based magnetic field sensing. Further, the operating principles of the Inertial Measurement Unit (IMU) are explained, followed by the derivation of position estimation based on the sensed measurements. The associated sources of error are also discussed. The sensor fusion process using the UKF is described in detail. In addition, the method of map interpolation using the *Kriging* algorithm is briefly introduced. The thesis also includes a brief introduction to sensor quantification and performance metrics, followed by a definition of the specific performance metrics used in this thesis.

The third chapter presents the methodology and setup of the work carried out in this thesis. It explains in detail the implemented magnetic field-aided navigation algorithm and describes the two simulation scenarios carried out in this work. It also describes the data acquisition process, the map generation scheme, and the laboratory experiment in which magnetic field-aided navigation is implemented in a real-world setting.

Chapter four presents and discusses the results. First, the results of the simulation approaches are presented, including both the laboratory experiment and the real-life simulations. For the lab experiment, the sensors used are first quantified in terms of drift and noise. The generated maps are then presented and the results of the real-life implementation of the lab experiment are discussed.

The final chapter, chapter five, summarizes the findings of this thesis and provides an outlook on potential future work.

2 Theoretical Background

This chapter presents the theoretical background necessary for this thesis, beginning with an introduction to the basic theory of magnetism and magnetic fields, followed by an overview of classical and quantum-based magnetic field sensing principles.
It then covers the Earth's magnetic field, including its origin, composition, and characteristics. The chapter proceeds to discuss the fundamentals of inertial navigation sensors and how position can be derived from them.
Following this, a brief explanation is provided on how measurements from multiple sensors can be integrated. Specifically, the UKF is introduced as a key component in the navigation aiding algorithm, enabling the combination of position estimates from different sensors to improve accuracy.
An introduction to the *Kriging* interpolation algorithm, used for constructing magnetic field maps in navigation aiding, is then presented.
The chapter concludes with fundamental definitions of sensor metrics, errors, and noise, as well as methods for quantifying them, followed by the definition of performance metrics for evaluating navigation accuracy.

2.1 Magnetic Fields and Magnetism

2.1.1 Magnetism in Classical Physics

The magnetic field is a fundamental physical vector field that is present everywhere around us. It describes the interaction between magnetic materials, moving electric charges, and electric currents. In the following, key phenomena and properties of magnetism are presented. This theoretical background is based on the book *Magnetism and Magnetic Materials* by Coey [12].
A key quantity in magnetism is the magnetic flux density $\boldsymbol{B}$. Magnetic flux density measures the line density that crosses a unit surface area and is given in units of Tesla $[\mathrm{T}]$. Another important measure of the magnetic vector field which is often used interchangeably is the

vector field called the magnetic field strength $\boldsymbol{H}$ $[\mathrm{A/m}]$. Both vector fields $\boldsymbol{B}$ and $\boldsymbol{H}$ are closely related through the following equation:

$$\boldsymbol{H} = \frac{1}{\mu_0}\boldsymbol{B} - \boldsymbol{M}, \tag{2.1}$$

where μ_0 is the vacuum permeability and $\boldsymbol{M}$ is the magnetization vector of the material. The magnetization is the resulting net magnetic field of a material exposed to the magnetic field. The difference between these two vector fields is that the $\boldsymbol{B}$ field accounts for the magnetization of the medium, whereas the $\boldsymbol{H}$ field does not. In vacuum, both $\boldsymbol{B}$ and $\boldsymbol{H}$ are proportional to each other as the magnetization $\boldsymbol{M}$ of vacuum is zero.

Although $\boldsymbol{B}$ represents typically the magnetic flux density, in the remainder of this thesis, the external magnetic field will be denoted as $\boldsymbol{B}$, since magnetic flux density is often interchangeable with the magnetic field's magnitude.

The magnetic field strength $\boldsymbol{B}$ is proportional to the magnetizing force, which determines how materials respond to magnetic fields. The force experienced by a moving charge q within the magnetic field $\boldsymbol{B}$ is known as the *Lorentz* force $\boldsymbol{F}_{Lor.}$ and is given by:

$$\boldsymbol{F}_{Lor.} = q\left(\boldsymbol{v} \times \boldsymbol{B}\right) \,, \tag{2.2}$$

where $\boldsymbol{v}$ is the velocity vector of the moving charge. It can be seen that the force acting on the charge q is perpendicular to the plane that is spanned by the velocity vector $\boldsymbol{v}$ and the magnetic field $\boldsymbol{B}$.

Fundamentals of Magnetic Moment

The simplest magnetic source is a dipole, which is also the basis for the definition of magnetization $\boldsymbol{M}$. A magnetic dipole consists of two poles: a north pole and a south pole. A schematic of the magnetic dipole and its field is shown in Figure 2.1a. The fact that only magnetic dipoles exist and not monopoles can be directly derived from the second Maxwell equation:

$$\nabla \cdot \boldsymbol{B} = 0\,, \tag{2.3}$$

which states that the divergence of the magnetic field is zero, meaning that the magnetic vector field is source-free.

The resulting magnetic dipole moment of a current loop $\boldsymbol{I}$ that encloses the surface area A

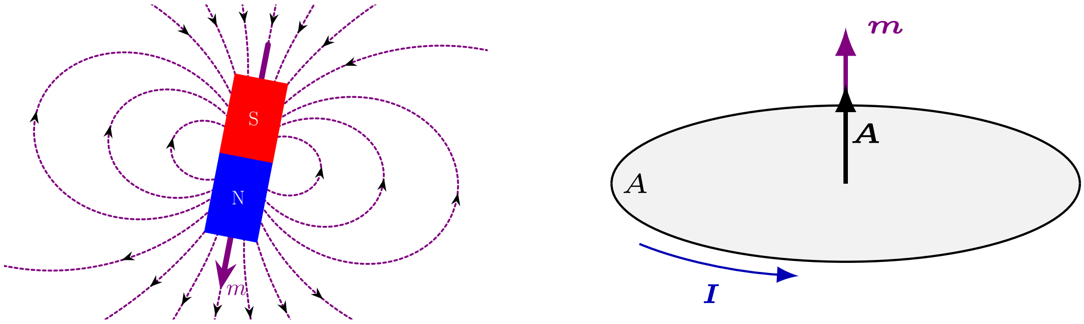

(a)

(b)

Figure 2.1: (a) Magnetic dipole $\boldsymbol{m}$ and its resulting magnetic field. (b) Magnetic moment of a current loop $\boldsymbol{I}$.

is given by the following:

$$\boldsymbol{m} = \boldsymbol{I} \cdot \boldsymbol{A}\,, \tag{2.4}$$

where $\boldsymbol{A}$ is a vector pointing towards the direction orthogonal to the surface A with its length proportional to the surface area, as illustrated in Figure 2.1b. When a magnetic dipole $\boldsymbol{m}$ is placed within a magnetic field, it experiences a resulting magnetic torque $\boldsymbol{\tau}$:

$$\boldsymbol{\tau} = \boldsymbol{m} \times \boldsymbol{B}\,, \tag{2.5}$$

which acts perpendicular to both the magnetic field and the magnetic dipole. The magnetic field due to a magnetic dipole can be calculated as follows:

$$\boldsymbol{B}(\boldsymbol{r}) = \frac{\mu_0}{4\pi}\left(\frac{(3(\hat{\boldsymbol{r}} \cdot \boldsymbol{m})\hat{\boldsymbol{r}} - \boldsymbol{m})}{r^3}\right)\,, \tag{2.6}$$

where $\hat{\boldsymbol{r}}$ is the unit direction vector, $\boldsymbol{r}$ is the position vector of the point to be evaluated, r is the distance between the dipole and the point to be evaluated. It can be seen, that the magnetic field strength decreases with r^3.

Magnetic Material and their Magnetization

When magnetic materials are exposed to an external magnetic field, they generate their own magnetic field in response. This process is known as the magnetization $\boldsymbol{M}$. The magnetization represents the overall effect of the individual magnetic moments $\boldsymbol{m}$ within a material, and can be calculated as the sum of all the dipole moment vectors:

$$\boldsymbol{M} = \sum_i \boldsymbol{m}_i \,. \tag{2.7}$$

This phenomenon is important to understand the magnetization of the Earth's crust. Additionally, a classical type of magnetometer, known as the *Fluxgate*, utilizes this phenomenon to measure the strength of the magnetic field.

Materials are mainly subdivided into three groups based on their response to the magnetic field. These material groups are referred to as: *diamagnetic*, *paramagnetic*, and *ferromagnetic*. These material responses to the magnetic field can also be quantified by the magnitude of proportionality factor called susceptibility χ. Magnetic susceptibility measures how much a material becomes magnetized by an external magnetic field $\boldsymbol{H}$:

$$\boldsymbol{M} = \chi \boldsymbol{H} \tag{2.8}$$

In *diamagnetic materials*, each magnetic moment tend to align opposite to the direction of the applied magnetic field, producing a net magnetization that counteracts the external magnetic field, as the vector $\boldsymbol{M}$ points in the opposite direction of the magnetic field $\boldsymbol{B}$. This effect is typically very weak, which results in a small, negative susceptibility $\chi_{dia.} < 0$. In addition, diamagnetic materials lose their magnetization once the external magnetic field is removed.

When the induced magnetization vector aligns with the external field in which it is located, the material is called *paramagnetic*. In these materials, each magnetic moment generally aligns with the applied external magnetic field. However, this magnetic alignment is only weakly present as the the magnetic moments not fully align with the field direction, leading to a small and positive susceptibility $\chi_{para.} > 0$. As in the case of *diamagnetic* material, the alignment of the magnetic moments does not stay when the externally applied magnetic field is removed, meaning that the magnetization is only present while the external magnetic field is present.

Ferromagnetic materials can have independent magnetization that does not necessarily correspond to the external magnetic field. This means that the magnetic moments within the material align with the external field direction, which stay aligned even if the external field is removed. This property allows ferromagnetic materials to become permanent magnets.
ferromagnetic materials also exhibit saturation effect when an increase in the applied external magnetic field $\boldsymbol{H}$ can no longer increase the material's magnetization. At this point, the

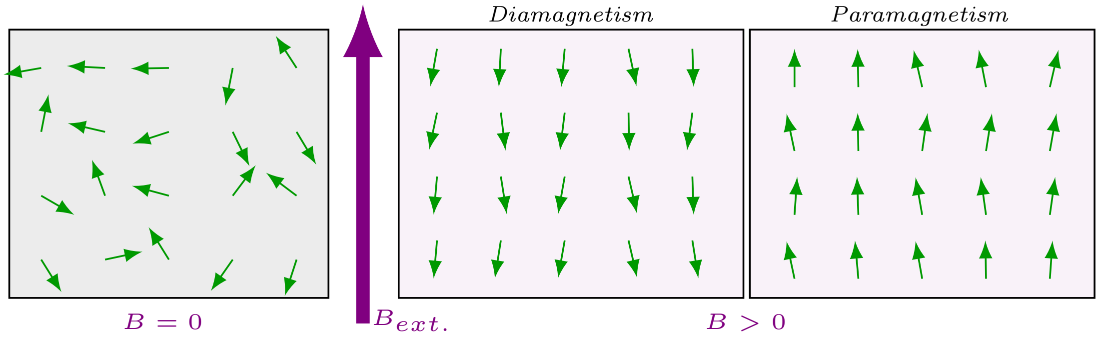

Figure 2.2: Illustration of the magnetic moments within a magnetic material. When no external magnetic field is present, the net magnetization of each magnetic moment (depicted as small green arrows) sums to zero. When an external magnetic field is applied to *diamagnetic* materials, the magnetic moments tend to align in the opposite direction of the applied $\boldsymbol{B}_{ext.}$. In *paramagnetic* materials, the magnetic moments align with the direction of the magnetic field. However, they tend to align only partially, leading to a weak net magnetization $\boldsymbol{M}$.

total magnetic flux density $\boldsymbol{B}$ reaches its maximum value.

The magnetization response of a ferromagnetic material when exposed to an external magnetic field is represented by the hysteresis curve. A schematic representation of the hysteresis curve is shown in Figure $2.3b$. Initially, the unmagnetized material becomes magnetized upon exposure to the field, but the magnetization does not increase linearly. It reaches the saturation point where higher magnetic field strengths no longer result in a higher magnetization. Once the material is magnetized, an external magnetic field opposing the direction of magnetization must be applied to reduce or reverse the magnetization. A magnetic field of magnitude H_{cor}, so called *Coercivity*, and opposing the magnetization vector has to be applied to fully demagnetize the magnetized ferromagnetic material. Another way to demagnetize an magnetized ferromagnet is increasing its temperature. Above a material specific temperature, also known as the *Curie* temperature T_C, the aligned magnetic moments get disordered leading to demagnetized state $\boldsymbol{M}(T > T_C) = 0$. Once magnetized by an external magnetic field the material retains some magnetization, when the magnetic field is removed, which is also known as *Remanence*.

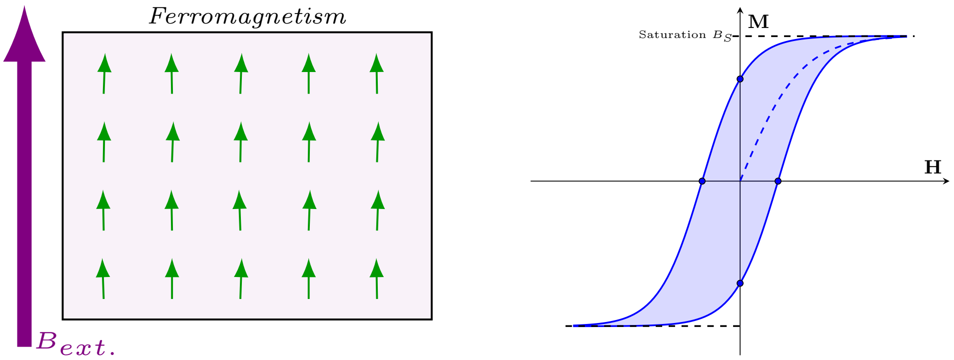

(a)

(b)

Figure 2.3: (a) An external magnetic field aligns the magnetic moments within the ferromagnetic material. (b) Hysteresis curve of a ferromagnetic material is shown. A non-magnetized material becomes magnetized upon exposure to an external magnetic field $\boldsymbol{H}$. However, the relationship between the applied magnetic field and magnetization is not linear, as the maximum magnetization, known as *Saturation*, is reached. When the magnetic field is removed, the material retains some magnetization, which is known as *Remanence*.

Current-Induced Magnetic Fields

As previously mentioned, moving charges or an electric current $\boldsymbol{I}$ generate a magnetic field. The experimentally determined mathematical representation of this field for arbitrary current shapes $\boldsymbol{I}$ is given by the equation below:

$$\boldsymbol{B}(\boldsymbol{r}) = \frac{\mu_0}{4\pi} \int \frac{I\,d\boldsymbol{L}}{|\boldsymbol{r}-\boldsymbol{r}_I|^2} \times \frac{\boldsymbol{r}-\boldsymbol{r}_I}{|\boldsymbol{r}-\boldsymbol{r}_I|}\,. \tag{2.9}$$

This equation is also known as the *Biot-Savart* law. The magnetic field induced by the current $\boldsymbol{I}$ is the integral of the cross-product of the finite element length $d\boldsymbol{L}$ of the current and the distance vector $\boldsymbol{r}-\boldsymbol{r}_I$ between the point $\boldsymbol{r}$ t which the field should be evaluated and the position $\boldsymbol{r}_I$ of the infinite element length. This equation clearly shows, after integrating over the entire current length, the dependence on the distance r, with the magnetic field decreasing proportionally to r^3, as seen in Equation 2.6.

This is an important phenomenon, as every current flow produces a magnetic field, which can cause distortions and unwanted noise, especially in indoor environments. In addition, Alternating Current (AC) generates an alternating magnetic field. Since the current in an

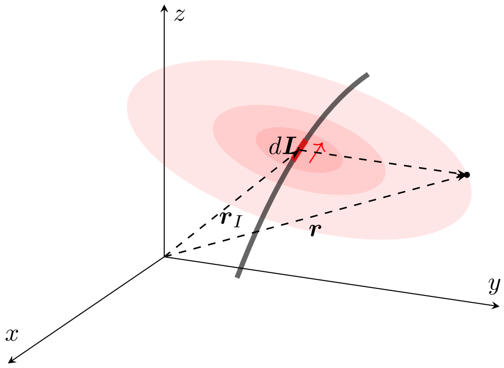

Figure 2.4: Schematic of the quantities for calculating current-induced magnetic field.

AC circuit changes direction periodically, the resulting magnetic field also fluctuates in both magnitude and direction at the same frequency as the current. In indoor environments, AC power lines and electronic devices can contribute to magnetic field noise, which will be a crucial factor to consider in the experimental setup discussed in the later Section.

By approximating this integral for long straight currents, one can calculate some resulting magnetic field strengths from currents within a typical household or laboratory. For these currents the resulting magnetic field strengths are typically within the order of $0.01\ \mu\mathrm{T}$ to $10\ \mu\mathrm{T}$ for distance of some meters away to a few cm. Another example is the magnetic field strength near high-voltage power lines, such as those used for trams, which are located $50-100$ meters away. At street level, just a few meters from a power distribution line, the magnetic field strength ranges from 0.01 to $1\mu\mathrm{T}$.

Induced Currents in Conductive Materials

Eddy currents are currents induced in electrically conductive materials due to time-varying magnetic fields. This is also known as the *Faraday*'s law of induction, which is the third *Maxwell* equation:

$$\nabla \times \boldsymbol{E} = -\frac{\partial \boldsymbol{B}}{\partial t} \tag{2.10}$$

Following the *Biot-Savart* law, these currents also generate a magnetic field, which can distort the magnetic field of interest.

2.1.2 The Behavior of Atoms in an External Magnetic Field

The following sections focus on key phenomena related to atoms and electrons and the behavior of their dipole moments in a magnetic field. This is a classical description of quantum mechanical phenomena that also have an equivalent quantum mechanical description.

Magnetic Moment

At the quantum level, particles such as electrons or atoms with angular momentum exhibit magnetic dipole moments.
Classically, each atom generates a magnetic dipole moment due to the motion of electrons around the positively charged nucleus, similar to a current loop (as shown in Equation 2.4), also known as the orbital magnetic moment. This arises because atoms possess orbital angular momentum $\boldsymbol{J}$.
Additionally, particles like electrons can have a magnetic moment due to their intrinsic spin $\boldsymbol{S}$. Particles with spin generate a magnetic dipole moment, much like a rotating electrically charged body in classical electrodynamics.

$$\boldsymbol{m} = \gamma \boldsymbol{J}\,, \tag{2.11}$$

here the proportionality factor between the two quantities is called the gyromagnetic ratio γ. This induced magnetic moment is also known as the spin magnetic moment.

The total magnetic moment of an atom is the vector sum of the orbital and spin magnetic moments. For an atom with a single electron (such as hydrogen ^1H), the total magnetic dipole moment is proportional to the angular momentum and spin of the electron.

Zeeman Splitting

The *Zeeman* splitting is an important quantum phenomenon that describes the splitting of atomic energy levels when exposed to an external magnetic field. This effect is crucial in quantum magnetometry, as it allows the measurement of the magnetic field by observing the splitting of energy levels. The splitting arises due to the interaction between spin $\boldsymbol{J}$ and the external field $\boldsymbol{B}$ it experiences. The energy shift ΔE between the levels due to the Zeeman effect is given by the following equation:

$$\Delta E = \Delta m_J \hbar \gamma |\boldsymbol{B}|\,, \tag{2.12}$$

where $\hbar$ is the Planck's constant and γ is the gyromagnetic ratio, the term Δm_j is the change of quantum number and the $|\boldsymbol{B}|$ the total intensity value of the magnetic field applied.

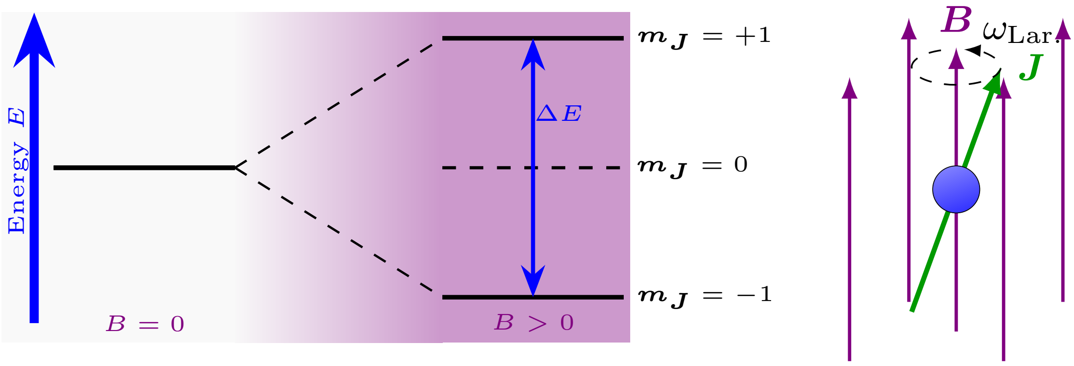

(a)

(b)

Figure 2.5: (a) Splitting of the energy level of due to an external magnetic field. (b) Precession of the spin $\boldsymbol{J}$ due to the torque it experiences.

Larmor Precession

Since the magnetic moment has angular momentum $\boldsymbol{J}$, it experiences a magnetic torque when exposed to a magnetic field $\boldsymbol{B}$, as seen in Equation 2.5. It therefore undergoes a precessional motion around the direction of the applied magnetic field. This precession is analogous to the precession known in classical physics. The precession of a spin system around the applied magnetic field occurs at a characteristic *Larmor* frequency ω_{Larmor}, which is proportional to the energy difference ΔE induced by the magnetic field strength:

$$\omega_{Larmor} = \frac{\Delta E}{\hbar} = \gamma|\boldsymbol{B}| \tag{2.13}$$

Magnetization of Atom Ensembles

In many cases, such as when describing how OPM magnetometers work, an ensemble of magnetic moments must be considered. In the absence of an external magnetic field, the orientation of the magnetic moments will be completely random, leading to the cancellation of each other out. As a result, the sum of the magnetic moments will be zero.

In contrast, when the ensemble of magnetic moments is exposed to an external magnetic field $\boldsymbol{B}$ the spins will align themselves parallel as well as anti-parallel with respect to the field direction. The energy difference between these two energy states of a considered two level system is given by the *Zeeman shift*. Because of the energy difference between the parallel and the anti-parallel aligned magnetic moments, the population of the energy states will not be identical. As the parallel aligned magnetic moments occupy the state with lower energy for $\gamma > 0$, this state will be more favored. Since magnetic moments with opposite alignments cancel each other out, only a weak net magnetization vector $\boldsymbol{M}$ can be detected. Consequently, only the surplus of the magnetic moments in the lower energy state result in the net magnetization vector $\boldsymbol{M}$ oriented in the direction of $\boldsymbol{B}$.

The resulting magnetization M of the two-level system is proportional to the population difference of the two different alignments:

$$M = \mu(N_+ - N_-)\,, \tag{2.14}$$

where μ is the permeability and N_+ is the number of magnetic moments in the upper energy level, that can be expressed with the help of the Boltzmann distribution as:

$$N_+ = \frac{N}{1 + \exp\left\{-\frac{\gamma\hbar B}{k_\mathrm{B}T}\right\}}\,,\; N_- = \frac{N}{1 + \exp\left\{\frac{\gamma\hbar B}{k_\mathrm{B}T}\right\}}\,. \tag{2.15}$$

$N = N_+ + N_-$ is the total number of magnetic moments in the considered ensemble, $\hbar$ is Planck's constant h divided by 2π, k_B the Boltzmann constant and T the temperature of the considered ensemble. With these two Equation of 2.15 for the different energy state populations, the equation for the net magnetization vector 2.14 follows:

$$M(B,T) = N\mu\left[\frac{1 - \exp\left\{-\frac{\gamma\hbar B}{k_\mathrm{B}T}\right\}}{1 + \exp\left\{-\frac{\gamma\hbar B}{k_\mathrm{B}T}\right\}}\right] = N\mu\tanh\left\{\frac{\gamma\hbar B}{2k_\mathrm{B}T}\right\}. \tag{2.16}$$

This equation is also called the Brillouin equation. Since the magnetization vector scales with $\tanh$ a saturation effect for very strong magnetic fields can be observed.

Bloch Equations

It can be seen that the net magnetization vector of the atomic ensemble can be influenced by the applied magnetic field. When exposed to a static magnetic field, the net magnetization is static and aligned parallel to the direction of the magnetic field. As the individual magnetic moments precess around the direction of the magnetic field, the ensemble averages out in the transverse direction, leaving the net magnetization with only a component in the longitudinal direction of the magnetic field. When a time-varying magnetic field is applied, the net magnetization vector begins to undergo a dynamic motion. The complete motion of the magnetization vector as a function of the applied magnetic field can be described by the following differential equation, known as the *Bloch* equations:

$$\frac{\mathrm{d}}{\mathrm{d}t}\begin{pmatrix} M_x(t) \\ M_y(t) \\ M_z(t) \end{pmatrix} = \begin{pmatrix} M_x(t) \\ M_y(t) \\ M_z(t) \end{pmatrix} \times \begin{pmatrix} \gamma B_x \\ \gamma B_y \\ \gamma B_z \end{pmatrix} . \tag{2.17}$$

The equations presented here are also known as relaxation-free *Bloch* equations, since they do not include any relaxation terms of the magnetization vector.

Optically Pumping

For magnetometry purposes and to obtain a measurable signal, the use of an ensemble of atoms is essential. To achieve this, it is crucial to create a net magnetization, also known as macroscopic spin polarization. This involves aligning a large fraction of the atomic spins in the same direction, similar to the magnetization of a medium. In classical NMR applications, this alignment is typically achieved using strong magnetic fields. In alkali atoms, however, spin polarization can be achieved more efficiently by optical pumping, where the interaction between light and the atom is used to increase the spin polarizatoin.

Without further derivation, and as stated in [9], the angular momentum selection rules of the light-atom interaction are the following:

$$\begin{aligned} \Delta L &= \pm 1 \, , \Delta S = 0 \, , \\ \Delta J &= \pm 1 \, , \Delta F = \pm 1 \, . \end{aligned}$$

It can be seen that by absorbing a photon, angular momentum can be transferred without changing the spin. The selection rules for the magnetic quantum number depend on the circular polarization of the pumping light. It is important to note that the pumping occurs and the magnetization builds up in the direction of light propagation. In addition, the spontaneous decay of the pumped states leads to a change in the magnetic quantum number, with $\Delta m_J = \pm 1$.

By modeling the absorption of circularly polarized photons, which transfer their angular momentum to the atom, and also taking into account the spontaneous decay of the excited states, the following differential equation for the magnetization vector can be derived:

$$\frac{\mathrm{d}}{\mathrm{d}t}\begin{pmatrix} M_x(t) \\ M_y(t) \\ M_z(t) \end{pmatrix} = \Gamma_{\text{pump}} \begin{pmatrix} 0 - M_x(t) \\ 0 - M_y(t) \\ M_{\text{pump}} - M_z(t) \end{pmatrix} - \Gamma_{\text{decay}} \begin{pmatrix} M_x(t) \\ M_y(t) \\ M_z(t) \end{pmatrix} \tag{2.18}$$

$$= \Gamma_{\text{pump}} \begin{pmatrix} -M_x(t) \\ -M_y(t) \\ M_{\text{eff.}} - M_z(t) \end{pmatrix} \tag{2.19}$$

where Γ_{pump} is the rate of optical pumping and Γ_{decay} is the rate of decay due to spontaneous emission. By introducing an effective pumping rate Γ and an effective magnetization $M_{\text{eff}} = M_{\text{pump}}\frac{\Gamma_{\text{pump}}}{\Gamma}$, Equation 2.18 can be further reduced to Equation 2.19. By incorporating the additional term that accounts for net magnetization due to optical pumping into the general relaxation-free Bloch equations introduced in Equation 2.20, the following differential equations are obtained:

$$\frac{\mathrm{d}}{\mathrm{d}t}\begin{pmatrix} M_x(t) \\ M_y(t) \\ M_z(t) \end{pmatrix} = \begin{pmatrix} M_x(t) \\ M_y(t) \\ M_z(t) \end{pmatrix} \times \begin{pmatrix} \gamma B_x \\ \gamma B_y \\ \gamma B_z \end{pmatrix} + \Gamma \begin{pmatrix} -M_x(t) \\ -M_y(t) \\ M_{\text{eff.}} - M_z(t) \end{pmatrix}. \tag{2.20}$$

This equation is important because it describes how optical pumping influences the net magnetization vector of the magnetic ensemble.

2.2 Magnetic Field Sensing Principles

This section introduces the principles of magnetic field sensing, both through classical methods and quantum mechanics. It explains the working principles of the magnetometers used in the experimental setup of this thesis and provides a brief overview of different types of magnetometers selected. These sensors are divided into two types: Classical Magnetometer (CM), which are widely available, and Quantum-based Magnetometer (QM), which are emerging technologies that utilize quantum mechanical properties to measure magnetic fields.

This section aims to provide a brief overview of the operating principles of each magnetometer type selected, illustrating the key differences between them, and highlight how quantum-based magnetometers leverage quantum phenomena to provide absolute measurements.

2.2.1 Classical Magnetometry

There are several techniques for measuring magnetic field strength based on classical magnetic phenomena. The following section briefly presents the three most common techniques: the *Hall* sensor, the *Fluxgate* sensor, and the *Magnetoresistive* sensor.

Hall Sensors

A widely used type of magnetometer is the *Hall* sensor. These magnetometers exploit the *Hall* effect.

A conductor carrying an electric current I induces a voltage, called the *Hall* voltage U_{Hall}, along its length when a perpendicular magnetic field is applied. The *Hall* voltage is proportional to both the magnetic field strength $\boldsymbol{B}$ and the current $\boldsymbol{I}$. An schematic of a *Hall* sensor is shown in Figure 2.6. The relationship is given by the equation below:

$$U_{\mathrm{Hall}} = \frac{I\,B}{e\,n\,t}\,, \tag{2.21}$$

where e is the charge of an electron, n is the density of electrons and t is the thickness of the conductor. The voltage induced by the *Lorentz* force results from the deflection of charges in the current, leading to a charge imbalance in the conductor. *Hall* sensors are widely used in various fields, However their sensitivity is limited compared to other sensor types to about $1\mathrm{nT}/\sqrt{\mathrm{Hz}}$ [9].

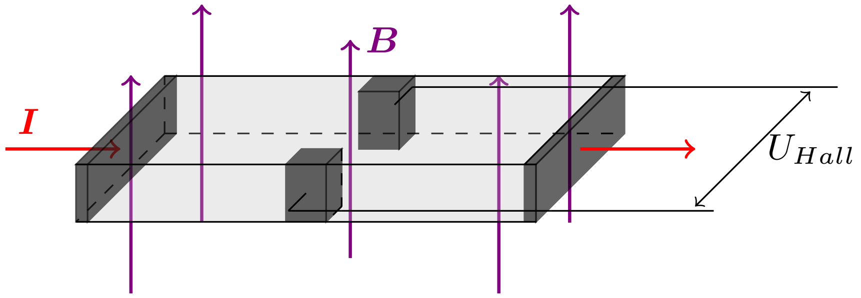

Figure 2.6: Schematic of a *Hall* sensor. A voltage U_{Hall} is induced across its length when a conductor carrying current $\boldsymbol{I}$ is subjected to a magnetic field $\boldsymbol{B}$ perpendicular to the current.

Fluxgates

Fluxgate magnetometers, contrary to Hall magnetometers, use a ferromagnetic core and its hysteresis curve to detect the surrounding magnetic field. The sensor often consists of a ring shaped ferromagnetic core wrapped with magnetization windings also known as a Drive Coil. Additional sensing windings are present to capture the induced currents generated by changes in the net magnetic field due to the magnetization of the core. A schematic of a *Fluxgate* magnetometer and its construction is depicted in Figure 2.7a. The measurement process involves detecting the core's saturation when exposed to a combination of the external magnetic field $\boldsymbol{B}_{\text{ext.}}$ and an alternating field $\boldsymbol{B}_{\text{AC}}$ produced by alternating currents in the Drive Coil [14]. The net magnetic field $\boldsymbol{H}_{\text{net}}(t)$ at any point in time is the sum of the external magnetic field $\boldsymbol{H}_{\text{ext.}}$ and the alternating magnetic field $\boldsymbol{H}_{\text{AC}}(t)$, as expressed mathematically in the following equation [15]:

$$\boldsymbol{H}_{\text{net}}(t) = \boldsymbol{H}_{\text{ext.}} + \boldsymbol{H}_{\text{AC}}(t) \tag{2.22}$$

The key principle behind this technique is that, in the absence of an external magnetic field, the induction of the magnetic field due to the AC current would be symmetrical. However, when an external magnetic field is present, it magnetizes the ferromagnetic core. This magnetization leads to an asymmetrical response, due to the hysteresis curve (see Figure 2.3b), to the applied field, allowing to measure the external magnetic field. The resulting net magnetic field $\boldsymbol{B}_{\text{net}}(t)$ is a function of the external magnetic field $\boldsymbol{H}_{\text{ext.}}$, as shown in the following equation:

$$\boldsymbol{B}_{\text{net}}(t) = f\left(\boldsymbol{H}_{\text{ext.}}(t)\right) \tag{2.23}$$

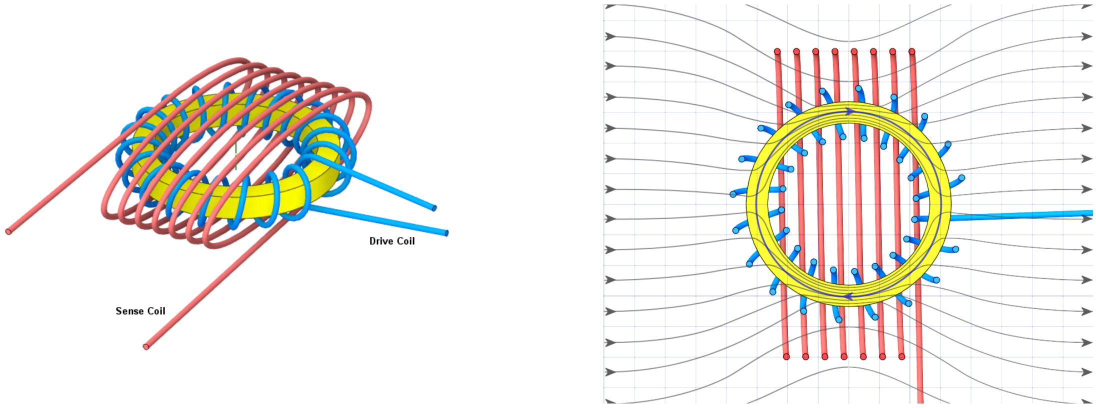

(a)

(b)

Figure 2.7: (a) Schematic of a *Fluxgate* magnetometer, consisting of a ring-shaped ferromagnetic core. Wrapped around the core is a magnetization coil, also known as the Drive Coil. Surrounding the ring and the Drive Coils is a Sense Coil that detects the induced current. (b) Cross section of the ferromagnetic core. The drive coil induces a magnetization within the core that is parallel in the upper half of the ring and opposite to the external field direction in the lower half.[13]

This signal is proportional to the external magnetic field. The induced electromotive force $\boldsymbol{E}_{\textit{ind.}}(t)$ is related to the time derivative of the magnetic field, as described by the equation below:

$$\boldsymbol{E}_{\textit{ind.}}(t) = -sw\frac{\partial \boldsymbol{B}(t)}{\partial t} \,, \tag{2.24}$$

where s is the area of the ferromagnetic core enclosed by the drive coil and w is the number of turns of the drive coil.

Since the ring-shaped core has two halves with opposing magnetization vectors, the induced $\boldsymbol{E}_{\textit{ind.}}$ in the sense coil would be zero in the absence of an external magnetic field. However, in the presence of an external field, one half, where the magnetization vector aligns with the field, reaches saturation before the other half, which has the opposing magnetization direction, as illustrated in 2.7b. As a result, the induced $\boldsymbol{E}_{\textit{ind.}}$ from each half does not fully cancel out, leading to a current spike in the sense coil when this occurs. The Drive Coil is continuously driven with AC, and as the halves periodically switch between saturated and unsaturated states, periodic signal peaks are detected in the Sense Coil. By measuring the periodic current signal from the sense coil and using Equation 2.22 and further approximating the relation of Equation 2.23, the induced signal depends on the desired $\boldsymbol{H}_{ext.}$ and can be calculated when $\boldsymbol{H}_{AC}(t)$ is known [15].

Fluxgate magnetometers are often the preferred solution to monitor Earth's magnetic field on ground but also in space, as they offer high sensitivity down to $0.1n\mathrm{T}$ within a field range of up to $100\mu\mathrm{T}$. The sensitivity of these magnetometer is usually around $6\text{-}10\mathrm{nT}/\sqrt{\mathrm{Hz}}$. The main challenges are the drifts and the calibration step required to maintain the accuracy of the magnetometer readings. ts are primarily linked to the temperature sensitivity and aging of the coils [16].

Magnetoresistive Magnetometer

The classical magnetometer used in the following laboratory experiment operates based on a phenomenon called anisotropic magnetoresistance.

The resistance of a ferromagnetic material depends hereby on the angle θ between the magnetization direction of the material $\boldsymbol{M}$ and the applied current $\boldsymbol{I}$ [17]. The term anisotropic originates from the fact that in most ferromagnetic materials the resistivity varies with angle θ. Thus, for parallel alignment $\boldsymbol{B}||\boldsymbol{I}$ the measured resistivity $\rho_{||}$ is higher than when both are perpendicular to each other $\boldsymbol{B}\perp\mathbf{I}$.

It is possible to measure the changes in the magnetic field by measuring this resistance change. In the case of the chips incorporated in the CM, nickel-iron (Permalloy) thin-film segments are deposited onto a silicon wafer, which makes it possible to construct a so-called *Wheatstone bridge*. This structure is a typical setup used to measure resistance changes. In this setup, resistors are arranged in a diamond-like configuration. Input voltage is applied across one axis of the structure, and a voltage reading is taken across the other axis of the diamond structure. In the case of the magnetometer setup, this is very similar. An illustration of this sensor bridge design can be found in Figure 2.8. The input voltage is applied across the horizontal axis of the structure. Within the structure, Permalloy sections are incorporated with different orientations of the permalloy material in the four arms of the diamond structure. The voltage which measure the resistance change across the different arms of the structure are taken across the vertical axis between **Out**$+$ and **Out**$-$. When an external magnetic field is present, the resistivity of the magnetoresistive material changes. This change can be detected as a voltage change when a constant voltage is applied to the bridge. This occurs because the output voltage is sensitive to the resistance changes in the bridge caused by the magnetic field. These resistive elements are aligned along a common sensitive axis, ensuring that an increase in the magnetic field along this axis produces a positive voltage change.

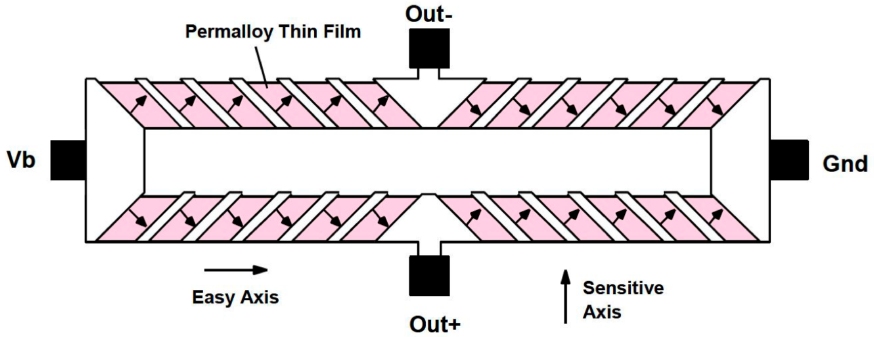

Figure 2.8: Schematic representation of a magnetoresistive bridge sensor utilizing permalloy thin film structures. The diagonal arrows indicate the magnetization direction along the easy axis. The bridge configuration allows a voltage measurement between **Out**$+$ and **Out**$-$ when an input voltage **Vb** is applied, providing a signal proportional to the external field along the sensitive axis.[18]

Since a single bridge structure provides information about only one component of the magnetic field, three such bridges can be arranged perpendicularly to one another to enable the measurement of all three components of the magnetic field. This configuration allows for the detection of arbitrary field directions.

2.2.2 Quantum-based Magnetometry

Many new concepts for magnetometry using quantum-mechanical phenomena have been and are being developed. Quantum-based magnetometers, operating in the quantum regime, are in principle to be absolute, meaning they provide accurate measurements. These devices are expected to offer drift- and bias-free measurements without the need for calibration. Today, the most commonly known magnetometers include OPM, NV centers, the so-called Superconducting Quantum Interference Device (SQUID), and Spin Exchange Relaxation-Free (SERF) magnetometers. Furthermore, a relatively new concept using Rydberg atoms, not only for electrometry but also for magnetometry, has been demonstrated [19]. This is also the aim of the department of Quantum NanoPhysics where this Master thesis takes place, to develop and implement a Rydberg-based sensor that can measure both electric and magnetic fields.

The following section briefly presents the working principles of three selected sensors: OPM, NV magnetometers, and the SQUID magnetometers.

Optically Pumped Magnetometers

The quantum magnetometer used in the laboratory experiment presented in the following chapters operates on the principle of optically pumped states of vapor atoms within a glass cell.
As described in Section 2.1.2, optical pumping refers to the process of optically exciting atoms from their ground state to an excited state, which internally increases the net magnetization of the atomic ensemble within the vapor cell. This resulting magnetization, which is sensitive to the magnetic field, interacts with the field to be measured. Through this interaction, the magnetic field can be measured on the basis of various schemes for magnetic field detection.
The magnetometer at hand in this work exploits the well-defined precession frequency of rubidium atoms, which depends on the total magnetic field strength they experience. This measurement scheme is known as Free Induction Decay (FID) [20], [21]. A basic schematic of this type of sensor is shown in the following Figure 2.9a. First, a laser beam is circularly polarized by passing through a quarter-wave plate. The scheme for detecting the magnetic field strength is divided into two phases.

In the first phase, a strong polarizing magnetic field $\boldsymbol{B}_{pol}$ is applied, aligned parallel to the light propagation. This field is generated by Helmholtz coils. The incident laser beam, together with the polarizing magnetic field, causes the atoms within the vapor cell to become spin-polarized, increasing the net magnetization of the atomic ensemble within the cell.

In the second phase, the polarizing magnetic field is rapidly switched off, causing the atoms and respectively the net magnetization $\boldsymbol{M_0}$ vector to precess around the magnetic field $\boldsymbol{B}_{ext.}$ to be measured, as it aligns itself with the magnetic field direction. The precession of the magnetization follows the Bloch Equations as shown in Equation 2.20. Following the Equation 2.13, the precession frequency is directly proportional to the magnetic field strength experienced by the atoms. The power of the laser light is tuned down during this period so that it is weak enough to prevent any optical pumping. The light passes through the precessing atoms in the vapor cell, which modulates the light due to the fact that the absorption coefficient of the atomic ensemble depends on the degree and orientation of the net magnetization vector [22]. The light that has passed through the vapor cell is thus proportional to the transverse component of the magnetization vector relative to the direction of light propagation. The transverse component of the magnetization is described as follows:

$$\boldsymbol{M}_{\perp}(t) = \boldsymbol{M}_0 \sin\left(\omega_{Lar.} t + \phi_0\right) e^{-\gamma_{decay} t} \tag{2.25}$$

The decay of the sinusoid is due to the fact that the transverse component of the magneti-

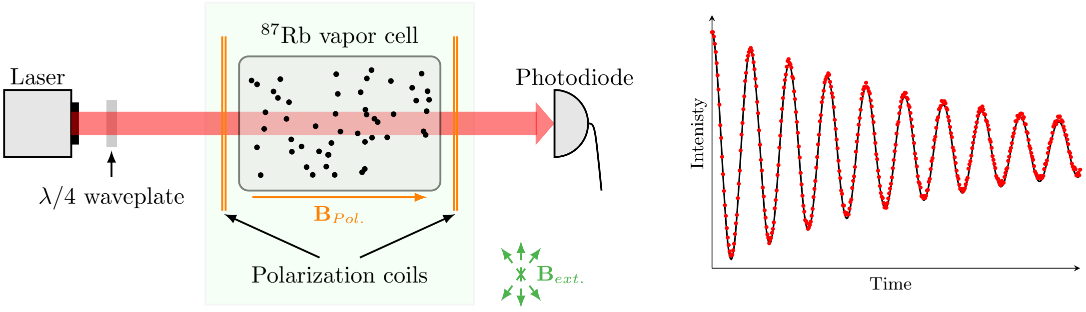

(a)

(b)

Figure 2.9: (a) Schematic diagram of the FID measurement setup used in the OPM QuSpin. The laser light is circularly polarized through a $\lambda/4$ plate and propagates through the vapor cell containing ^{87}Rb atoms. In the first step, a strong polarizing field, $\boldsymbol{B}_{pol}$, is applied to align the spin states. After polarization, $\boldsymbol{B}_{pol.}$ is switched off, and the spins begin to precess around $\boldsymbol{B}_{ext.}$, modulating the light with the corresponding $\omega_{Lar.}$. (b) Output of the photodiode, in the second phase where the $B_{ext.}$ is measured.

zation vector becomes smaller as it aligns with the field direction. Once the magnetization vector is completely aligned, the transverse component has completely disappeared and only the longitudinal component remains. The signal detected by the photodiode is then amplified, and a frequency counter measures the precession frequency. A schematic of the signal detected by the photodiode is shown in Figure 2.9b.

Since the precession frequency has a fixed relationship with the magnetic field strength given by $6.998\mathrm{Hz}/\mathrm{nT}$, the measured frequency can be used to determine the experienced magnetic field.

Nitrogen Vacancy Magnetometers

Nitrogen Vacancy (NV) centers are an emerging quantum sensor technology that is gradually being minituarized and commercialized. These sensors use the spin system induced by a point defect in the diamond lattice, where a nitrogen atom replaces a carbon atom and is directly neighboring to a missing lattice atom, known as a vacancy forming a spin-triplet system. The defect within the lattice is visualized in Figure 2.10a. Hereby, the blue atoms represent the carbon atoms, the red atom represents the Nitrogen atom, and the white ball represents the missing atom.

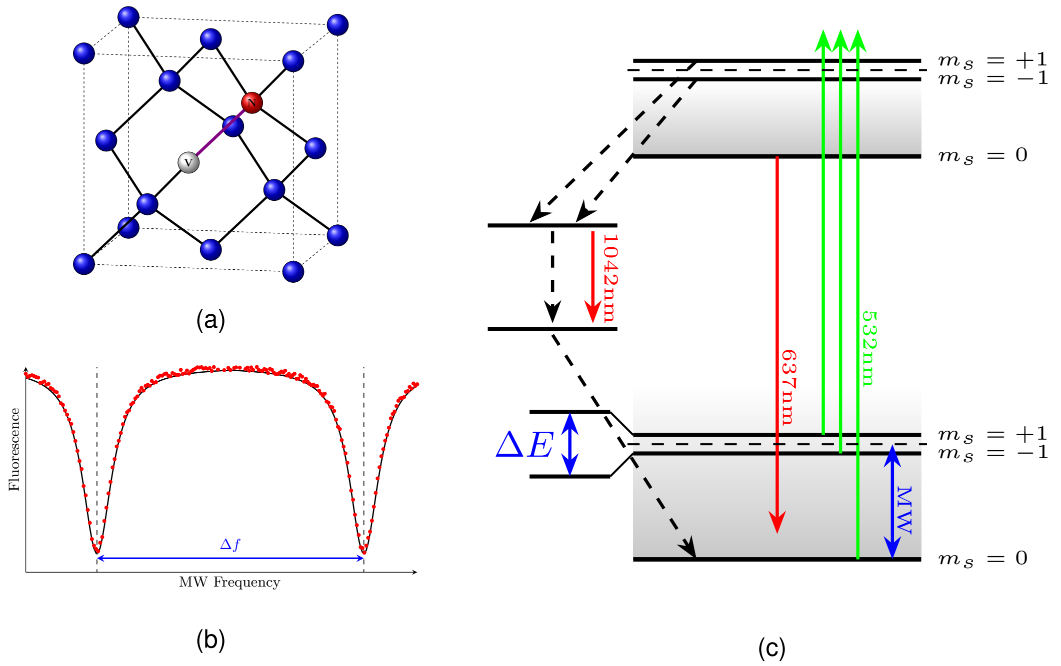

(a)

(b)

(c)

Figure 2.10: (a) Diamond lattice structure containing an NV defect. (b) Fluorescence spectrum detected at the detector. (c) Energy levels and the two pathways of the de-excitation are illustrated.

The NV center's quantum state can be manipulated and read out using microwaves and laser excitation. Its energy levels are sensitive to the surrounding magnetic field, leading to Zeeman splitting, which shifts the resonance frequency.

Under laser excitation, the spin state can be elevated from the ground state to the excited state. De-excitation back to the ground state can occur mainly via two different pathways. The first is a direct transition to the ground state, which is accompanied by the emission of red fluorescent light of $\lambda = 637\mathrm{nm}$, often referred to as the bright state. The second pathway involves an intermediate metastable state, where fluorescence in the infrared spectrum is emitted, and commonly known as the dark state.

A widely used detection method for this system is Optically Detected Magnetic Resonance (ODMR), in which the fluorescence from an NV center in diamond is used to measure an external magnetic field the NV is in. This method relies on the fact that, at microwave resonance which depends on the magnetic field, the $m_s = 0$ spin state is driven into a transition to the $m_s = \pm 1$ states. These states have a higher probability of decaying via the dark-state pathway, where no visible fluorescent light is emitted. By recording the fluorescence intensity while sweeping the microwave frequency over a range that includes the resonance frequency, one can observe two characteristic dips in the ODMR spectrum. This spectrum with the characteristic dips can be seen in Figure 2.10b. The frequency separation Δf between these dips is directly proportional to the Zeeman splitting of the $m_s = \pm 1$ energy levels. With this frequency difference and Equation 2.12, the external magnetic field strength can be calculated.

In contrast to the OPM, the fluorescence depends on the angle θ between the NV axis and the direction of the magnetic field it experiences. This characteristic enables the possibility of vectorizing the magnetic field sensor by incorporating multiple NV centers whose axes are orthogonal to each other, spanning all three spatial dimensions [23].

SQUID Magnetometers

Superconducting Quantum Interference Device (SQUID) magnetometers rely on superconducting materials that incorporate *Josephson* junctions. Unlike other quantum magnetometers, SQUIDs require cooling to low temperatures to achieve the superconducting state. Additionally, the sensor measures the magnetic flux $\mathbf{\Phi}$ through an effective area A to determine the magnetic field strength $\boldsymbol{B}$.

The core component of a SQUID is the *Josephson* junction, at which tunneling of electron pairs across the junction happen. The tunneling current at the junctions are used to calculate the magnetic flux the magnetometer is experiencing. According to [24], the tunneling current between the two superconductors is described by the first *Josephson* equation (Equation 2.26), which depends on the applied current I_0 and the phase difference between the superconductors, $\phi_2 - \phi_1$. The second *Josephson* equation, stated in Equation 2.27, describes the time evolution of the phase difference due to the applied voltage V across the two superconductors.

$$I_s = I_0 \sin\left(\phi_2 - \phi_1\right), \tag{2.26}$$

$$\frac{d}{dt}\left(\phi_2 - \phi_1\right) = \frac{qV}{\hbar}. \tag{2.27}$$

There are two primary types of these magnetometers, classified by the number of *Josephson* junctions incorporated and how the bias current needed to operate the sensor is applied. The *AC SQUID* incorporates only one junction between the superconductors and requires an AC operating current. The *DC SQUID*, on the other hand, incorporates two junctions in parallel and uses direct current for operation.

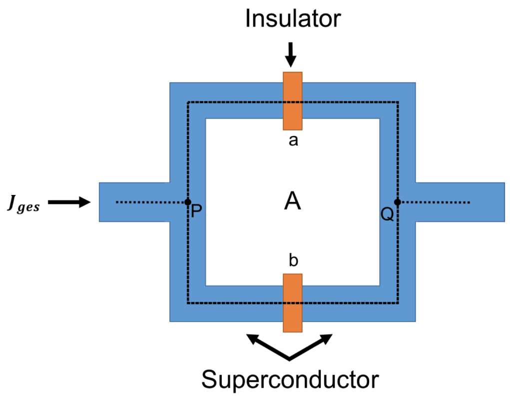

Figure 2.11: Illustration of a *DC SQUID*, which incorporates two *Josephson* junctions. The sensor measures the magnetic flux Φ passing through surface A by measuring the current $I_{ges.}$ due to tunneling at the junctions.[24]

In the following, the structure and operation of a *DC SQUID* will be briefly explained. This type usually consists of a ring-shaped structure made of a superconductor. Two junctions split the ring into two equal halves. The junctions are made of a normal resistive material like copper. In Figure 2.11 a schematic of the structure is illustrated. The superconducting ring encloses the effective surface A, which is essential for the derivation of the magnetic field intensity. Starting with the probability current in an electromagnetic field and using the fact that the induced current of the magnetic field within the structure will result in a current of zero within the structure's volume, one can arrive at the following sum of current at each junction:

$$I_{\text{ges}} = 2I_0 \sin(\delta_0) \cos\left(\frac{q_e}{\hbar}\Phi\right). \tag{2.28}$$

Here, I_0 is the applied current, δ_0 is a constant phase shift between the two superconductor and q_e is the charge of an electron. This equation can be separated into a constant term $2I_0 \sin(\delta_0)$ and a magnetic flux dependent term $\cos\left(\frac{q_e}{\hbar}\Phi\right)$. The constant can be determined by calibrating the current in a known magnetic field with a known magnetic flux. After calibration, the magnetic flux can be determined by measuring the current along both junctions. To find the magnetic field strength B, the surface area A of the ring structure has to be known.

2.3 Earth's Magnetic Field

This section provides a brief introduction to the composition of Earth's magnetic field. Following this, a reference magnetic field model, known as the International Geomagnetic Reference Field (IGRF), is presented. The IGRF is used to calculate the magnetic anomaly field, which is the desired magnetic field component for navigation near the Earth's surface.

2.3.1 Composition

The Earth is surrounded by magnetic fields. The magnetic field experienced at any given location and time is a superposition of multiple sources. Following the description by Canicani (2016) [8], on which this section is based, these sources can be categorized as *internal* and *external*. Internal sources include the magnetic field generated by the Earth's core and the magnetization of the Earth's crust. External sources arise from the ionosphere and the magnetosphere.

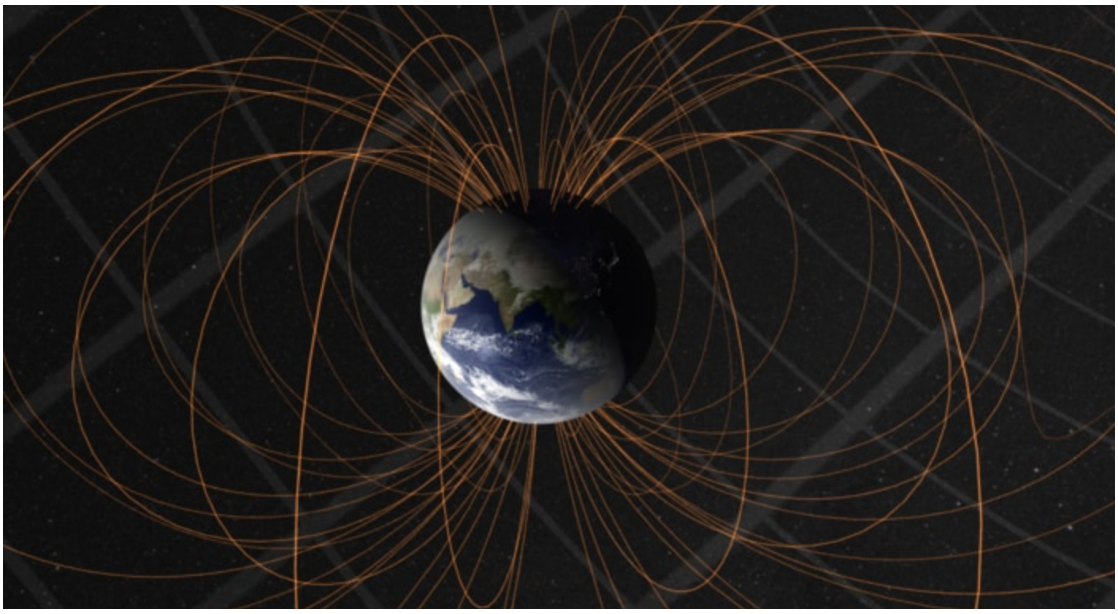

Figure 2.12: Simulation of Earth's dipole-like magnetic field arising from the inner core [25].

The primary magnetic field arising from an internal source is generated by the Earth's fluid outer core, a process known as the geodynamo. This field is responsible for making a compass needle point north. It can be thought of as a dipole field, and it is considered the most dominant field. An illustration of this main magnetic field of the Earth is depicted in Figure 2.12. The field is generated by the motion of an electrically conductive fluid in the core, driven by heat and the rotation of the earth. The magnitude of the magnetic field caused by this varies between $30 - 70\ \mu\mathrm{T}$. Although changes in the movement of the core fluid cause changes in the generated magnetic field, known as secular variation, this deviation is modeled and corrected every 5 years by the IGRF [26].

The second source of the magnetic field is the Earth's crust. The origin of these magnetic fields lies in magnetization, which can result from permanently magnetized materials or induced magnetization due to paramagnetic minerals within it. These spatially varying materials and their non-uniform distribution contribute to the magnetic anomaly field of earth [27]. Anomalies can also be due to man made structures containing magnetic materials which further add to distortions of an ideal dipole field.

Beyond these internal sources, external magnetic fields can arise from processes such as particle interactions in the magnetosphere. These interactions are driven by solar winds, that are streams of charged particles ejected from the Sun's surface. The charged particles interact with Earth's magnetic field, causing them to move in circular currents known as ring currents. These ring currents, in turn, induce additional magnetic fields, particularly in the polar regions. Geomagnetic storms, which occur when intense bursts of solar wind impact the Earth's magnetosphere, cause time-varying fluctuations in Earth's magnetic field, which make denoising techniques to minimize their effects necessary, as these distortions can be in the polar region of the Earth as high as a couple of $10\ \mathrm{nT}$ and at the equator a few nT. One way to mitigate these fluctuations is by observing magnetic fields at geomagnetic observatories. Using these measurements, it may be possible to account for these variations. However, due to the high fluctuations in the polar regions, geomagnetic navigation is not viable there [28].

2.3.2 Reference Magnetic Field Model

The magnetic field induced by the fluid Earth's core changes over time. This overall dipole-like field of the core is modeled by tracking the Earth's magnetic field. The goal is to provide a standardized core field model used worldwide. For magnetic navigation in particular a standardized reference model enables consistent magnetic anomaly field mapping around the entire Earth. This model is based on a spherical harmonic scheme, which attempts to fit periodic harmonics onto the Earth's surface. These harmonics, also known as wave numbers n, are inversely proportional to the spatial wavelength of the Earth. By summing

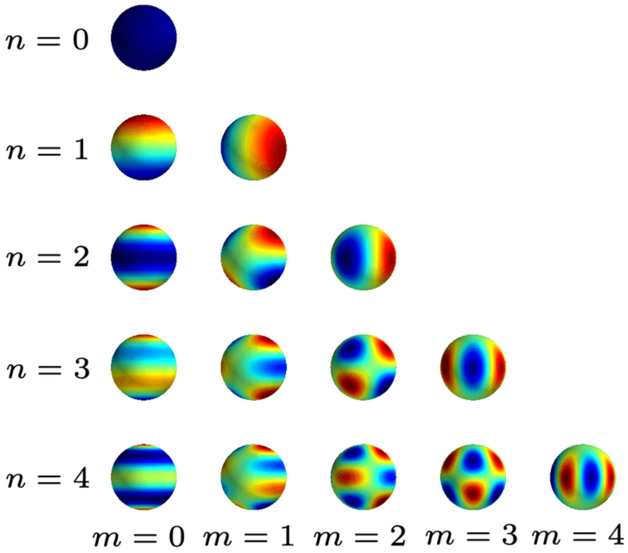

Figure 2.13: Real parts of the spherical harmonics up to and including wavenumber $n = 4$. The IGRF fits coefficients to Schmidt semi-normalized associated Legendre polynomials, each corresponding to a specific wavenumber, to model Earth's dipole-like magnetic field [29].

these spherical harmonics with their respective weights, any arbitrary function on the surface of the Earth can be defined. There are two main parameters that affect the spherical harmonic. One being the wave number n, which determines how often the wave oscillates around the circumference of the sphere, and the secondly m, which determines how often the harmonic oscillates in the longitudinal direction of the sphere for a given n. An illustration of the spherical harmonics for wave numbers up to $n = 4$ is shown in Figure 2.13.
The main contribution of the model comes from low wave numbers, as the Earth's core field can be approximated as a tilted dipole field. On top of this, deviations are captured by higher wave numbers to refine the model further. However, wave numbers until $n < 16$ are considered to arise from Earth's core magnetic field. Higher wave numbers are said to be from the earths crust and its anomalies, which is not to be modeled.

The optimized geomagnetic model that is recalculated every 5 years provides a scalar magnetic potential field $V(r, \phi, \theta, t)$, which depends on the spherical polar coordinates with parameters: radius r, latitude ϕ, longitude θ, and time t. To obtain the desired magnetic field strength $\mathbf{B}(r, \phi, \theta, t)$ at a specific location, the gradient of this potential has to be computed

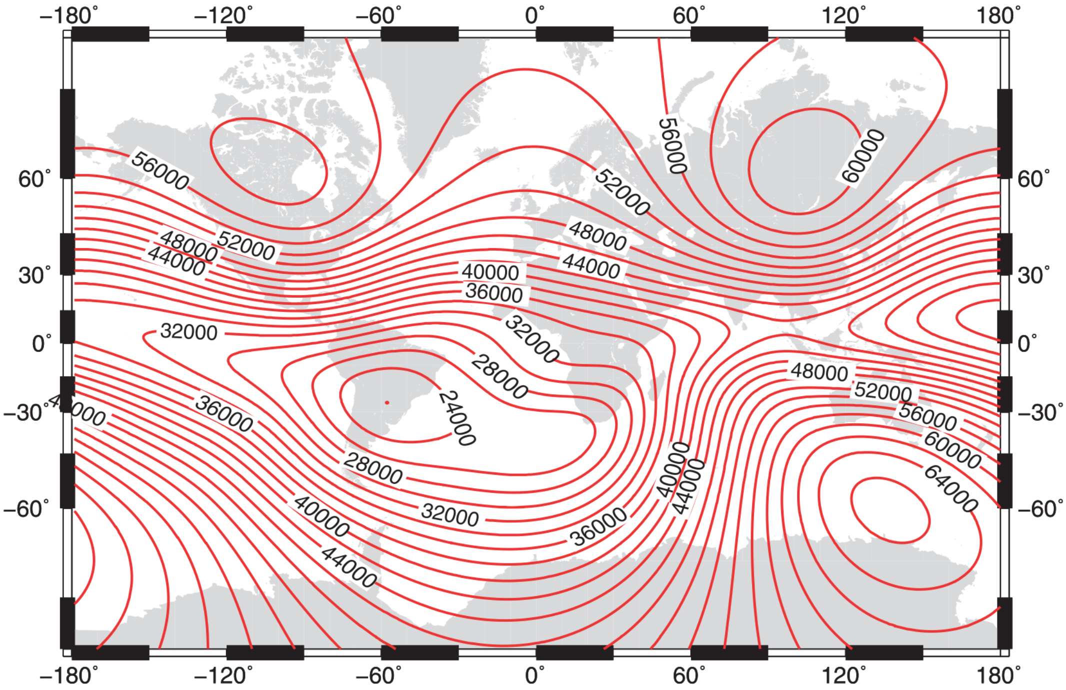

Figure 2.14: Isocontour lines of the Earth's magnetic field calculated from the IGRF model, derived from geomagnetic observations over the past century [26].

at the desired location (r, ϕ, θ):

$$\mathbf{B}(r, \phi, \theta, t) = -\nabla V(r, \phi, \theta, t). \tag{2.29}$$

The scalar magnetic potential field follows from the fitted Gauss coefficients g_n^m and h_n^m for the respective Schmidt semi-normalized associated Legendre polynomial $P_n^m(\phi)$ and is calculated as follows [26]:

$$V(r, \phi, \theta) = a \sum_{n=1}^{n_{max}} \left(\frac{a}{r}\right)^{i+1} \sum_{m=0}^{n} \left[g_n^m \cos(m\theta) + h_n^m \sin(m\theta)\right] P_n^m(\phi). \tag{2.30}$$

The most recent total magnetic field intensities derived form the IGRF model as an contour map is depicted in Figure 2.14.

2.3.3 Magnetic Anomaly Field

The magnetic anomaly field is the preferred field for magnetic navigation on Earth, as it is assumed to remain stable over long periods of time. This stability arises from the magnetization of minerals within the Earth's crust when the surface solidified, making it a reliable reference for navigation. To derive useful information about the anomaly field from total magnetic field measurements obtained through surveys and mapping, one must subtract the standard reference field modeled by IGRF. However, the subtraction of the scalar field measurements alone does not yield the true magnetic anomaly field of the Earth, as the direction of the magnetic anomaly cannot be precisely captured from a single total field intensity measurement. Nevertheless, this information is still useful, as the resulting field represents the projection of the anomaly field component along the magnetic field vector of the reference field. Figure 2.15 shows the magnetic anomaly field map provided by the *NOAA National Centers for Environmental Information* [30].
The mean core field is approximately $50\ \mu\mathrm{T}$. In comparison, the Earth's anomaly field is on the order of hundreds of nT, resulting in a difference of about three orders of magnitude.

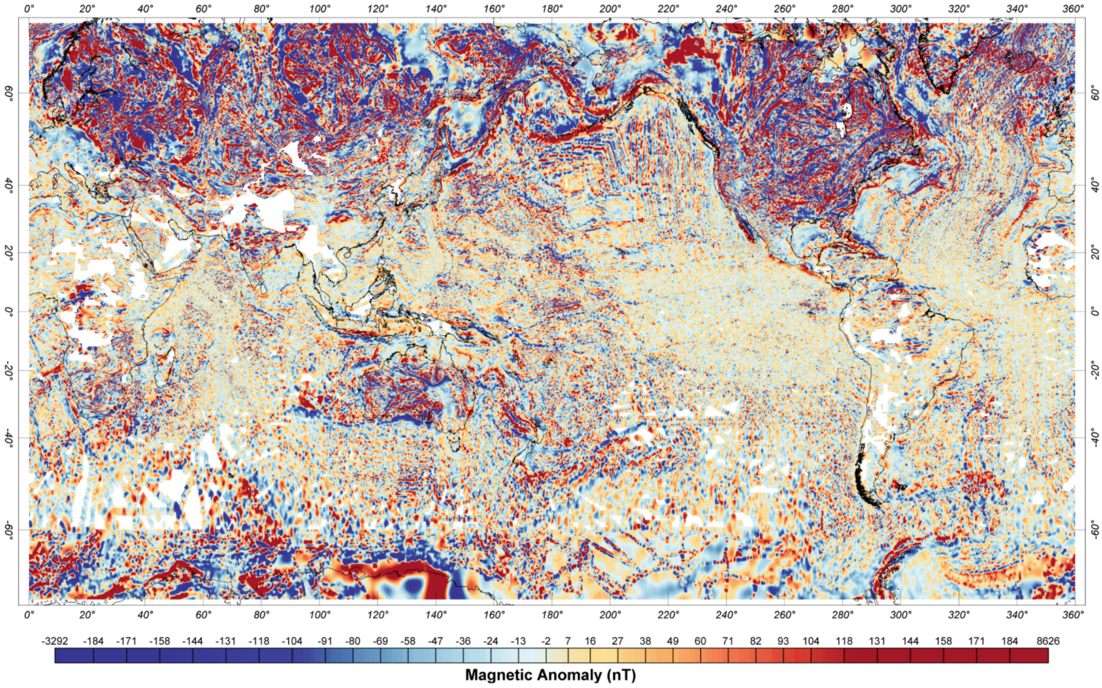

Figure 2.15: Upward-continued Magnetic Anomaly Map of the Earth at an altitude of 4 km above sea level [30].

2.4 Classical Inertial Measurement Sensors

Magnetic field-aided navigation aims to enhance and correct position estimates derived from classical inertial sensor measurements to provide a self-sufficient navigation solution. This section provides a brief introduction to the inertial navigation sensors, explaining their fundamental operating principles. Additionally, it outlines how position estimates are obtained by integrating acceleration and angular velocity measurements, including the necessary coordinate transformations to convert the state of the moving body from the body frame to the navigation frame. Finally, it discusses how these state estimates diverge from the true state of the body over time.

2.4.1 Working Principles of Accelerometers and Gyroscopes

This section briefly describes the working principle of measuring linear acceleration and angular rate changes in a moving body via mechanical inertial navigation sensors. Furthermore, it outlines the basic scheme by which Micro-Electro-Mechanical Systems (MEMS) inertial navigation sensors operate, based on [31]. This introduction is divided into two sections: *Accelerometers* and *Gyroscopes*.

Accelerometers are used to measure linear accelerations $\boldsymbol{a}$ along each axis of a moving body, that are generated when forces are acting on it. The basic principle of detecting such accelerations involves measuring the displacement Δx of a probe body with a known mass m suspended by springs with known spring rates k. This displacement occurs due to the forces acting on the mass, allowing it to be directly correlated to acceleration through Newton's second law:

$$\boldsymbol{F} = m\boldsymbol{a} = k\Delta\boldsymbol{x}\,. \tag{2.31}$$

Today, the most popular type of accelerometers are MEMS accelerometers, which can be found in nearly all electronic devices. The basic principle involves a micromechanical structure containing a mass that is engineered into a silicon wafer and held by spring-like structures surrounding it. The mass is suspended by springs and can move when the body to which the accelerometer is attached is in motion. The displacement caused by dynamic forces can be measured using different methods, such as capacitive, piezoresistive, or piezoelectric effects. These electrical signal than are converted to the acceleration which is outputted in units of $\mathrm{m/s^2}$ or g, the gravitational acceleration and corresponds to $9.81\mathrm{m/s^2}$.

Gyroscopes, on the other hand measure the angular change rate ω of the respective roll

ϕ, pitch θ, and yaw ψ angles around each of the three axis x, y and z of the body. This allows for the detection of the angular velocity of the motion, which is needed to transform coordinates from the body frame to the navigation frame. The working principle of MEMS gyroscopes is based on detecting Coriolis acceleration, which acts upon a vibrating proof mass perpendicular to the axis of rotation when a rotational force is applied. The detected acceleration enables the calculation of angular velocity and changes in angle.
The core of the MEMS sensor is an oscillating mass suspended within the sensor by micromachined spring-like structures. Unlike linear accelerometers, it must be continuously driven to maintain its oscillation. Similar to accelerometers, the experienced acceleration is detected through various electrical displacement measurement techniques, allowing for the calculation of angular velocity. The output is typically measured in degrees per second, which, when integrated once and given a known initial angle, allows for the calculation of the rotated angle.

2.4.2 Position Derivation via Inertial Navigation Sensors

Position information can be derived from known accelerometer and gyroscope measurements. This is obtained by integrating twice the acceleration over time

$$\boldsymbol{x}(t) = \iint \boldsymbol{a}(t)dt + \int \boldsymbol{v}_0 dt + \boldsymbol{x}_0 \tag{2.32}$$

Since acceleration measures only linear forces, the measured angular velocities $\boldsymbol{\omega}$ from the gyroscopes can be used to reconstruct the roll ϕ, pitch θ, and yaw ψ angles of the moving platform. This requires an integration step to obtain the resulting angles from the measured angular velocities $\boldsymbol{\omega}$ about each respective axis. With this information about dynamic motion and heading, a coordinate transformation can be applied to obtain the position and heading estimate in the desired navigation frame N. The explicit transformation and integration steps are provided in the following section. The IMU measurements are taken in the body frame, which are denoted with b, as the sensors move with the body. However, the desired position is in the navigation frame N. To obtain the position in the navigation frame from the raw measurements of the IMU in the body coordinate system, the gyroscope measurements must first be integrated.
This integration is typically done using an *Euler* integration step, as the sensor measurements are provided at discrete time intervals. The integration scheme can be stated as

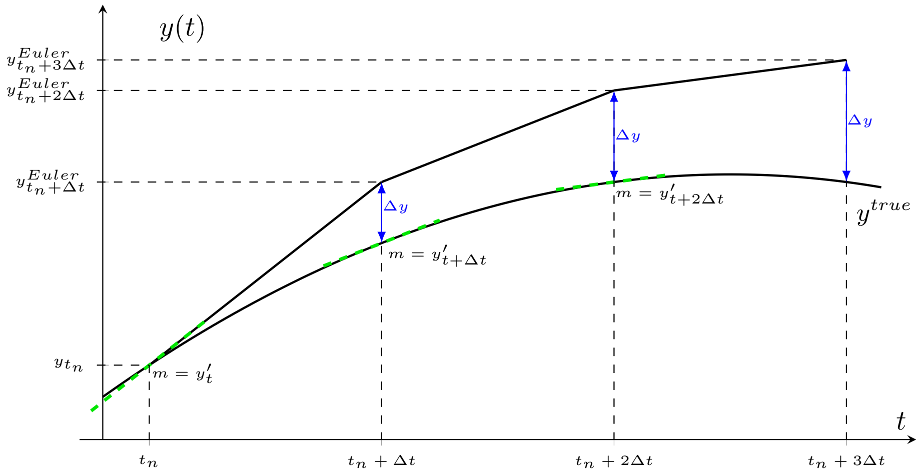

Figure 2.16: *Euler* step integration. The discrete measurements y'_t are integrated over equidistant time intervals Δt to compute the desired quantity y_t.

follows:

$$y^{Euler}_{t+\Delta t} \approx y_t + y'_t\,\Delta t\,, \tag{2.33}$$

where y'_t is the quantity to be integrated, y_t is the state prior to the integration step and Δt the integration step interval. In the case of measuring angular velocity and calculating the angle, y'_t represents angular acceleration $\boldsymbol{\omega}$, and Δt is the time interval between the measurements at hand. The resulting angles are as follows

$$\phi_{t+\Delta t} = \phi_t + \omega^x_t\,\Delta t\,, \tag{2.34}$$
$$\theta_{t+\Delta t} = \theta_t + \omega^y_t\,\Delta t\,, \tag{2.35}$$
$$\psi_{t+\Delta t} = \psi_t + \omega^z_t\,\Delta t\,. \tag{2.36}$$

After integrating the angular velocities, the *Euler* angles ϕ, θ, and ψ between the body frame and the reference frame are determined. A schematic illustration of the body and navigation frame, along with the angles between them, can be seen in Figure 2.17.
These angles are then used to perform a coordinate transformation that aligns the axes of both frames. This can be done by sequentially rotating each axis by its respective angle.

These rotations can be mathematically described using the following rotation matrices:

$$\boldsymbol{R}_x(\phi) = \begin{pmatrix} 1 & 0 & 0 \\ 0 & \cos(\phi) & -\sin(\phi) \\ 0 & \sin(\phi) & \cos(\phi) \end{pmatrix} , \tag{2.37}$$

$$\boldsymbol{R}_y(\theta) = \begin{pmatrix} \cos(\theta) & 0 & \sin(\theta) \\ 0 & 1 & 0 \\ -\sin(\theta) & 0 & \cos(\theta) \end{pmatrix} , \tag{2.38}$$

$$\boldsymbol{R}_z(\psi) = \begin{pmatrix} \cos(\psi) & -\sin(\psi) & 0 \\ \sin(\psi) & \cos(\psi) & 0 \\ 0 & 0 & 1 \end{pmatrix} . \tag{2.39}$$

The three rotation matrices can be multiplied together to form a single transformation matrix. The resulting coordinate transformation matrix $\boldsymbol{R}_b^N$ which aligns the body frame with the navigation frame, is given by:

$$\boldsymbol{R}_b^N = \boldsymbol{R}(\phi, \theta, \psi) = \boldsymbol{R}_z(\psi)\boldsymbol{R}_y(\theta)\boldsymbol{R}_x(\phi) \tag{2.40}$$

$$= \begin{bmatrix} c(\theta)c(\psi) & c(\theta)s(\psi) & -s(\theta) \\ s(\phi)s(\theta)c(\psi) - c(\phi)s(\psi) & s(\phi)s(\theta)s(\psi) + c(\phi)c(\psi) & s(\phi)c(\theta) \\ c(\phi)s(\theta)c(\psi) + s(\phi)s(\psi) & c(\phi)s(\theta)s(\psi) - s(\phi)c(\psi) & c(\phi)c(\theta) \end{bmatrix} , \tag{2.41}$$

where $s(\cdot)$ and $c(\cdot)$ are standing for $\sin(\cdot)$ and $\cos(\cdot)$ respectively.

When the correct rotation matrix for each time is calculated and the navigation frame is considered an inertial coordinate frame, accelerations $\mathbf{a}_N$, velocities $\mathbf{v}_N$, and positions $\mathbf{x}_N$ of the moving body in navigation frame can be determined using the following equations:

$$\boldsymbol{a}_t^N = \boldsymbol{R}_{b,t}^N \, \boldsymbol{a}_t^b \, , \tag{2.42}$$

$$\boldsymbol{v}_{t+\Delta t}^N = \boldsymbol{v}_t^N + \boldsymbol{a}_t^N \Delta t \, , \tag{2.43}$$

$$\boldsymbol{x}_{t+\Delta t}^N = \boldsymbol{x}_t^N + \boldsymbol{v}_t^N \Delta t - \boldsymbol{t}_{b,t=0}^N \, . \tag{2.44}$$

where $\boldsymbol{a}^b$ is the acceleration in the body frame and $\boldsymbol{t}_{b,t=0}^N$ is the initial translation vector at time $t = 0$ that describes the initial position of the body in the navigation frame.

When a rotating navigation frame, such as the Earth-centered Earth-fixed (ECEF) coordinate system, which is centered at the Earth's center and rotates with the Earth's rotation $\boldsymbol{\omega}$ around its axis, is used, the equations do not hold true, and pseudo-accelerations must be

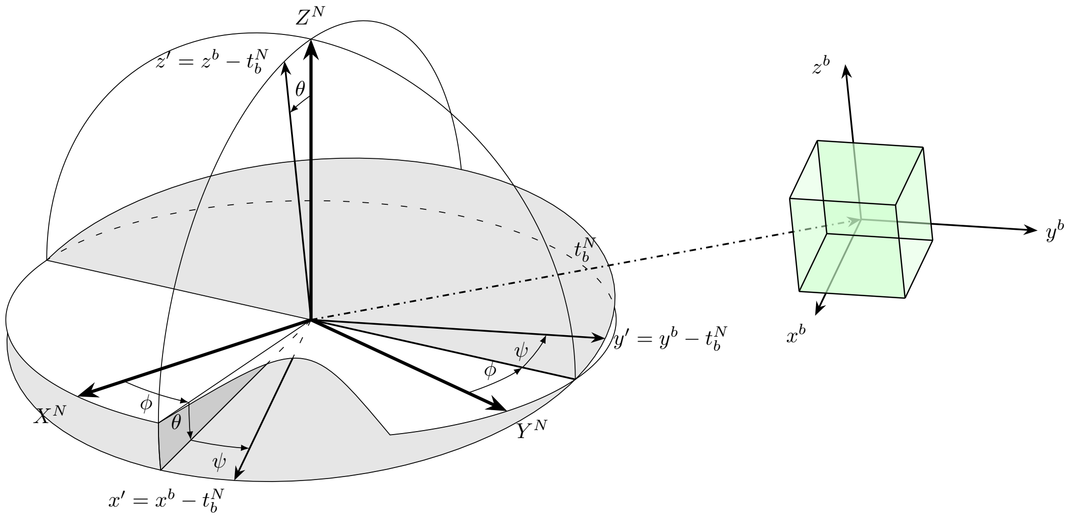

Figure 2.17: Schematic of the relationship of the navigation frame N and the body frame b. To convert measurements from the body frame, where linear acceleration and angular velocities are recorded, to the navigation frame, a coordinate transformation is required. This involves a rotational transformation via the rotation matrix $\boldsymbol{R}_b^N$. The position in the body frame represents the desired position estimate for navigation.

included. This gives the following result for the acceleration:

$$\boldsymbol{a}^N = R_b^N \boldsymbol{a}^b - \boldsymbol{\omega} \times \boldsymbol{v}^N - \boldsymbol{\omega} \times (\boldsymbol{\omega} \times \boldsymbol{x}^N)\,, \tag{2.45}$$

where the $\boldsymbol{\omega} \times \boldsymbol{v}^N$ term represents the Coriolis term and $\boldsymbol{\omega} \times (\boldsymbol{\omega} \times \boldsymbol{x}^N)$ represents the centripetal force, both of which need to be subtracted from the experienced body accelerations.

2.4.3 Position Errors due to INS

There are primarily two error types that occur when calculating the position only by using IMU measurements. One type of error arises from the sensor and its measurements themselves. This include measurement biases that still persist even after calibration, drift, which is essentially a time-varying bias caused by factors such as temperature fluctuations, electromagnetic interference, and other environmental influences that add random noise signal upon the true signal.

The second source of error is the accumulation of integration errors. Integration in discrete time is an approximation, where each step approximates the state forward in time. This process leads to errors that accumulate over time, which is known as integration drift. Integration in discrete time is typically done by using an *Euler* integration step, seen in Equation 2.33. The error of an Euler step is typically scaling by the square of the integration step width Δt and hence given by:

$$\epsilon_t^{Euler} = y_t^{Euler} - y_t^{true} = \mathcal{O}\left(\Delta t^2\right) \tag{2.46}$$

Furthermore, transitioning from acceleration to position requires two integration steps, making the method even more prone to these integration errors.

There are different grades of IMU for various applications. Depending on the application, drift, noise, and price vary significantly. IMUs are typically categorized into four different classes based on their performance. The position errors are usually expressed in $\mathrm{km/hr}$. The following performance numbers and prices are taken from [32]:

- The highest grade called strategic-grade IMU, possesses a position drift of less than $0.03\mathrm{km/hr}$ and typically costs over $1\ \mathrm{Mio\,USD}$.
- Navigation-grade IMU, commonly used in aircraft, has a drift rate of approximately $2\mathrm{km/hr}$ and costs around $100\ \mathrm{kUSD}$.
- Tactical-grade IMU has a drift rate of approximately 20-$40\ \mathrm{km/hr}$ and the price ranges around $10\ \mathrm{kUSD}$.
- The commercial-grade IMU has a drift rate that exceedes $40\ \mathrm{km/hr}$ and cost around a few $100\ \mathrm{USDs}$.

2.5 The Unscented Kalman Filter

An important aspect of the navigation aiding algorithm used in this work is sensor fusion. This technique combines position estimates from various sensors to provide a more accurate and reliable estimation. In this work, sensor fusion is used to integrate position estimates from inertial sensors with those derived from mapping magnetic field measurements to obtain more robust positions. The following theoretical introduction into the KF (Kalman Filter) is based on [33] and [34].

2.5.1 Fusion of Estimates

The sensor fusion process involves the combination of different types of estimates and sensor data. Many approaches exist for this, such as Particle Filters and non-linear Bayesian filters [35].

One distinct method for non-linear Bayesian filtering is the Unscented Kalman Filter (UKF). In contrast to other filtering methods, UKF uses specifically chosen sample points to represent the underlying distributions, characterized by their mean and covariance matrices. This sampling process to generate the respective sampling points is known as the Unscented Transform (UT), which sampling scheme is presented in more detail in later section.

The KF generally consists of a prediction step and an update step. Hereby, the prediction step is used to predict the state by propagating the initial state in time t according to the state transition function F of the process model. The second step is the update step which uses the measurement model to incorporate the measurement state with the propagated state prediction.

Process Model

The state $\mathbf{X}_t$ is propagated by the process model. The mathematical description of this model is as follows:

$$\mathbf{X}_{t+1|t} = \mathbf{F}\mathbf{X}_{t|t} + \mathbf{q}_t \, , \; \mathbf{q}_t \sim \mathcal{N}\left(0, \mathbf{Q}_t\right) \; . \tag{2.47}$$

Here, the state is propagated by the function $\mathbf{F}$, and is perturbed by the process noise $\mathbf{q}_t$ that follows an assumed normal distribution with zero mean and covariance $\mathbf{Q}_t$.

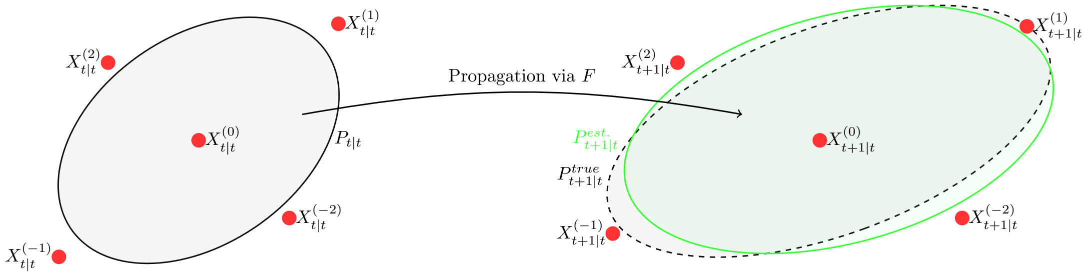

Figure 2.18: Schematic illustration of a two-dimensional distribution function that gets propagated by function F in time t. The UKF samples the Probability Density Function (PDF), and passes the samples points $\mathbf{X}_{t|t}^{(\pm i)}$ through F. Each sampling point hereby gets an assigned weight $w^{(\pm i)}$. The propagated sampling points $\mathbf{X}_{t+1|t}^{(\pm i)}$ and there weights are used to estimate the propagated PDF.

Measurement Model

The measurement model describes how the sensor measurement relates to the state. Mathematically, this is described as follows:

$$\mathbf{z}_{t+1} = \mathbf{H}\mathbf{X}_{t+1|t}^{true} + \mathbf{r}_t \, , \; \mathbf{r}_t \sim \mathcal{N}\left(0, \mathbf{R}\right) \, , \tag{2.48}$$

where $\mathbf{z}_t$ is the measurement at time t, $\mathbf{H}$ is the measurement matrix that maps the true state $\mathbf{X}_{t+1|t}^{true}$ into the measurement space, and the measurement is disturbed by the measurement noise vector $\mathbf{R}$.

2.5.2 Unscented Transform

In contrast to other filters, the UKF propagates the probability distribution of the state by sampling it in a specific order. It tries to capture information about the whole PDF by using only a few carefully chosen points and their corresponding weights. These sampling points are then propagated through a non-linear propagation function $\mathbf{F}$ of the process model. The sampling of the underlying distributions, known as the UT, is generally performed using the following sampling scheme:

$$\mathbf{X}^{(0)} = \boldsymbol{\mu}_X \, , \qquad \mathbf{X}^{(\pm i)} = \boldsymbol{\mu}_X \pm \left[\sqrt{n+\lambda}\mathbf{S}_X\right]_i \, , \tag{2.49}$$

where n is the number of dimensions of the state vector $\mathbf{X}$ and therefore also the dimension of the probability distribution to be sampled. S_X being the Cholesky decomposed covariance matrix $\mathbf{P}_X = \mathbf{S}_X\mathbf{S}_X^T$ of the state covariance.

$$w^{(0)}_{mean} = \frac{\lambda}{n+\lambda}\,, \qquad w^{(\pm i)}_{mean} = \frac{1}{2(n+\lambda)}\,, \tag{2.50}$$

$$w^{(\pm i)}_{mean} = \quad w^{(\pm i)}_{mean} = \frac{1}{2(n+\lambda)}\,,\ i = 1,\ldots,n \tag{2.51}$$

In addition, λ is the parameterized scaling factor that not only affects the spread of the sampling points $X^{(\pm i)}$ from the mean $X^{(0)}$ as can be seen in Equation 2.49 but also the weighting $w^{(\pm i)}$ of each sampling point. Here, this scaling factor is calculated as follows:

$$\lambda = \alpha^2(n+\kappa) - n\,, \tag{2.52}$$

where the constant α is a parameter scaling the distance from the mean of the PDF.
The sampling points $\mathbf{X}^{(i)}$ are used to propagate the state probability distribution through $\mathbf{F}$. Once propagated, the points passed through $\mathbf{F}$ are used to estimate the resulting probability function. The mean $\mathbf{X}^{(0)}_{t+1|t}$ and the covariance $\mathbf{P}_{t+1|t}$ follow from the following equations:

$$\mathbf{X}^{(0)}_{t+1|t} \approx \sum_{i=-n}^{n} w^{i}_{mean}\left(\mathbf{F}\mathbf{X}^{(i)}_{t|t}\right)\,, \tag{2.53}$$

$$\mathbf{P}_{t+1|t} \approx \sum_{i=-n}^{n} w^{i}_{cov}\left(\mathbf{F}\mathbf{X}^{(i)}_{t|t}\right)\,. \tag{2.54}$$

An illustration of the scheme using two-dimensional PDF is shown in Figure 2.18. Here, the grayed initial distribution is sampled as mathematically described above. Once fully sampled and the weights are determined, the sampling points are propagated through the process function, which describes the underlying dynamics of the system. After all sampling points have passed through the function $\mathbf{F}$, the propagated distribution (green) is estimated by taking the weighted sum of the resulting sampling points.

2.5.3 Kalman Gain and Updates

The updating of the propagated state is done by computing a so-called Kalman gain $\mathbf{K}$. Hereby, the relation between the propagated state covariance and the measurement covariance is used to derive a factor, with which the measurement state and the predicted state are fused to maximize the state probability and minimize the state covariance. The Kalman gain matrix is calculated by the following equation:

$$\mathbf{K}_{t+1} = \frac{\mathbf{P}_{t+1|t}\mathbf{H}'}{\mathbf{H}\mathbf{P}_{t+1|t}\mathbf{H}' + \mathbf{R}_{t+1}} \,. \tag{2.55}$$

Once the weight matrix $\mathbf{K}_{t+1}$ has been calculated, the state vector $\mathbf{X}_{t+1|t}$ is updated as follows:

$$\mathbf{X}_{t+1|t+1} = \mathbf{X}_{t+1|t} + \mathbf{K}_{t+1}\left(\mathbf{z}_{t+1} - \mathbf{H}\mathbf{X}_{t+1|t}\right) \,. \tag{2.56}$$

Consequently, the covariance matrix $\mathbf{P}_{t+1|t}$ of the state $\mathbf{X}_{t+1|t+1}$ is updated by the following equation:

$$\mathbf{P}_{t+1|t+1} = \mathbf{P}_{t+1|t} + \mathbf{K}_{t+1}\mathbf{H}\mathbf{P}_{t+1|t} \,. \tag{2.57}$$

The updated state $\mathbf{X}_{t+1|t+1}$ and the respective covariance matrix $\mathbf{P}_{t+1|t+1}$ contain all available information about the state at time $t+1$. Hereby, the state represents the optimal state which minimizes the state uncertainty.

2.6 Kriging Interpolation

The *Kriging* interpolation method is used to create continuous, complete maps of various geophysical quantities based on a sparse set of sample points. It is often employed to reduce the number of sampling points required to generate a fully sampled map. Unlike classical interpolation methods, which often rely only on data from the nearest neighbors, *Kriging* uses a weighted linear combination, with weights proportional to the spatial correlation between data points to provide more accurate interpolation.

The method is divided into two steps. In the first step, a so called variogram of the known data points is calculated, representing the spatial covariance between the known locations. With this spatial information, the second step derives weights for each known data point relative to the unsampled location, based on the correlation information. The following section is based on the paper of Li *et al.* [36].

The variogram γ is calculated by computing the covariance between each pair of sampled points. The lag distance, which is the unit distance of the spatial separation between pairs of points, plays a crucial role in this calculation. The variogram is explicitly defined as the half of the variance between measurement $z(\cdot)$ at point x and $x + lag$:

$$\gamma(x, lag) = \frac{1}{2} Var\left[z(x) - z(x + lag)\right] \tag{2.58}$$

To find the variogram that depends solely on the lag distance between points, eliminating the dependency on specific location x, the variograms of all location pairs with known measurements are grouped by their lag distance. By taking the mean of the variogram values for each lag, the resulting variogram becomes a function only dependent on lag, $\gamma(lag)$. Additionally, theoretical variograms can be fitted using different methods, each describing a different spatial correlation curve. The most common is the *Gaussian* variogram, defined as follows:

$$\gamma(lag) = C_0 + C\left(1 - \exp\left\{-\frac{lag}{a}\right\}\right) \tag{2.59}$$

Here, the parameter C_0 represents the nugget, C is the so-called arch height, and $C_0 + C$ is often referred to as the sill. The parameter a denotes the range. The range defines the boundary between correlated and uncorrelated lag distances. The nugget corresponds to the variogram value at *lag* zero, while the sill represents the value at which the variogram levels off. An illustration of the different variograms and their curves, using the same sill and range values, is shown in Figure 2.19.

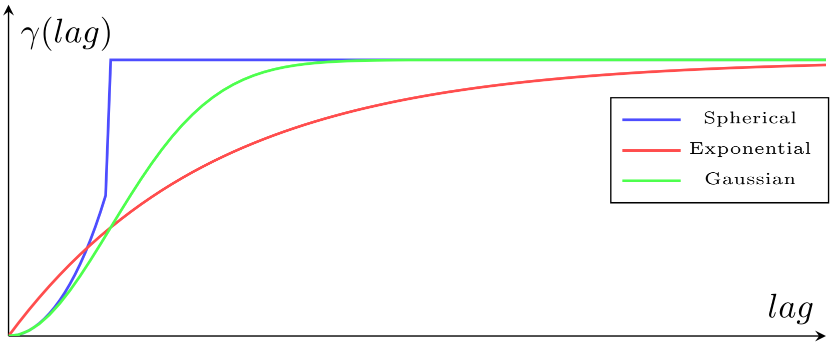

Figure 2.19: Illustration of the variograms for the different methods. The point where the variogram exceeds the threshold represents a lack of spatial correlation, meaning that lag distances greater than the range do not influence the data.

Furthermore, an experimental variogram $\gamma^\star$ can be constructed using the given sampled points and their respective measurements. Hereby, the variance is calculated by the sum of squared differences for all point pairs with a certain *lag*:

$$\gamma^\star = \frac{1}{2\,N(lag)} \sum_{i}^{N(lag)} \left[z(x_i) - z(x_i + lag)\right]^2 \, . \tag{2.60}$$

By computing the experimental variogram of the sparse map to be interpolated, one can use the theoretical variograms to find the best-fitting theoretical variogram. Once a fitted variogram with the optimal parameters, which best resembles the experimental variogram, is found, a system of linear equations can be set up. For this linear equation system, the results of the fitted variogram between all possible pairs of locations with known measurements x_i for $i \in 1,..,n$ are needed. Furthermore, the result of the variogram for the location x_0 for which the measurement should be calculated, with respect to all known measurement locations x_i, must also be computed. With these values obtained the desired weights λ_i can be calculated by solving the following system of linear equations:

$$\begin{bmatrix} \gamma(x_1,x_1) & \gamma(x_1,x_2) & \dots & \gamma(x_1,x_n) & 1 \\ \gamma(x_2,x_1) & \gamma(x_2,x_2) & \dots & \gamma(x_2,x_n) & 1 \\ \vdots & \vdots & \ddots & \vdots & \vdots \\ \gamma(x_n,x_1) & \gamma(x_n,x_2) & \dots & \gamma(x_n,x_n) & 1 \\ 1 & 1 & \dots & 1 & 0 \end{bmatrix} \begin{bmatrix} \lambda_1 \\ \lambda_2 \\ \vdots \\ \lambda_n \\ \mu \end{bmatrix} = \begin{bmatrix} \gamma(x_1,x_0) \\ \gamma(x_2,x_0) \\ \vdots \\ \gamma(x_n,x_0) \\ 1 \end{bmatrix} . \tag{2.61}$$

The term μ is a Lagrange multiplier used to incorporate the constraint that the sum of the weights should be equal to one, $\sum_i \lambda_i = 1$. The prediction $\hat{z}(\mathbf{x}_0)$ at the unsampled point $\mathbf{x}_0$, given the calculated weights λ_i, is computed than as follows:

$$\hat{z}(\mathbf{x}_0) = \sum_{i=1}^{N} \lambda_i z(\mathbf{x}_i)\,. \tag{2.62}$$

This scheme of calculating the estimation is further illustrated in Figure 2.20 (b). Here, the gray squares represent locations where the measurements are known, while the green square indicates the location at which the measurement should be estimated. After fitting a variogram for the given map and calculating the variogram results between all pairs of known locations, as well as between all known locations and the location to be estimated, the linear equation in Equation 2.61 can be solved. This leads to the respective weight for each known location, which is used in the estimation of the measurement at location x_0. By traversing all unknown locations and calculating the estimated measurements using the described procedure, one can construct a fully sampled map.

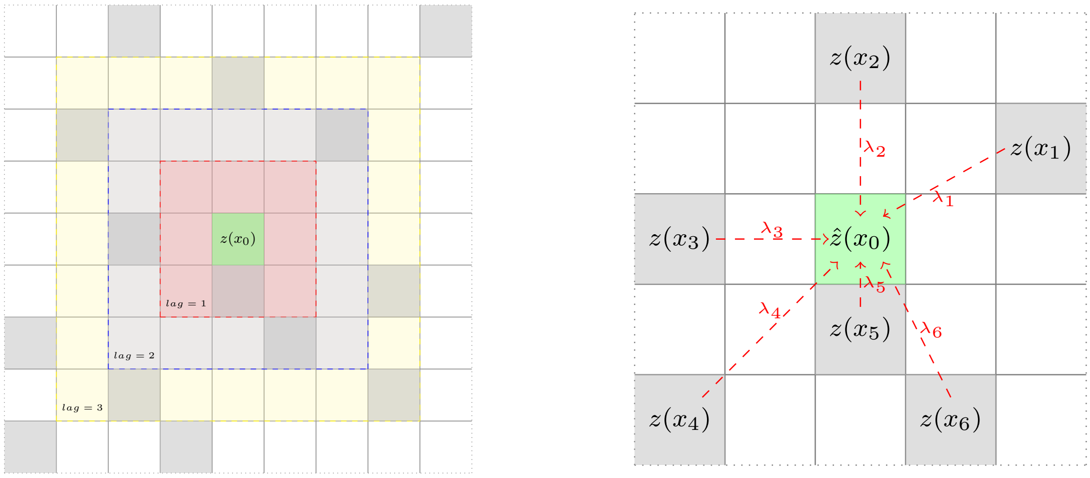

(a)

(b)

Figure 2.20: (*Left*) Extent of each lag distance to the location x_0. (*Right*) Scheme for calculating the unknown measurement $\hat{z}(x_0)$ based on the known measurements at locations $\mathbf{x}_i$ using the *Kriging* algorithm. The spatial correlation between the known measurements and the missing locations is used to compute the corresponding weights λ_i which are then used to estimate a measurement $\hat{z}$ at the unknown location x_0.

2.7 Performance Metrics of Sensors

The performance of a sensor is generally quantified by a few key metrics. Important metrics for inertial navigation sensors and magnetometers include the following:

Bias describes the constant offset between the measured value and the actual quantity measured. Biases can arise due to many different external factors, such as temperature changes of the sensor, which in this case leads to a constant offset. However, bias can often be eliminated by calibration.
For example, for inertial navigation sensors static calibration can eliminate the offsets of the accelerometers and gyroscopes, when the sensor is known to stand still.
Magnetometers can be calibrated by measuring the absolute magnetic field or by precisely defining the magnetic field the sensor is expected to experience. For example, Meritt coils are used in highly shielded, quiet environments to counteract the Earth's magnetic field near zero, while a second three-dimensional coil array creates a predefined magnetic field.

Drift typically refers to the change in the output of a sensor when the input signal remains constant. This phenomenon is often described as a time-varying bias that has not been compensated for during calibration. However, drift can be mitigated by understanding how factors such as time, temperature, and other external influences affect the measurements. By modeling these effects, drift can be compensated for through post-processing techniques to a certain degree. However, the less drift a sensor has, the better. Further, in magnetometry for space application usually Fluxgate magnetometers are deployed accompanied by QM for drift mitigation. Hereby based on the measurements of the QM the fluxgate sensors are recalibrated during deployment.
One method of characterizing and quantifying the types of drift and noise of a sensor is through the Allan Deviation (AD) analysis [37]. This method computes the variance $\sigma^2_{AD}(\tau)$ over different averaging time lengths τ of the sensor time series recorded, resulting in a graph where distinct slope regions indicate various types of sensor drift. For this, the time series is divided into N adjacent intervals, indexed by $n \in \{1, .., N\}$, each with a sample length τ. The difference between the means of each subsequent interval is then calculated, squared, and averaged [38]. Mathematically this is done as follows:

$$\sigma_{AD}(\tau) = \sqrt{\frac{1}{2}\left\langle (\tilde{y}_{n+1} - \tilde{y}_n)^2 \right\rangle}\,. \tag{2.63}$$

The interval length τ ranges from a minimum of one sample to a maximum of half the total length of the time series. Figure 2.21 shows a graph illustrating the different types of drift that can be derived from the calculated AD.

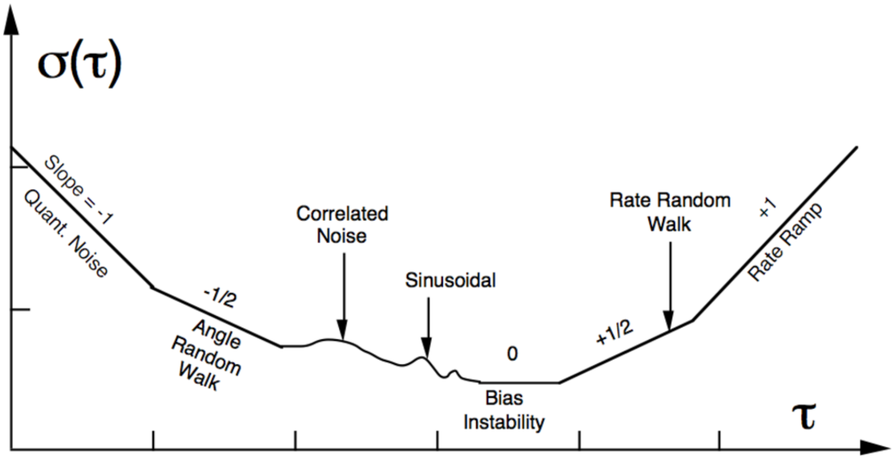

Figure 2.21: Alan Deviation in log-log scale. The distinct regions with varying slopes help identify the different types of noise present in the sensor's time-series data.[39]

In this log-log plot, white noise is identified in the region where the graph has a slope of $m = -0.5$, showing that *Gaussian* white noise is present. Furthermore, the bias instability, which determines the intrinsic drift rate without any external disturbances, is found near the minimum of the graph, where the slope is equal to $m = 0$. The bias instability can be read directly from the y-axis at the point where this condition is satisfied. In addition, the drift rate, which is specific to each measurement, can be found in the region where the AD plot slopes upwards with a slope of $m = 1$. This measure incorporates further drifts caused by external influences.

Noise is defined as any variation in the measurement that does not originate from the actual quantity being measured. It can arise from environmental disturbances, interference from other devices or sensors, or come from the sensor itself. A key difference between noise and other systematic errors, such as biases and drift, is that noise is random and therefore not predictable. This type of noise is also known as stochastic noise.

Noise can be quantified in the time domain using methods such as AD analysis as described prior. In the frequency domain, more prominent methods include the Power Spectral Density (PSD) analysis which quantifies the distribution of noise power across different frequencies. The time series to be evaluated is divided into n segments of equal length. For each of the n segments, the Fourier Transform is calculated, which transforms the data from the time domain into the frequency domain. Afterward, the amplitude of each frequency bin is squared, and the mean of these squared values is taken to calculate the power. By analyzing the PSD, one can quantify the power of each respective frequency component of the time series. This information can then be used to minimize noise signals through a suitable filter, which reduces the unwanted noise signal form the measurement.

Further, an often-used quantity derived from measurements is the Signal-to-Noise Ratio (SNR), which is equivalent to the power ratio between the true signal and the noise signal or the ratio of the respective amplitudes:

$$\text{SNR} = \frac{P_{\text{signal}}}{P_{\text{noise}}} = \frac{\sigma^2_{\text{signal}}}{\sigma^2_{\text{noise}}} = \frac{A_{\text{signal}}}{A_{\text{noise}}} \tag{2.64}$$

The higher the SNR, the better the sensor can distinguish the true signal from the noise. Mathematically, this is equivalent to calculating the ratio of powers, the ratio of variances, or, alternatively, the ratio of amplitudes between the signal and the noise of the measurement.

Sensitivity is a commonly used metric to quantify and compare the performance of different sensors. It defines the value of how small of a signal change the sensor can measure. In magnetometry, sensitivity is typically given in units of $\mathrm{T}/\sqrt{\mathrm{Hz}}$, which is derived from the calculated PSD and taken at the frequency of $1\ \mathrm{Hz}$.
An important aspect is that the sensitivity is limited by the environmental noise the sensor is experiencing. For example, if the noise level in the environment is higher than the sensor's sensitivity, it becomes difficult to distinguish between true variations in the measured quantity and variations caused by noise.

Resolution is also closely related to the noise and the sensitivity. Hereby resolution also often defined as the smallest measurable change in the physical quantity that the sensor can reliably detect. Further, there is also often two different resolutions defined: the *spatial resolution* and the *temporal resolution*.

The *spatial resolution* is usually limited by the sensor size and defines the limits of spatial variation it can resolve. The *temporal resolution* in other words describes how the sensor can pick up the temporal variation which is limited by the sampling frequency of the sensor.

2.8 Navigation Performance

The navigation performance metrics used in the later chapter, with which the results of the navigation aiding algorithm are presented and discussed, are outlined below.
The following three types of error are used: Maximum Absolute Error (ME), Mean Absolute Error (MAE) and Root-Mean-Square-Error (RMSE). In the following formulas, y_i represents the true values, $\hat{y}_i$ represents the predicted values, and n is the total number of observations. The predicted values can hereby be both, either the position estimates from pure INS navigation which is also known as the dead reckoning solution and the position estimates resulting from the magnetic field-aided navigation algorithm.

The ME is defined as follows:

$$\mathrm{ME} = \max_{i \in \{1,2,\ldots,n\}} |y_i - \hat{y}_i| \ , \tag{2.65}$$

which gives the maximal deviation within the observations. The MAE is calculated as follows:

$$\mathrm{MAE} = \frac{1}{n} \sum_{i=1}^{n} |y_i - \hat{y}_i| \tag{2.66}$$

gives a quantification of the mean error RMSE:

$$\mathrm{RMSE} = \sqrt{\frac{1}{n} \sum_{i=1}^{n} (y_i - \hat{y}_i)^2} \tag{2.67}$$

where y_i are the true values, $\hat{y}_i$ are the predicted values, n is the total number of observations.

3 Experimental Setup and Methodology

This chapter introduces the general methodology of the research conducted in this work. The planned experimental setup for the real-life implementation of the magnetic field-aided navigation algorithm is described, followed by a detailed explanation of the magnetic field-aided navigation scheme. This includes map matching, probability and covariance estimation, and the overall algorithm, with the map matching and covariance calculations based on the work by Wang *et al.* [10].

The simulation approach is then presented, covering both the laboratory experiment simulations and the real-flight path simulations. Finally, the general data acquisition and processing steps for magnetic navigation aiding in the experiment are outlined, including data collection from the sensor, the process of acquiring data for sensor noise and drift analysis, and the generation of the magnetic field map.

3.1 Experimental Setup of the Laboratory Experiment

A physical experimental setup was designed and constructed in the laboratory. The goal was to create a continuously moving platform with a known absolute position at all times, enabling the quantification of the stability and performance of the magnetic field-aided navigation algorithm in a real-life experiment.

To achieve this, a custom-designed, 3D-printed platform was mounted at each end of a $1\mathrm{m}$ carbon fiber rod, which holds the IMU and the magnetometers. The rod is horizontally mounted onto an aluminum post, which is then attached to a motorized rotation stage from *ThorLabs* that provides circular motion. The rotation stage is controlled by custom *Python* code, allowing for the specification of movement protocols, homing, and real-time position reading during operation. Furthermore, the setup consists of an arrangement of permanent neodymium magnets randomly placed on the base, where the rotation stage is also mounted. Cylindrical neodymium N35 magnets with a diameter of $5\mathrm{mm}$ and a height of $5\mathrm{mm}$ were chosen to create the magnetic field variations for the setup. The distance between the magnets and the magnetometers is approximately $20 - 30\mathrm{cm}$ to produce field variations of a few $\mu\mathrm{T}$. These specifications and the distance were determined based on prior simulations conducted using the *Magpylib* package [40] in *Python*. The simulations were designed to generate magnetic field ranges similar to those encountered during real-world travel over large distances on and above the Earth's surface. At the same time, the magnetic field gradient was kept below $300\mathrm{nT}/\mathrm{cm}$, which is the maximum gradient that the OPM can reliably measure. A rendering of the planned laboratory setup and its actual implementation is shown in Figure 3.1.

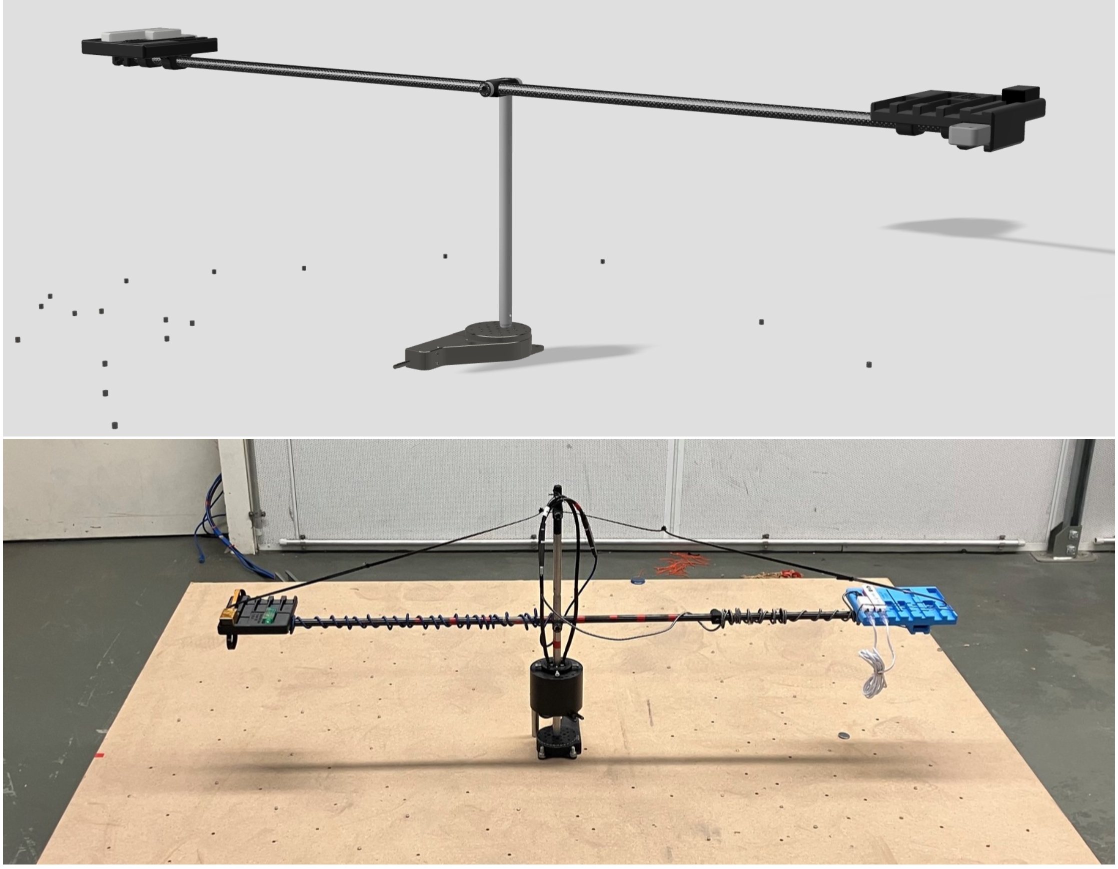

Figure 3.1: (*Top*) Rendering of the experimental setup used for rotating the platform on which the inertial sensor and magnetometers are mounted. (*Bottom*) Picture of the implemented laboratory setup.

3.2 Magnetic Field-Aided Navigation

The goal of this work is to take the first steps toward magnetic field-aided navigation and implement a navigation-aiding algorithm which corrects position estimates derived from INS by mapping and comparing the magnetic field measurements recorded, while in motion, to a pre-recorded magnetic field map. The following section describes the concepts of the implemented navigation algorithm.

3.2.1 Map Matching Problem

An important problem that needs to be overcome not only in magnetic field-aided navigation but also in all navigation schemes that utilize matching measurements and an underlying map is the so-called *map matching problem*. This problem refers to the issue that arises when more than one match between the measured quantity and the map at hand is found. This leads to signal ambiguity, causing uncertainty about which of these matched locations the signal originally arises from. Mathematically, one can model the sensor measurement

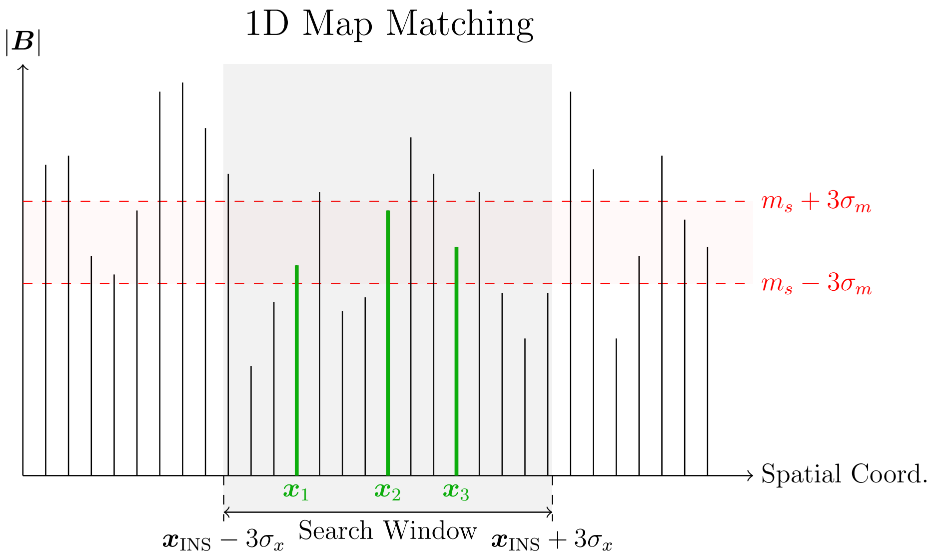

Figure 3.2: Illustrated is the scheme of how map matches are found on an one-dimensional example. Locations of matches x_i are considered when the magnetic field measurements $m(x_i)$ fall within the interval $m(x_i) \in [m_s - 3\sigma_m, m_s + 3\sigma_m]$ and are within the search window $x_i \in [x_{INS} - 3\sigma_x, x_{INS} + 3\sigma_x]$.

m_s as a *Gaussian* random variable following: $m_s \sim \mathcal{N}\left(m_0, \sigma^2_{\text{Mag.}}\right)$, where m_0 is the noiseless, true signal and $\sigma_{\text{Mag.}}$ is the standard deviation of the signal error due to the overall noises the magnetometer is experiencing.

To overcome this map ambiguity only candidate locations that fall within the interval with specified bounds around the magnetometer's magnetic measurement m_s and that are spatially bounded around the position estimate of the INS $\boldsymbol{x}_{\text{INS}}$ are considered as matches. This limits the location to the most likely locations, minimizing map matches at completely different locations. The locations of the matches that fall within the intervals are assigned as $\{\mathbf{z}_1, ..., \mathbf{z}_n\}$. An illustration of this map-matching scheme is found in a one-dimensional problem, as shown in Figure 3.2. It is important to set both spatial and measurement bounds appropriately to ensure that there are neither too many nor too few map matches. Therefore, the spatial bounds are defined as $\delta x = 3\sigma_x$, where σ_x is the standard deviation of the INS position estimate $\boldsymbol{x}_{\text{INS}}$. Similarly, the interval considered for the magnetic field measurement is based on the sum of the expected deviations from both the map and the sensor, yielding a total uncertainty of $\sigma_m = \sqrt{\sigma^2_{\text{Map}} + \sigma^2_{\text{Mag.}}}$. These bounds correspond to a confidence level of $\gamma = 99\%$ for both the spatial location and magnetic field measurements.

3.2.2 Probabilistic Data Association

The goal of the Probabilistic Data Association (PDA) is to calculate the most probable position given the set of position candidates of the map matching step. This step takes the list of candidate locations $\boldsymbol{Z}_n = \{\boldsymbol{z}_1, ..., \boldsymbol{z}_n\}$ in, that were found by *map matching* in search window around INS position estimate $\boldsymbol{x}_{\text{INS}}$. The probability weight of each candidate location $\boldsymbol{z}_i$ of $\boldsymbol{Z}_n$ is calculated as follows:

$$w_i = \frac{p\left(\boldsymbol{z}_i | \boldsymbol{x}_{\text{INS}}\right)}{\sum_{j=1}^{n} p\left(\boldsymbol{z}_j | \boldsymbol{x}_{\text{INS}}\right)}\,, \tag{3.1}$$

which is normalized such that the sum of the weights for each match equals 1. The conditional probability $p\left(\mathbf{z}_i | \mathbf{x}_{\text{INS}}\right) \sim \mathcal{N}(\mathbf{z}_i - \mathbf{x}_{\text{INS}}, \Sigma)$ follows a multivariate normal distribution. To reduce the set of multiple candidate positions to a single estimate, the weighted mean is computed:

$$\boldsymbol{z}_{\text{PDA}} = \bar{\boldsymbol{z}} = \sum_{i=1}^{n} w_i \boldsymbol{z}_i\,. \tag{3.2}$$

A schematic depiction of how map matching and the position estimate calculated by the PDA are related is shown in Figure 3.3.

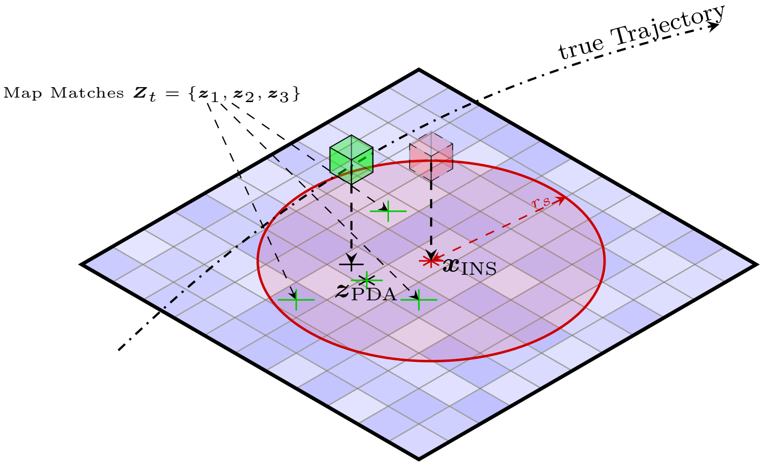

Figure 3.3: Illustrated is the working principle of the Map Matching process in two dimensions. The position estimate z_{PDA} of the IMU is used to define the search area of the map (red circle). The locations z_i are used to calculate the resulting map match by taking the weighted sum of the matched locations. The weight of each location is computed as stated in Equation 3.1.

The corresponding associated weighted variance is calculated by taking the average sum of the measurement covariance $\boldsymbol{R}_i$ and the spatial covariance of the location found:

$$\bar{\boldsymbol{R}} = \sum_{i=1}^{n} w_i \left[\boldsymbol{R}_i + (\boldsymbol{z}_i - \bar{\boldsymbol{z}})(\boldsymbol{z}_i - \bar{\boldsymbol{z}})^\top\right] . \tag{3.3}$$

The initial measurement covariance $\boldsymbol{R}_i$ represents the signal noise variance of the measurements in the immediate proximity of the location relative to the measurements at the location and is described in the next section in more detail.

3.2.3 Unscented Kalman Filter

As outlined, a UKF is used to fuse the position estimates obtained from the INS and the *map matching*. The *Process Model* and the *Measurement Model* of the UKF used in the implemented algorithm are defined in the following. Additionally, the *Process Noise* and

Measurement Noise are specified. Initially, the state $\boldsymbol{X}_t$ of the platform consists of the position vector $\boldsymbol{x}_t$, concatenated with the velocity vector $\boldsymbol{v}_t$ and the direction angle θ, forming the following state vector:

$$\boldsymbol{X}_t = (\boldsymbol{x}_t, \boldsymbol{v}_t, \theta_t) \ . \tag{3.4}$$

Process Model

The state is propagated by the *Process Model*. The mathematical representation of the process model is given by the Equation 2.47. This step of the UKF is also known as the *Prediction Step*. Here the state is propagated by the function $\boldsymbol{F}$ and perturbed by the process noise $\boldsymbol{q}_t$ which follows a normal distribution with zero mean and covariance $\boldsymbol{Q}_t$.

In the case of the underlying application of this thesis, the function $\boldsymbol{F}$ is a non-linear function and describes the integration steps taken via the *Euler* integration step to go angular velocities to the corresponding *Euler* angle used for the rotational transformation of the body accelerations from the body frame b to the navigation frame N. Furthermore, F contains the integration steps to go from the measured accelerations $\boldsymbol{a}_t$ of the platform to the velocities $\boldsymbol{v}_t$ and the positions $\boldsymbol{x}_t$ respectively.

Since only a motion in the horizontal plane is considered, this transformation is a simpler case of the three-dimensional case presented in Equation 2.41 and is given by the following:

$$\boldsymbol{R}_b^N = \begin{bmatrix} \cos(\theta) & -\sin(\theta) \\ \sin(\theta) & \cos(\theta) \end{bmatrix} \ . \tag{3.5}$$

The *Process Noise* $\mathbf{Q}_t$ results from the measurement noise of the accelerometers $\sigma^2_{\text{Acc.}}$ and gyroscopes $\sigma^2_{\text{Gyro.}}$ of the IMU used. The process covariance matrix has the following form:

$$\boldsymbol{Q}_t = \begin{pmatrix} \frac{1}{2}\sigma^2_{\text{Acc.}}\Delta t^4 & 0 & \frac{1}{3}\sigma^2_{\text{Acc.}}\Delta t^3 & 0 & 0 \\ 0 & 0.5\,\sigma^2_{\text{Acc.}}\Delta t^4 & 0 & \frac{1}{3}\sigma^2_{\text{Acc.}}\Delta t^3 & 0 \\ \frac{1}{3}\sigma^2_{\text{Acc.}}\Delta t^3 & 0 & \sigma^2_{\text{Acc.}}\Delta t^2 & 0 & 0 \\ 0 & \frac{1}{3}\sigma^2_{\text{Acc.}}\Delta t^3 & 0 & \sigma^2_{\text{Acc.}}\Delta t^2 & 0 \\ 0 & 0 & 0 & 0 & \sigma^2_{\text{Gyro.}}\Delta t^2 \end{pmatrix} \ . \tag{3.6}$$

Measurement Model

The fusion of position estimation of the magnetic field measurements and the map matching for the navigation aiding are described by the *Measurement Model* of the UKF. This step of the UKF is also known as the *Update Step*. The position estimate is based on the comparison of one of the magnetometer's signal measurements m_s with the magnetic field map $\mathcal{M}$. As described in the previous section on PDA, there is the possibility of multiple map matches, which are then combined to maximize the likelihood of the computed position estimate. The function $\mathbf{H}$ represents the map matching function, which maps the magnetic field measurement m_s to the map matched location $\boldsymbol{x}_{PDA}$.

The definition of *Measurement Noise* is not trivial in this case. Because the magnetic field measurements are in units of Tesla and the position is given in meters. There is also no direct link to calculate the uncertainty resulting from the map comparison step. Following the approach of Storms [41], the covariance matrix $\mathbf{R}_i$ of each individual location match is calculated by looking at neighboring locations and deriving a gaussian likelihood function with these neighboring measurements. The likelihood L of one neighboring location is calculated as follows

$$L(x_N; m_s) = \frac{1}{\sqrt{2\pi\sigma_m^2}} \exp\left(-\frac{(m_s - m(x_N))^2}{2\sigma_m}\right), \tag{3.7}$$

where the measured magnetic field m_s is subtracted from the magnetic field value $m(\boldsymbol{x}_N)$ of the neighboring location of the map match x_N. The standard deviation σ_m is the square root of the sum of the variances from the map σ^2_{Map} and the magnetometer $\sigma^2_{\text{Mag.}}$. By normalizing the likelihoods of all neighboring locations, the standard deviation σ_x of the resulting normalized *Gaussian* PDF is used to define a diagonal matrix representing the covariance matrix of the position match:

$$\boldsymbol{R}_i = \begin{pmatrix} \sigma_x^2 & 0 \\ 0 & \sigma_x^2 \end{pmatrix}. \tag{3.8}$$

The covariances obtained for each map match are considered and weighted to calculate the resulting covariance matrix of the PDA position estimate, as shown in Equation 3.3. In addition, as proposed by Wang *et al.* [10], the normalized *Map Variability* $V(\boldsymbol{x}_i)$ of the entire search radius is used to scale the measurement covariance. This quantity quantifies the degree of variability in the map and provides information on how much the map is changing and is calculated as follows:

$$V(\boldsymbol{x}_i) = \sum_i \left[z(x_i) - z(x_0)\right]^2 . \tag{3.9}$$

This results in a scaled measurement covariance of the following:

$$\boldsymbol{R} = V(\boldsymbol{x}_{\text{INS}})\bar{\boldsymbol{R}} , \tag{3.10}$$

where additional clipping is applied to ensure that the covariance is no smaller than the spatial dimension of a single pixel of the map.

3.2.4 Batch Estimation

Incorporating the position estimate from *Map Matching* is not performed at every map matching step. This is because an incorrectly matched position, if corrected at a high map matching rate, can lead to a divergent position estimate. In addition, the position estimate from the INS is sufficiently accurate over short time intervals, making frequent updates unnecessary. A more efficient approach is to fuse the map matches with the INS position estimate using a series of map matches, referred to as *batches* in this thesis, which are found along the trajectory. By combining these batches with the kinematic information of the state, more accurate and stable position estimates can be obtained. In the further course, this step is referred to as the *Batch Estimation Step*.

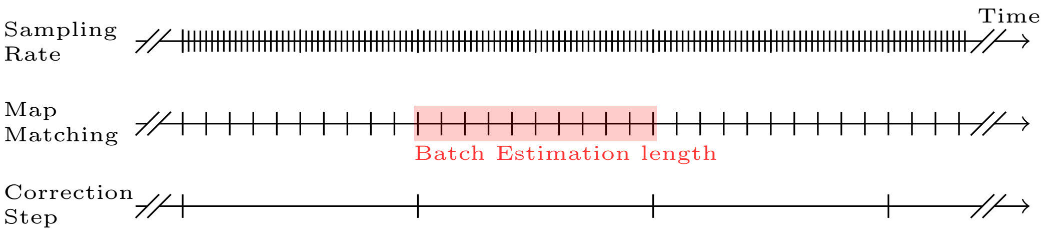

Figure 3.4: Illustrated is the relationship between the sampling rate, the map matching rate, and the correction step rate. The number of subsequently listed map match results used for one correction step is defined as the *Batch Estimation Length*.

The matches identified at each map matching step are stored along with the corresponding velocities and heading angle, as well as the map match covariances and state covariances.

An illustration of the magnetometer sampling rate, map matching rate and correction steps is shown in Figure 3.4, where the batch length is defined. The batch length indicates how many map matches are combined to obtain the resulting position estimate for correction. Once the specified batch length is reached, the batch estimation procedure is initiated. In this step, past map matches and their corresponding kinematic information are propagated over time and fused with the position estimate from the subsequent map match. This process is implemented using an additional UKF, which enables the propagation of covariance information alongside the position estimate by using the stored velocities. The schematic of this procedure is shown in Figure 3.5 for three consecutive steps. As described, the position estimate from the INS is used for map matching. The green crosses represent the map matches found for each step. The position estimates, which fuse the map matches, are denoted as z_{PDA}. Once a z_{PDA} and its covariance are propagated over time and space with the respective velocity, the propagated position estimate and the newly found position estimate from map matching are fused to minimize the covariance of the position estimates. The resulting position estimate from this single step of batch estimation is marked as a violet dot. This position estimate is then used for propagation in the next step of the batch estimation process. Once all the positions in the list of batches have been traversed, the final position estimate, incorporating all previous matches and kinematic information, is used to

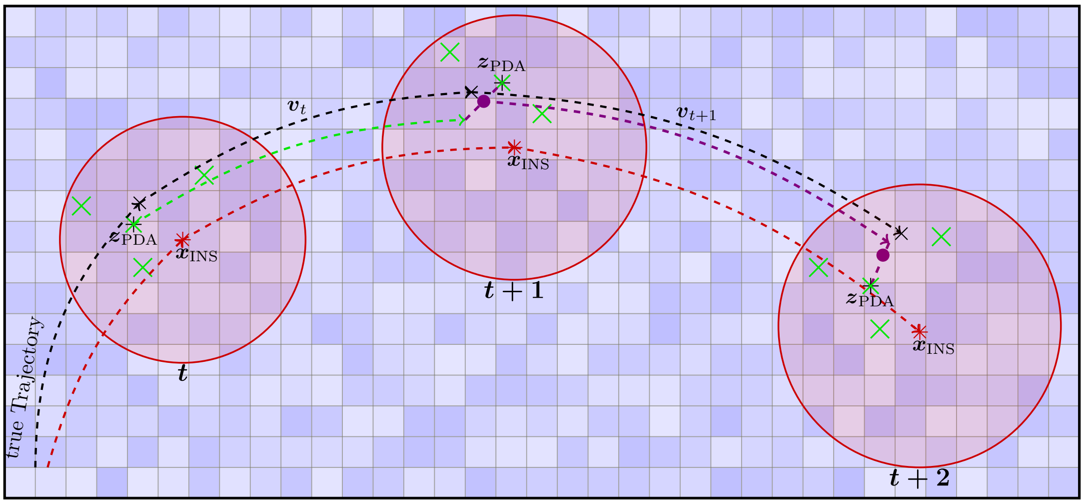

Figure 3.5: Illustrated is the Batch Estimation process for 3 subsequent steps. In black the true trajectory is visualized. The red trajectory shows the pure INS position estimate of, which diverges from the true trajectory. The green and following violet curve shows the resulting trajectory using map matching and batch estimation.

fuse the diverging INS position.

3.2.5 Overview of the Magnetic Field-Aided Navigation Algorithm

As each step has been described in detail, the entire algorithm process is now described step by step. A schematic flowchart of the algorithm is shown in Figure 3.6.

First, the accelerations $\boldsymbol{a}$ and angular velocities $\boldsymbol{\omega}$ are taken from the IMU. The preceding position is also available. The position propagation due to the dynamics measured by the IMU and the integration of the angular velocities is described in Section 2.4.2. This propagation occurs in the prediction step of the UKF, where the state covariance is also propagated over time.

Once the state estimate $\boldsymbol{X}^{t|t-1}$ with the corresponding covariance matrix $\boldsymbol{P}^{t|t-1}$ is computed from the INS, the position estimates $\boldsymbol{x}_{\mathrm{INS}}^{t}$ and the corresponding position covariance $\Sigma_{\mathrm{INS}}^{t}$ are extracted and used for map matching. The position estimate $\boldsymbol{x}_{\mathrm{INS}}^{t}$ is used as the central location of the circular search area. The covariance is used to calculate the search radius, the chosen radius being $r_s = 3\sigma_x$, within which the spatial bounds are set. The magnetometer measurements are then used to define the limits of the magnetic field interval for consideration of a match, requiring estimates of magnetometer noise $\sigma_{Magn.}$ and estimates of map noise σ_{Map} to define the interval within which a location is considered a match.
If more than one match is found, the multiple matches are merged into a single most likely map match by using PDA step. Once the map match and its resulting covariance have been computed, they are stored with the other state components in a list for *Batch Estimation*.

Until the specified batch length is reached, no update step of the UKF is performed to merge the position estimates of the INS and the map matching. This means that the state derived solely from the INS is used for the next subsequent time step and the whole process is repeated.

Once the specified batch length is reached, the list of map matches is traversed chronologically. Fusion is then performed in another UKF, where the map matches are propagated in time using the corresponding velocity and fused with the next map match. At the end of the batch estimation, the map match incorporates both the previous map match information and the kinematic information of the moving platform. This batch estimation result z_B^t is then considered as a position estimate for the update step of the magnetic navigation UKF to correct the state of the moving body. Not only the position estimate but also the corresponding covariance of the positions are updated in the updating step.

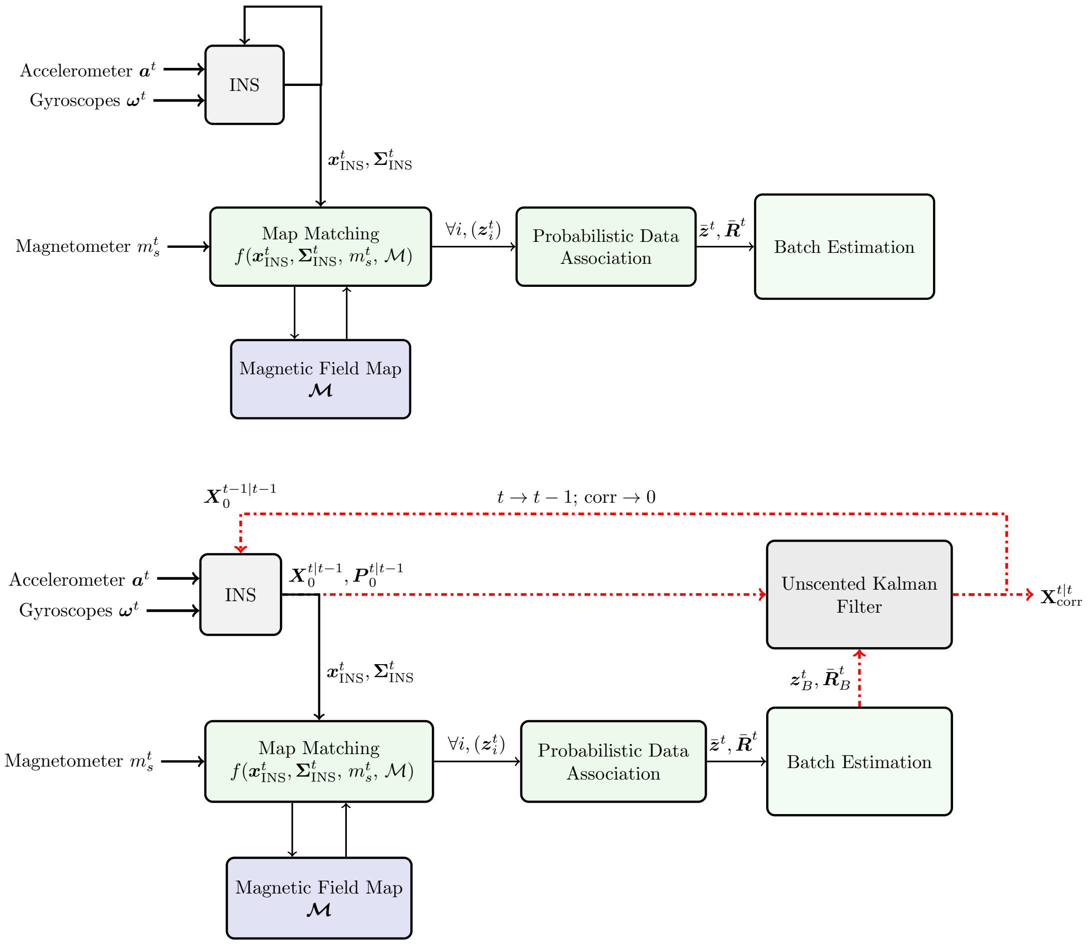

Figure 3.6: Schematics of the implemented magnetic field-aided navigation system based on map matching of magnetometer measurements to a magnetic field map. (*Top*) Time steps in which no correction step is performed: the INS position estimate is calculated solely based on the experienced accelerations and angular velocities. The resulting position estimate and its respective position covariance are provided for map matching. This step also incorporates the magnetic field measurements. Based on the map matches found, the most probable location of the measurements is calculated along with its covariance. These results, including the corresponding velocities, are saved for the batch estimation step for later propagation. The INS state estimate is then used for the next time step. (*Bottom*) Similar to the previous scenario, position and map matches are calculated. When the specified batch length is reached, batch estimation is executed. The resulting batch estimation position and covariance are fed into the prediction step of the UKF, allowing for position correction. The corrected position is incorporated into the state vector, which is then used for the next time step.

3.2.6 Different magnetic field-aiding approaches

Different magnetic field measurements with their respective map can be used to support navigation. Since the magnetic field is a vector quantity, it offers more information than just a single scalar value such as the total magnetic field strength. Instead of relying solely on total field measurements, each vector component (e.g., in the x, y and z directions) can be considered individually. This enables the use of separate maps and corresponding measurements for each component to estimate location. The advantage is that when using only a single component, map matching identifies locations along the corresponding contour line of the map. In contrast, using multiple components results in matches that are more consistent across all components, making the identified location more probable and specific.

The effectiveness of using individual vector components $\boldsymbol{B}_x$, $\boldsymbol{B}_y$ and $\boldsymbol{B}_z$, as compared to the total magnetic field magnitude $|\boldsymbol{B}|$, is briefly evaluated in the laboratory simulation. To implement this approach, a magnetic field map for each vector component is required, against which the corresponding recorded measurements are map-matched. The resulting position estimates $\boldsymbol{x}_i$ for each axis $i \in x, y, z$ are then fused by minimizing their respective covariance matrices $\boldsymbol{P}_i$, assuming that the position estimates are uncorrelated. The fused estimates for the position $\boldsymbol{x}$ and its associated covariance $\boldsymbol{P}$ are obtained using the following equations:

$$\boldsymbol{P} = \boldsymbol{P}_x^{-1} + \boldsymbol{P}_y^{-1} + \boldsymbol{P}_z^{-1}\,, \tag{3.11}$$

$$\boldsymbol{x} = \boldsymbol{P}\left(\boldsymbol{P}_x^{-1}\boldsymbol{x}_x + \boldsymbol{P}_y^{-1}\boldsymbol{x}_y + \boldsymbol{P}_z^{-1}\boldsymbol{x}_z\right)\,. \tag{3.12}$$

Another approach would be to use the gradient components, which eliminates the need for absolute measurements. Since the gradient of a vector field is considered, this is represented as a 3×3 tensor:

$$\nabla\mathbf{B} = \begin{bmatrix} \frac{\partial B_x}{\partial x} & \frac{\partial B_x}{\partial y} & \frac{\partial B_x}{\partial z} \\ \frac{\partial B_y}{\partial x} & \frac{\partial B_y}{\partial y} & \frac{\partial B_y}{\partial z} \\ \frac{\partial B_z}{\partial x} & \frac{\partial B_z}{\partial y} & \frac{\partial B_z}{\partial z} \end{bmatrix} \tag{3.13}$$

By using the fact that the magnetic field is divergence-free as stated in Equation 2.3 and, under the assumption of that no currents and no changing electric fields are present, also curl-free $\nabla \times \boldsymbol{B} = 0$, only 5 of the 9 magnetic gradient tensor components are independent. Incorporating multiple components of these independent tensor components can enhance navigation accuracy further [42].

3.3 Simulation Approach

The simulation framework developed for this work serves two purposes. First, to test the implementation prior to conducting the real experiment, and second, to evaluate the navigation performance under controlled conditions and to identify challenges in the real world implementation of the navigation aiding algorithm. To achieve this, two different simulation scenarios have been implemented. The first scenario simulated the laboratory setup, while the second simulated a real-world application of airplane navigation using real magnetic anomaly maps.

In the following sections, both simulation approaches and the chosen parameters are described in detail.

3.3.1 Simulation of Laboratory Experiment

The lab experiment was first simulated before being deployed in the real world. This allowed the algorithm to be implemented and developed in advance.

This was achieved by simulating a randomly generated magnetic field arrangement with specified parameters, which produced the assumed true magnetic field. Based on this simulated field, magnetic field measurements were generated from the magnetometer moving along a specified circular trajectory with a set radius of $R = 0.45\mathrm{m}$ and rotational speed of $1\mathrm{RPM}$. Noise, modeled as random Gaussian noise, was added according to the specified noise characteristics of the magnetometer. In addition, the accelerations and angular velocities for the motion along the trajectory were simulated by adding expected *Gaussian* white noise. The IMU sampling rate was set to $100\mathrm{Hz}$, while the magnetometer sampling rate was set to $20\mathrm{Hz}$ during the simulations. The noisy measurements were synchronized using the same time array to allow easy traversal of the data arrays. The full set of simulation parameters can be found in the Table 3.1.

Figure 3.7 shows a randomly generated magnetic field map as a heat map in the background. The magnetic field map spans a simulated rectangle of $1.2\mathrm{m} \times 1.2\mathrm{m}$, with a chosen resolution of $1\mathrm{cm}$. Furthermore, the circular trajectory, with a radius of $R = 0.45\mathrm{m}$, is shown as a dashed blue line. The starting position of the simulation is marked by the red star. For conducting the simulation experiments, a brief parameter optimization of the UKF parameters, α and β, was first performed over the most promising interval. Following this, Monte Carlo simulations with 500 iterations per chosen batch length and map noise level were

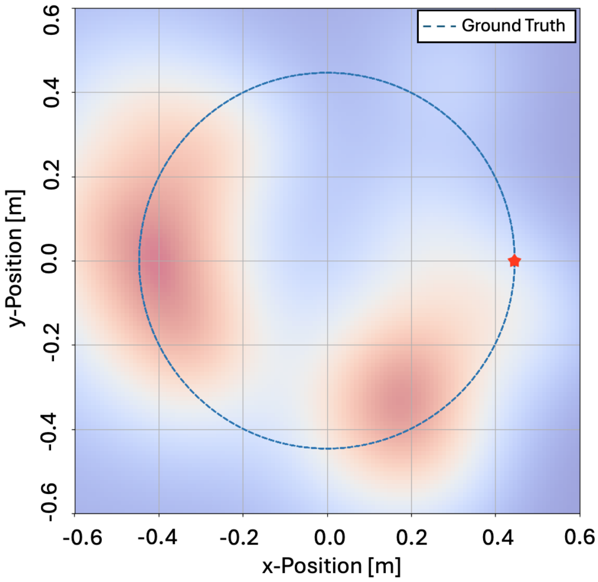

Figure 3.7: The region of interest is shown with the desired trajectory (blue, dashed line) of the moving platform on which the sensors are mounted. Also shown is the randomly generated magnetic field map with a pixel size of $1\,\mathrm{cm}$. The starting point of the trajectory is marked with a red star.

conducted. These simulations aim to analyze how map quality influences the magnetic navigation aiding algorithm and to determine the optimal batch length for the lab experiment. Furthermore, component-wise map matching using vector measurements to map the locations was also performed to evaluate how this approach affects the navigation performance.

Table 3.1: Simulation Parameters of the Laboratory Experiment

Parameter	**Units**	**Value**
Initial Position	$[\mathrm{m}]$	$(0.45 \pm 0.01, 0 \pm 0.01)$
Initial Velocity	$[\mathrm{m/s}]$	$(0 \pm 0.001, 0.047 \pm 0.001)$
Initial Heading	[deg]	0 ± 0.01
IMU Acceleration Noise Level	$[\mathrm{m/s^2/\sqrt{Hz}}]$	1×10^{-4}
Gyroscope Noise Level	[deg/$\sqrt{\mathrm{Hz}}$]	1×10^{-3}
Magnetometer Noise Level	$[\mathrm{pT/\sqrt{Hz}}]$	3
Map Noise Levels	$[\mathrm{nT}]$	$\{0.5, 1, 1.5, 2\}$
Batch Estimation Lengths		$\{10, 20, 30\}$

3.3.2 Simulation of Flight Scenarios

Building upon the simulations conducted in the laboratory, the goal was to deploy and validate the implemented navigation algorithm in potential real-world applications, such as navigation aiding for airplanes.

Similar to the laboratory simulations, the airplane's movement was restricted to the horizontal plane with stabilized roll and pitch angles. This limitation reduces the usual six Degrees-of-Freedom (DOF) in three-dimensional space to only three. This is valid because, in flight applications, further different sesnor and systems are used to determine flight height. Additionally, for determining the heading angle of an airplane, there are also further systems like magnetic heading which makes calculating of heading angle using the gyroscope redundant. By considering a constant heading angle, this reduces the DOF further to only two of the original six DOF.

The total magnetic field maps used for the simulation were derived from the Earth's Magnetic Anomaly Grid (EMAG2), which is publicly available at [30]. Since the resolution of these maps is too coarse for the intended application, they were upscaled via interpolation using a standard linear interpolation method to achieve a resolution of 2 arc-seconds, which corresponds to approximately $120\mathrm{m}$ at the chosen latitude and longitude for the simulation. Figure 3.8 shows the area of the flight path simulation. Furthermore, the position state was represented in geodetic coordinates, as the maps are referenced in the same geodetic frame also known as the North-East-Down (NED) coordinate system, resulting in a state vector of

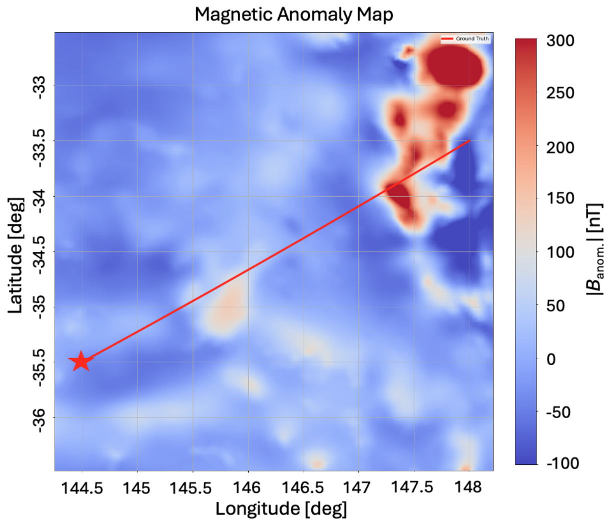

Figure 3.8: Magnetic anomaly field map of the area surrounding the implemented flight path in southeastern Australia. The actual flight path is depicted as a red line, with a star marking the starting point of the trajectory.

the following form:

$$\boldsymbol{X}_t = \left[lat_t,\, lon_t,\, v_t^{north},\, v_t^{east} \right] , \tag{3.14}$$

The magnetic field measurements were simulated by recording the magnetic field along the true flight path before starting the simulations. In addition, random *Gaussian* white noise at the specified noise level for the *QuSpin QTFM* was applied.

Since a magnetic field map typically contains errors that are unknown, additional random noise was added before performing the map matching within the rectangular search area around the INS position estimate. Only one noise level, $\sigma_{\text{map}} = 0.5\mathrm{nT}$, was chosen for the simulations. For the EMAG2 anomaly map, measurements during a real-life flight experiment would need to account for the magnetic field strength from the IGRF model, which should be subtracted from the magnetic field. An overview of the simulation parameters is provided in Table 3.2.

The simulations were conducted for two different simulation sets, each with different batch lengths and map matching rates. For both simulation sets, a parameter sweep of the UKF parameters α and β was conducted to find the optimal UKF parameter set. Once the optimal parameter set was chosen, a Monte Carlo simulation was performed for each simulation set to analyze the stability of the implemented algorithm.

Table 3.2: Simulation Parameters of the Flight Path Simulations

Parameter	**Units**	**Value**
Initial Position (lat, lon)	$[deg]$	$(-35.5 \pm \frac{2}{3600}, 144.5 \pm \frac{2}{3600})$
Initial Velocity (v^{north}, v^{east})	$[\mathrm{m/s}]$	$(18.7 \pm 0.1, 27.0 \pm 0.1)$
IMU Acceleration Noise Level	$[\mathrm{m/s^2/\sqrt{Hz}}]$	1×10^{-5}
Magnetometer Noise Level	$[\mathrm{pT/\sqrt{Hz}}]$	3
Map Noise Levels	$[\mathrm{nT}]$	0.5

3.4 Data Collection and Processing

This section outlines the process of data acquisition and storage for magnetic field-aided navigation and noise studies in the laboratory.

It begins by describing the general procedure for acquiring data, including how information from the magnetometers is retrieved and stored. Next, the method used to collect data for analyzing sensor noise and sensitivity is presented. This is followed by a brief explanation of the procedure for acquiring data to calibrate the IMU. The subsection concludes with the data collection method used to obtain sample points for generating the magnetic field map, which is essential for the navigation-aiding part of the experiment.

3.4.1 General Data Acquisition

The two magnetometers used are the *TwinLeaf VMR*, a classical magnetometer that uses three magnetoresistive sensor chips to capture the three vector components of the magnetic field, and the *QuSpin QTFM Gen2*, an optically pumped magnetometer. Both magnetometers are depicted in Figure 3.9. The specification specified by the companies are listed in Table 3.3.

To read the sensor data, two custom *Python* scripts were implemented, one for each magnetometer at hand. These scripts enable configuring the sensor settings via serial commands sent using the *UART* protocol. They also handle the reading of sensor data and storing the received data in *DataFrames*, which are subsequently saved as *.csv* files.

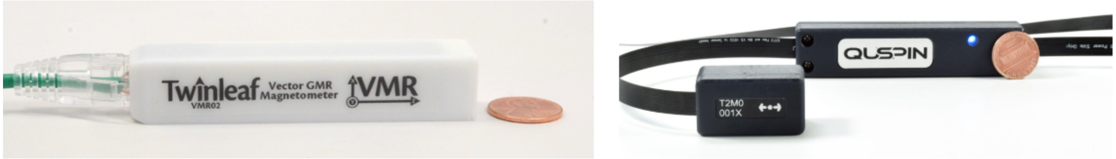

Figure 3.9: Depicted are the two magnetometers at hand: on the *left*, the *TwinLeaf VMR*; on the *right* the *QuSpin QTFM Gen2* [20].

Table 3.3: Comparison of the *TwinLeaf VMR* and *QuSpin QTFM Gen2* magnetometers.

Property	***TwinLeaf VMR***	***QuSpin QTFM Gen2***
Sensitivity $[\mathrm{pT}/\sqrt{\mathrm{Hz}}]$	300	3
Dynamic Range [μT]	$[-100, 100]$	$[1, 150]$
Max Gradient Field $[\mathrm{nT/cm}]$	N/A	300

A key component of this work is the synchronization of the two magnetometers to allow for side-by-side comparison of the magnetometers and also being able to incorporate the IMU measurements with the magnetic field measurements for navigation.
To achieve this, data from both sensors is collected at the same time using multithreading, with each measurement assigned a timestamp to ensure synchronization. This is especially critical because the two sensors send the data in different ways. The *TwinLeaf VMR* continuously streams the measurement data one by one, while the *QuSpin QTFM* sends the measurement data in batches, including internal timestamps for reconstruction of the measurement sequence.

The synchronization of the three components of the laboratory experiment is achieved through the choosing of a reference timeline. In this case, the sensor time-line of the *TwinLeaf VMR* was selected. Having this reference time line allows the other two components, the *QuSpin QTFM* and the rotation stage, to be synchronized to it.
For the sensor with the higher sampling rate, the closest sampling points are selected and aligned with the reference time-line. Given the higher sampling rate of the reference sensor, there are additional sensor readings between the matched points. These additional measurements are then utilized and incorporated into the final matched measurements by taking the mean value of the measurements that fall around the matched reading.
The same matching process, of finding the closest sampling match, is applied to the rotation stage. As the rotation stage has a lower sampling frequency, the missing sampling values are then interpolated using the closest sensor measurement. This interpolation is valid due to the fact that the rotation stage only provides positional information about the angle it is in. An illustration of this synchronization scheme is depicted in Figure 3.10.

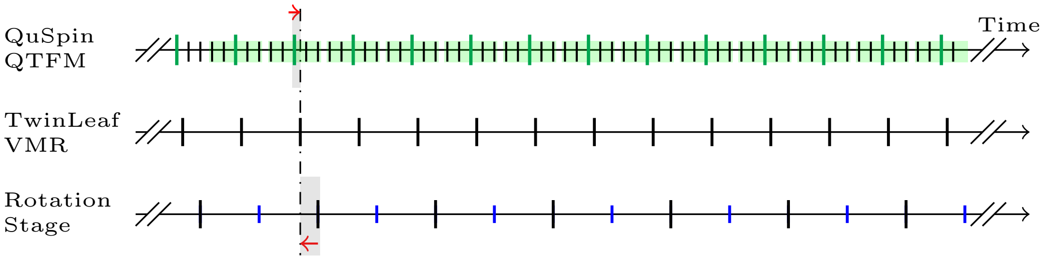

Figure 3.10: Schematic of how the data from the three sensors are synchronized for the laboratory experiment: Each sensor operates at its own sampling rate. The *TwinLeaf VMR* was chosen to provide the reference timeline. The other two sensors and their measurements are synchronized by finding the closest timestamps to this reference. For the sensor with a higher sampling rate than the reference, the excess measurements are handled by taking the mean value around the matched reading. For the lower sampling sensor, interpolation is used to estimate the missing values at the reference timestamps. This results in all three sensors sharing the same timeline and having an equal number of sampling points.

3.4.2 Noise and Drift Analysis

Prior to conducting the lab experiment, the bias, noise, and drift levels of the inertial sensors and magnetometers were quantified by acquiring sensor data over an extended period. To ensure accurate error quantification, the environment was kept as stable as possible to minimize the influence of external factors. Furthermore, the sensors had been running for several hours to reach a steady state, which in turn minimizes temperature fluctuations.

For noise and sensitivity quantification, the acquired time-series data were analyzed using a Fourier Transform to obtain the spectral density. Data from both *TwinLeaf VMR* and *QuSpin QTFM* sensors were collected simultaneously over a duration of $6\mathrm{h}$, with measurements taken overnight. This long-term data acquisition was used to analyze sensor drift via AD analysis and common linear drift fitting.

3.4.3 Inertial Sensor Calibration

Accurate position estimates calculated from inertial sensors depend on precise calibration, especially ofr consumer grade IMU. Sensor bias can significantly distort the calculated position, leading to large errors in a short period of time. This is particularly problematic for the navigation-aiding algorithm in the laboratory experiment, which may not have enough time to counteract excessive drift.

The basic method for calibrating the IMU sensors is *static calibration*. This method is using known output values of the sensor for different orientations to estimate the offsets caused by *axis misalignment*, *non-orthogonality*, and *gravitation*. To correct for these systematic errors, a *calibration matrix* $\mathbf{A}$ can be used, which accounts for misalignment and scale factor deviations, while individual sensor biases are captured in a bias vector $\mathbf{b}$. The calibrated sensor output (x_i, y_i, z_i) is then computed as:

$$\begin{bmatrix} x_i \\ y_i \\ z_i \end{bmatrix} = \begin{bmatrix} a_{11} & a_{12} & a_{13} \\ a_{21} & a_{22} & a_{23} \\ a_{31} & a_{32} & a_{33} \end{bmatrix} \begin{bmatrix} g_{ix} \\ g_{iy} \\ g_{iz} \end{bmatrix} + \begin{bmatrix} b_x \\ b_y \\ b_z \end{bmatrix} .$$

(g_{ix}, g_{iy}, g_{iz}) is the expected output for each axis. In the case of aligning the the z-axis of the sensor parallel to the gravity vector it should read $\left(0\frac{m}{s^2}, 0\frac{m}{s^2}, 9.81\frac{m}{s^2}\right)$. By recording the output of each axis for various orientations and and knowing the expected output value each orientation should have, it is possible to solve for matrix $\mathbf{A}$ and vector $\mathbf{b}$. For calibrating the built-in IMU of the *TwinLeaf VMR*, six static orientations were used with each axis aligned parallel and antiparallel once to the gravity vector. This calibration step has to be only done once.

Furthermore, as the IMU is mounted on a moving platform, perfect horizontal alignment is not always possible. As a result, further calibration is required to obtain accurate measurements. After each standstill simulation, a short measurement is taken to remove static bias caused by a slight tilt of the platform, thus eliminating gravitational offsets.

3.4.4 Magnetic Field Map Generation

The quality and accuracy of the magnetic field map are crucial for navigation with magnetic fields. For navigation to be reliable, the map must provide accurate, location-specific magnetic field data. This section outlines the two main steps involved in producing these maps. The first step focuses on the data collection methods, while the second step outlines the process of transforming the measured data into a usable map.

The laboratory experiment uses a rotating platform, therefore the same platform was used to generate the underlying magnetic field map. By varying the radius of motion, the main Region of Interest (ROI) of the $1.5\mathrm{m} \times 1.5\mathrm{m}$ area can be traversed sufficiently. Given the

dimensions of the OPM sensor head, a pixel resolution of $2\mathrm{cm}$ was selected for the preliminary measurement mapping.
However, to avoid the need to measure at 30 different radii, data were collected at only eight radii, ranging from $30\mathrm{cm}$ to $75\mathrm{cm}$ with $5\mathrm{cm}$ separation.
Data collection for map generation was performed by synchronizing the *QuSpin QTFM Gen-2* magnetometer with the step readings of the rotary stage. Each sensor reading was given an absolute timestamp, which was then used to determine the location of each magnetic measurement. The magnetometer was configured to sample at a rate of $128\mathrm{Hz}$, while the rotary stage provided position readings at approximately $20\mathrm{Hz}$. To synchronize the data sets, the magnetometer readings with the smallest time stamp difference to each stage reading were selected. As the magnetometer provided excess readings, these were averaged to minimize uncorrelated random noise, which acts further as a low-pass filter. In addition, due to the chosen velocity of $1\mathrm{RPM}$, several averaged magnetic field measurements fell within the $1\mathrm{cm}$ pixel size, requiring further averaging to ensure spatial consistency.

To compensate for the missing grid points, a *Kriging* interpolation algorithm was implemented, which allowed the reconstruction of the complete magnetic field map. As different *Kriging* interpolation algorithms exist and parameters such as sill and range can be adjusted depending on the underlying problem, the experimental variogram of the recorded maps were used to find the best matching method and the best parameter set.

The resulting map is complete, with no missing pixels within the circular ROI of radius $R \in [0.3\mathrm{m}, 0.75\mathrm{m}]$.

4 Results & Discussion

This section presents the results obtained from both the simulation approaches and the experiment conducted in the laboratory. Additionally, the results are discussed to provide a clearer understanding of the rationale behind each step taken.

In the first part, the results of the simulation approaches are presented and discussed, including both the laboratory experiments and the flight path simulation results.
Moving on from the simulation approaches, the experimental data are presented and discussed in the second half of this chapter. This includes further a comparison of the magnetometers at hand in terms of drift and noise.

4.1 Simulation Approach

4.1.1 Simulation of the Laboratory Experiment

This section presents the results of the simulation of the laboratory experiment. The map is introduced, and its characteristics are outlined. The optimization results of the sampling parameters α and β for the UKF are then discussed. With the optimized parameters, the algorithm is evaluated in terms of performance and stability, considering the batch length and map noise. In addition, magnetic field navigation using the vector components of the magnetic field for navigation is also examined.

Simulated Magnetic Field Map

The randomly generated simulated magnetic field map used for the subsequent analysis is shown in Figure 4.1 (*upper left corner*). Additionally, the variability of the map within the search area of each pixel is calculated using the equation presented in Equation 3.9. For this calculation, a pixel radius of $r_s = 3$ was chosen, and the entire map was traversed pixel by pixel. The map varies between $2\mathrm{nT}$ and $50\mathrm{nT}$.

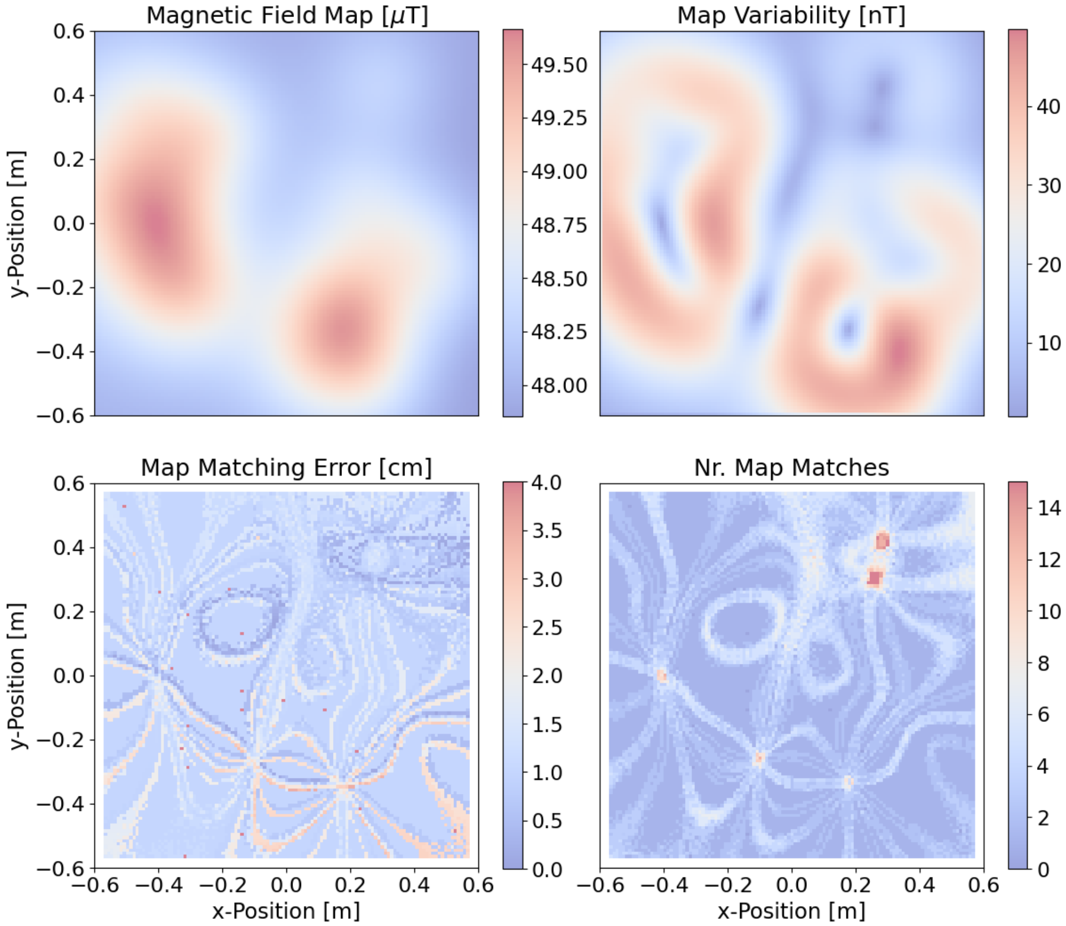

Figure 4.1: (*Upper left*) Randomly generated magnetic field map used in the following section. (*Upper right*) Corresponding map variability, calculated using Equation 3.9. (*Bottom left*) Mean map matching error per pixel, computed using the PDA implemented in the navigation aiding algorithm. (*Bottom right*) Mean number of map matches within the search area of each location in the map.

Further evaluation of the position estimate error within the considered search area for each pixel, using the PDA approach presented in Section 3.2.2, is shown in Figure 4.1 (*bottom left*). The corresponding number of map matches found in the search area is depicted in Figure 4.1 (*bottom right*). For these evaluations, randomly generated magnetic measurements, incorporating the magnetometer noise of the *QuSpin QTFM*, were conducted for each pixel. The resulting plots represent the mean values of ten computations.

The map matching error is generally around $1\mathrm{cm}$, which corresponds to the spatial resolution of the map. The results of the map matching evaluation reveal interesting patterns, with line contours indicating deviations in the mean PDA error. Further analysis of the number of map matches shows similar patterns, suggesting that in those regions of the map, more matches are found and incorporated into the position estimate. This indicates a correlation where a higher number of map matches leads, in some cases, to a higher position error and, in others, to a lower position error.

Discussion: One realization of the magnetic field map arrangement was presented, along with an analysis of how the map varies and how the map matching algorithm performs across the entire area. This included the evaluation of map variability and the PDA error over the full map. For this analysis, a defined search area around each pixel was considered, with a constant radius. The radius was selected based on the observation that the standard deviation σ_x of the position estimate tends to converge at a value slightly above the pixel resolution. As specified, a search radius of $r_s = 3\mathrm{px}$ was used in this evaluation, as this was found to be the mean search radius when setting it to three times the standard deviation of the state's position estimate $r_s = 3\sigma_x$ when navigation simulations were conducted. Since the number of matches across most of the map remains below five, and the PDA position error stays close to the pixel resolution, this indicates that the bounds for map matching are appropriately defined. These measurement bounds were set according to the specifications detailed in Section 3.2.1.

Optimization of Unscented Kalman Filter Parameter

In order to find the optimal set of UKF parameters, a parameter sweep of the scaling parameters α and β of the UT was conducted. For the optimization, a batch length of ten was used. Additionally, the map noise in the simulations was set to a level of $\sigma_{\text{Map}} = 1\mathrm{nT}$. The intervals for parameter α were set to $[0.1, 0.9]$ and for β to $[2, 8]$, with respective step sizes of $\Delta\alpha = 0.1$ and $\Delta\beta = 1$. For each parameter combination, a total of 10 simulations were conducted.

The resulting mean of the mean absolute error (*MAE*) of the magnetic field-aided navigation algorithm for different values of α and β is presented in Figure 4.2 (*left*). Furthermore, Figure 4.2 (*right*) shows the mean simulation duration achieved for each parameter set. The parameter optimization plots do not show any clear tendency or relationship between the α and β parameters of the UKF. However, some parameter sets exhibit a lower MAE and a higher mean simulation duration.

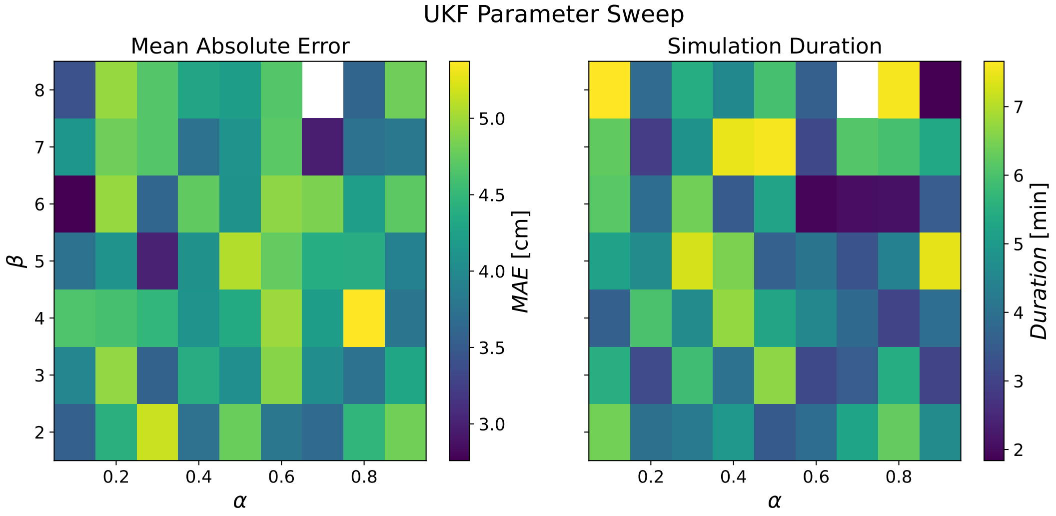

Figure 4.2: (*Left*) Mean of mean absolute error of the navigation aiding algorithm for each set of α and β. (*Right*) Mean of simulation duration of each parameter set. Simulation duration is considers the simulated time in which the position error of the magnetic field-aided navigation does not exceed $15\mathrm{cm}$.

To select the optimal parameter set, a cost function was defined, which minimizes the MAE of the simulation runs while maximizing the duration of simulations. The following cost function was formulated:

$$J(\alpha, \beta) = w_1 \cdot \text{MAE}(\alpha, \beta) - w_2 \cdot \text{Duration}(\alpha, \beta) \tag{4.1}$$

The three best parameter sets that minimize the cost function, along with their corresponding MAE values and simulation durations, are presented in Table 4.1. Parameter Set 1 was selected for further analysis of the algorithm's stability in the following course of the work.

Table 4.1: Optimal Parameter Sets for UKF

Parameter Set	α	β	*MAE* $[\mathrm{cm}]$	*Duration* $[\mathrm{min}]$
Set 1	0.3	5	3.0	7.3
Set 2	0.3	6	2.8	6.2
Set 3	0.1	8	3.4	7.7

Discussion: Prior to conducting the parameter optimization step, it was observed that the UKF parameters significantly influence the algorithm's performance. This initial optimization, although based on a limited number of samples, aimed to identify general trends in how performance depends on the chosen parameters. However, for a more reliable and robust analysis, a larger number of samples per parameter set would be necessary. Additionally, a wider range for the scaling factor α should be considered, as suggested in the [33], where it is stated that α could be varied within the interval $[1 \cdot 10^{-4}, 1]$. The limitations of the implemented optimization presented were mostly due to the number of samples, the computational time, and the large number of simulations required. To manage this, a simulation stop was implemented at a duration of $20\mathrm{min}$, as simulations reaching this point typically required around $5\mathrm{min}$ of computation time.

This optimization process is closely tied to the estimation of map-matching covariances. Defining these covariances is not straightforward, and the parameter tuning can also be interpreted as a way of fine-tuning how the assumed Gaussian PDF are sampled and fused. Therefore, the optimization plays an important role in both enhancing performance and refining the underlying probabilistic assumptions used for the fusion of the position estimates. Furthermore, it is important to note that the UKF used for fusing the position estimate of the batch estimation with the INS position estimate, and the UKF used to fuse single matches for batch estimation, currently share the same parameter set of α and β. While separating these UKF parameter sets could be beneficial, as this would allow for further tuning, it would also require two separate optimization processes if optimal performance is desired.

Navigation Algorithm Stability Analysis

The evaluation of the implemented navigation algorithm was conducted using Monte Carlo simulations. A total of 500 simulations were performed for each batch length and map noise level considered. The results are shown in Figure 4.3 and Figure 4.4.

As in the previous UKF optimization, two observables are evaluated. The duration of the simulations in which the magnetic field-aided navigation did not exceed the defined error threshold of $15\mathrm{cm}$, and the MAE over the entire simulated trajectory are looked into. Focusing on the distribution of simulation durations dependent on map noise and batch length, it can be observed that, although the optimization step was performed at a batch length of 10, the peaks of the PDF for batch lengths of 20 and 30 tend to occur at slightly higher durations for map noise levels above $1\mathrm{nT}$. Additionally, the number of simulations reaching the maximum duration of $20\mathrm{min}$ decreases significantly as the map noise increases. For example, at a batch length of 20, the proportion of simulations reaching the maximum duration drops

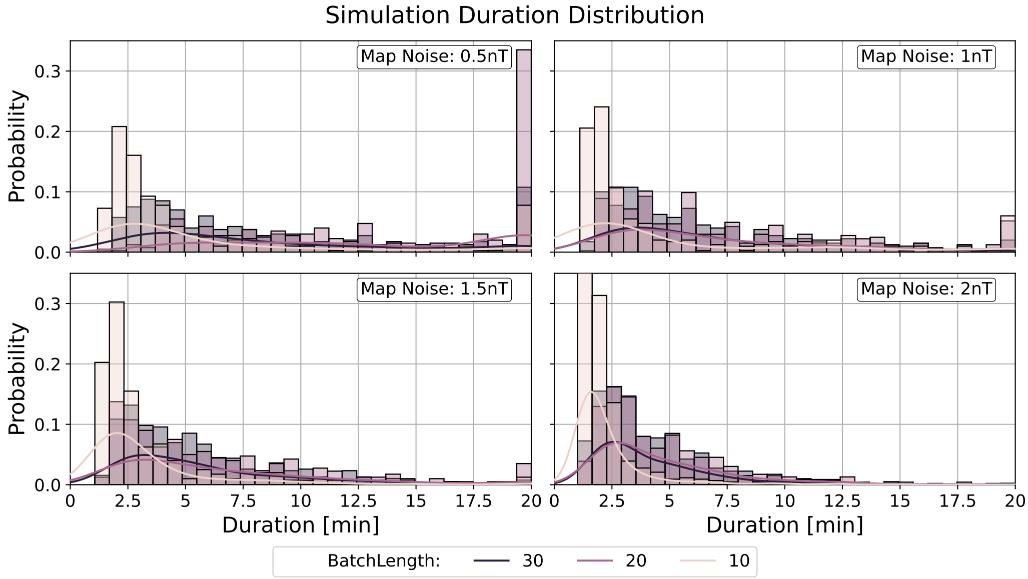

Figure 4.3: Histograms of simulation durations for different batch lengths and map noise levels.

from approximately 33% at a map noise level of $0.5\mathrm{nT}$ to around 6% with at map noise levels $1\mathrm{nT}$. With further increases in map noise, this percentage continues to drop, reaching below 1% for map noise level of $2\mathrm{nT}$. This trend is consistently observed across all batch lengths.

When examining the distribution of the MAE, particularly at low map noise levels, distinct peaks are observed for noise levels of $0.5\mathrm{nT}$ and $1\mathrm{nT}$, with the mean absolute error centered below $2\mathrm{cm}$. At higher map noise levels, these peaks become less pronounced as the PDF broadens and shifts slightly upward, indicating an increased position error. Additionally, it is visible that a batch length of 10 results in poorer performance compared to longer batch lengths. A few simulation examples with varying simulation durations are shown in the Appendix. To evaluate the deviation of the navigation-aided position estimate over time and compare it to the position estimate from pure INS navigation, simulations that reached the end of the simulation time without exceeding the set error threshold were considered. The graph in Figure 4.5 (*left*) shows the resulting error plots over time for the navigation-aided algorithm and the pure INS at map noise level of $1.5\mathrm{nT}$ and batch length of 20. For this, the mean of the simulation considered is taken. The pure INS position errors diverge fast ending the $20\mathrm{min}$ simulation duration at about $1-2\mathrm{m}$, while the position error of the map matching algorithm stays bounded within $0.5-4\mathrm{cm}$. This is visualized in the zoomed in

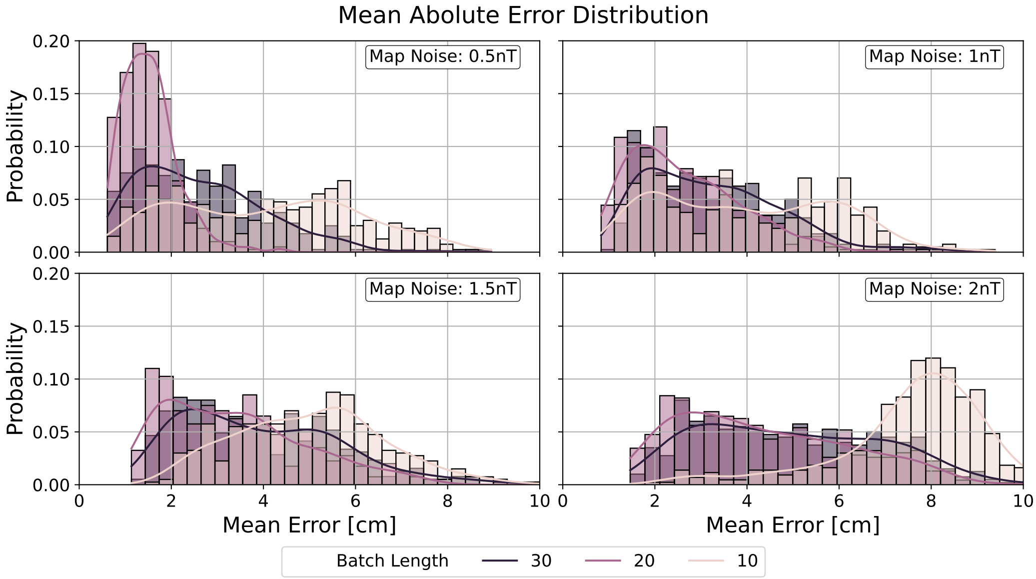

Figure 4.4: Histograms of mean absolute errors for different batch lengths and map noise levels.

interval in Figure 4.5 (*right*). It is noticeable that oscillation in the position error are present. This is attributed to the circular trajectory of the movement and the fact that the body moves multiple times through the same map.

Discussion: The simulation of the laboratory setup was carried out using a single randomly generated magnetic field map realization. This was done to evaluate the performance and stability of the implemented algorithm, specifically in relation to map noise level and batch length, while keeping the map constant. Further studies could explore different parameter sets, as many of the algorithm's parameters are adjustable. For example, the dependency of the search radius on the position estimate, as well as the bounds for considering a map match, could be varied. The algorithm demonstrated good navigation performance, as most of the trials were successfully completed over one entire circular trajectory. Divergence issues seem to arise when map matches were missing or incorrect matches are used, particularly when velocity errors especially the direction component are present. As this leads to high deviation from the true location while no position correction is done.

One key research point that needs to be addressed is the potential for correcting velocity drift when only fusing INS and magnetic field measurements. It is important to note that this simulation was specifically tailored to the planned laboratory experiment. For other appli-

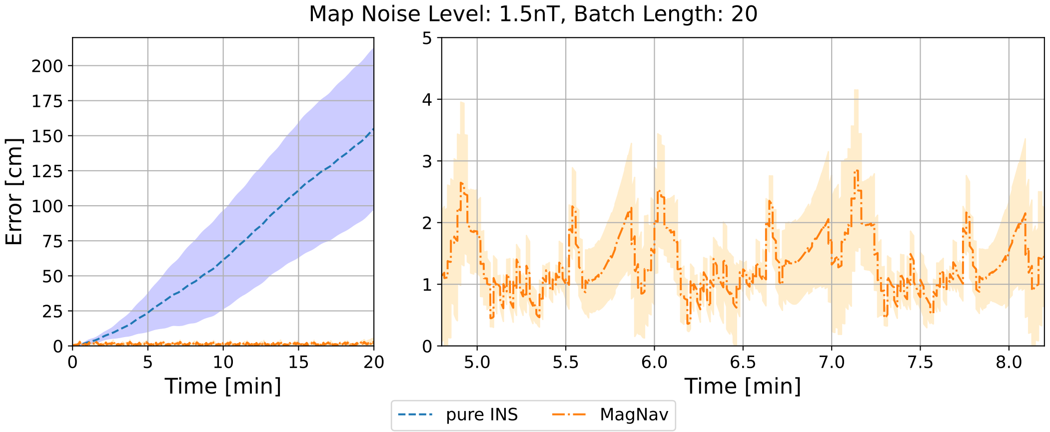

Figure 4.5: The mean error over time of the considered simulations that reached the simulation end is depicted. A comparison between the navigation-aided algorithm and the pure INS error shows that the algorithm's error does not diverge and remains bounded, which is not the case for the unaided error.

cations, different simulations would be required, but the methodology used to analyze the stability of the algorithm's performance could be adapted accordingly. Further simulations should consider a wider range of scenarios.

Navigation Aiding Based on Vector Components of the Magnetic Field

The previous simulation only considered the total intensity of the magnetic field. However, since the magnetic field is a vector field, the vector components of the field can also be utilized for navigation aiding. Equivalent to the previously presented Monte Carlo simulations, a Monte Carlo simulation is conducted that considers fusing position estimates of each of the three vector components for navigation aiding. To compare the performance of the total intensity map matching with that of the vector component matching, the simulations were limited to a single batch length of 20 and a map noise level of $1.5\mathrm{nT}$. The resulting MAE and simulation duration histograms of the Monte Carlo simulations are presented in Figure 4.6. When comparing these vectorial navigation results (blue) to the previously presented Monte Carlo simulations (solid black line), it becomes evident that utilizing all three vector components for map matching enhances the simulation duration. The peak of the empirical PDF occurs around $4\mathrm{min}$, compared to the peaks at around $3\mathrm{min}$ in the previous simulations. However, the comparison indicates the histogram indicates that more simulations reach the maximum simulation duration of $20\mathrm{min}$. Looking at the mean absolute error distribution,

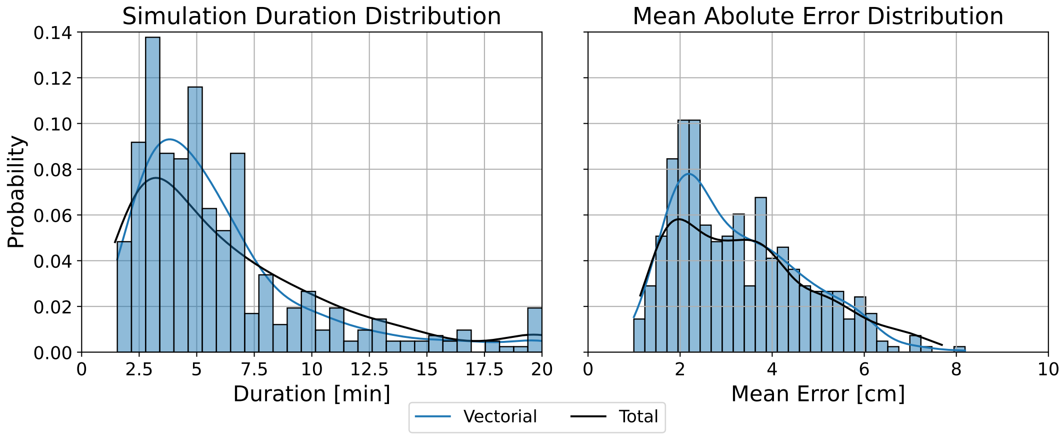

Figure 4.6: Monte Carlo results using all three vector components of the magnetic field for map matching. Simulation parameters are set to a batch length of 20 and a map noise level equivalent to $1.5\mathrm{nT}$ for total intensity map matching.

the peak of the distribution is more prominent compared to the corresponding total intensity map matching. When comparing this to the other map noise level distributions of the total intensity map matching, it is evident that although a map noise level of equivalent $1.5\mathrm{nT}$ was simulated for these vector component simulations, the resulting distribution more closely resembles those for lower map noises of the total intensity simulations. This suggests that using all three vector components results in more robust navigation aiding.

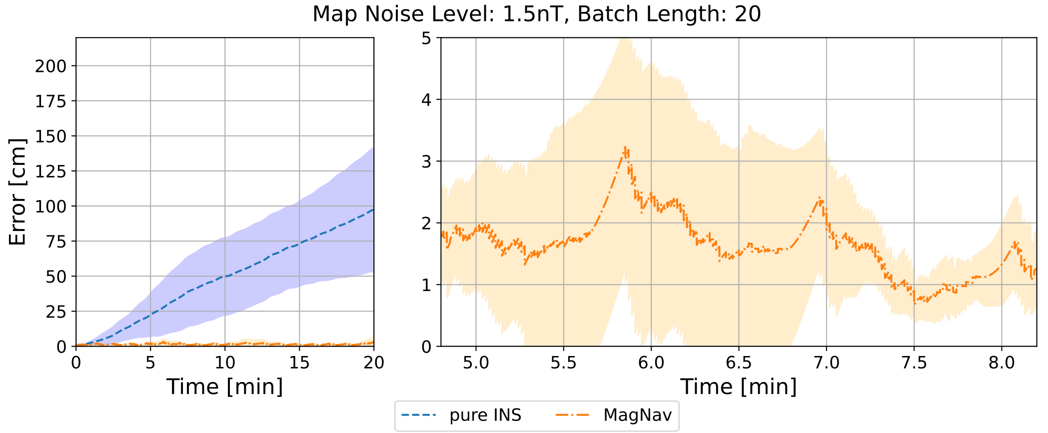

Figure 4.7: The mean error over time of the considered simulations that reached the simulation end using the three vector components for map matching is shown.

Figure 4.7 shows further the mean error with the respective standard deviation over time for simulations that reached the end of the simulation. Comparing this error plot to the total magnetic field one it can be seen that the error curve has a different reoccuring pattern and less error fluctuations within one rotation.

4.1.2 Flight Path Simulations

Simulations were conducted using the specified flight path and a real magnetic anomaly map, both of which were introduced in the previous chapter. Two different sets of parameters were selected. *Simulation Case A* uses a batch length of 10 with the magnetometer sampling rate set to $0.2\mathrm{Hz}$. *Simulation Case B* uses a batch length of 25 and a magnetometer sampling rate at $1\mathrm{Hz}$. For both sets, a brief UKF parameter optimization was performed prior to conducting the Monte Carlo simulation with the optimal parameter sets found.

Optimization of Unscented Kalman Filter Parameter

Initially, a quick optimization of the UKF parameters for each simulation set was performed using a limited number of simulation samples of 10. The parameters α and β were considered within the ranges $\alpha \in [0.3, 0.5]$ and $\beta \in [4, 8]$. The intervals for α and β were not equally spaced and the intervals chosen based on intuition of prior simulations. The resulting heat plots of the *Mean Absolute Error (MAE)* and *Total Error (TE)* for Simulation Case A are shown in Figure 4.8. The same heat plots for Simulation Case B can be found in the Appendix. Neither of the plots for both simulation cases do show any clear tendency on how UKF parameter influence the performance of the navigation aiding. However, some parameter sets tend to perform better than others. To determine the optimal parameter set, the following cost function was defined to minimize both the *MAE* and *TE* simultaneously:

$$J(\alpha, \beta) = w_1 \cdot MAE(\alpha, \beta) + w_2 \cdot TE(\alpha, \beta)\,, \tag{4.2}$$

where the weights are set to $w_1 = w_2 = 0.5$. The top three parameter sets for α and β identified during the minimization process for each Simulation Case are presented in Table 4.2.

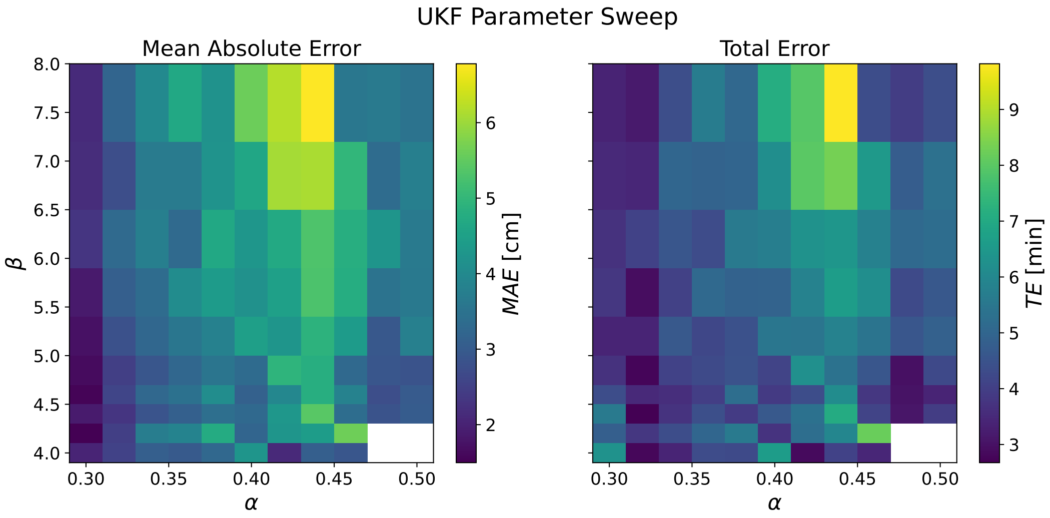

Figure 4.8: Resulting mean values for the *Mean Absolute Error* and *Total Error* for each UKF parameter set of Simulation Case A.

Table 4.2: Optimal Parameter Sets for UKF

	Parameter Set	α	β	*MAE* $[\mathrm{km}]$	*TE* $[\mathrm{km}]$
Group A	**Set 1**	0.42	4	2.09	2.85
	Set 2	0.32	4.4	2.32	2.68
	Set 3	0.3	5.2	1.74	3.38
Group B	**Set 1**	0.58	9	1.29	4.23
	Set 2	0.5	8	1.32	4.49
	Set 3	0.3	8	1.41	4.69

Furthermore, Figure 4.9 illustrates the mean error plots for various UKF parameter sets used in the implemented navigation algorithm during the optimization step for Simulation Case A. For this analysis, the error from each individual simulation was calculated, and the mean error was then computed for each parameter set. It is evident that the choice of parameters has a significant impact on the resulting navigation error curves. Most simulations show a rapid divergence from the true trajectory. However, some simulations stabilize at different error magnitudes after the initial divergence, while others show a diverging pattern similar to that of the pure INS. The error plot corresponding to the optimal parameter set is highlighted in green, with the shaded area representing the $\pm 1\sigma$ confidence interval. The respective error plots for the parameter sets of Simulation Case B are provided in the Appendix.

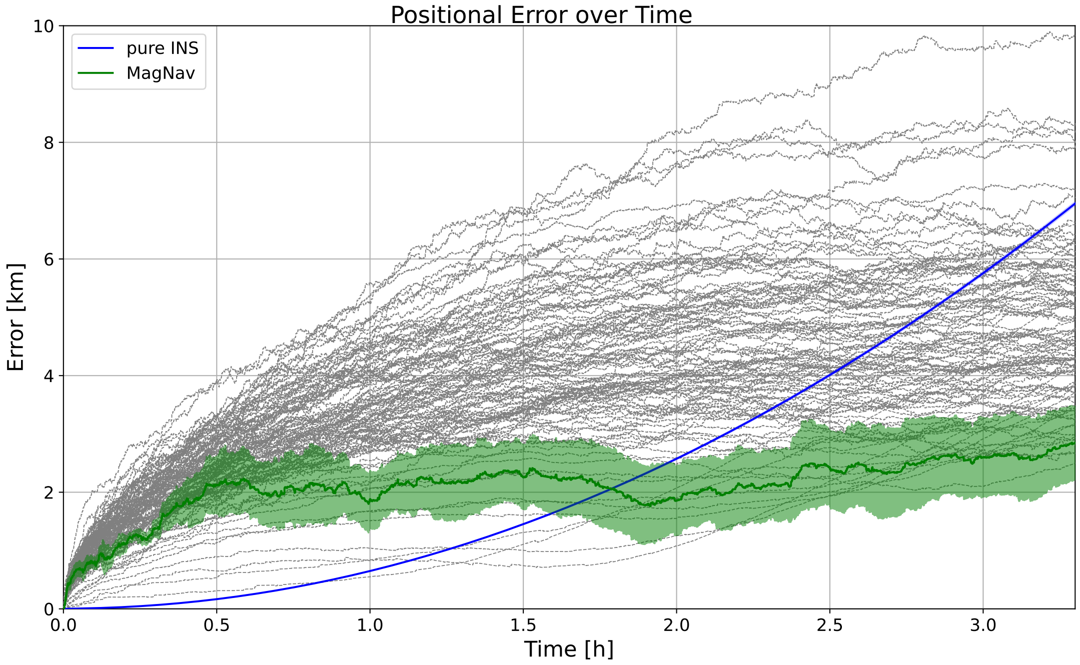

Figure 4.9: Mean errors along the trajectory for different parameter sets of α and β. The error plots show varying curves depending on the parameter values, indicating that the UKF parameters have a significant impact on the navigation performance of the algorithm.

Discussion: Similar to the optimization performed in the laboratory experiment, a brief parameter optimization was conducted for both simulation cases considered. As before, only a limited sample size of 10 simulations per parameter set was used. The results indicate that different parameter configurations lead to varying navigation performance.

For the optimal parameter set in Simulation Case A, the position error initially increases rapidly, reaching approximately $2000\mathrm{m}$, which is even higher than that of the pure INS. However, the error appears to stabilize over time, suggesting that the navigation error is ultimately bounded. In contrast, the best parameter set for Simulation Case B shows a slower initial error growth. Yet, as the trajectory progresses, the position error curve begins to follow a similar diverging trend to that of the pure INS solution. In the case of the optimal parameter set of Simulation Case A the algorithm seems to be overconfident during the initial phase, leading to a rapid divergence from the true position. Wile for the Simulation Case B the algorithm seems to lack sufficient correction, which results in an error curve that closely resembles pure INS performance.

This optimization was conducted using two different simulation cases, each employing varying batch lengths and sampling rates. However, certain parameters such as the spatial and measurement bounds used for map matching were kept fixed across both cases. Further simulations and a broader exploration of the full parameter space are necessary to improve the performance of the navigation algorithm. The current parameters were selected based on intuition and insights gained during the development and tuning of the simulation code.

It is important to note that the conclusions drawn here are limited by the small number of simulations per parameter set. To overcome this in the following section a Monte Carlo simulation using the most promising parameter set for Simulation Case A and Simulation Case B is conducted.

Monte Carlo Simulations

With the optimal parameter set for α and β for each simulation case chosen, a Monte Carlo study was conducted to further evaluate the algorithm's performance. In this study, 1000 simulation runs were performed for each case.

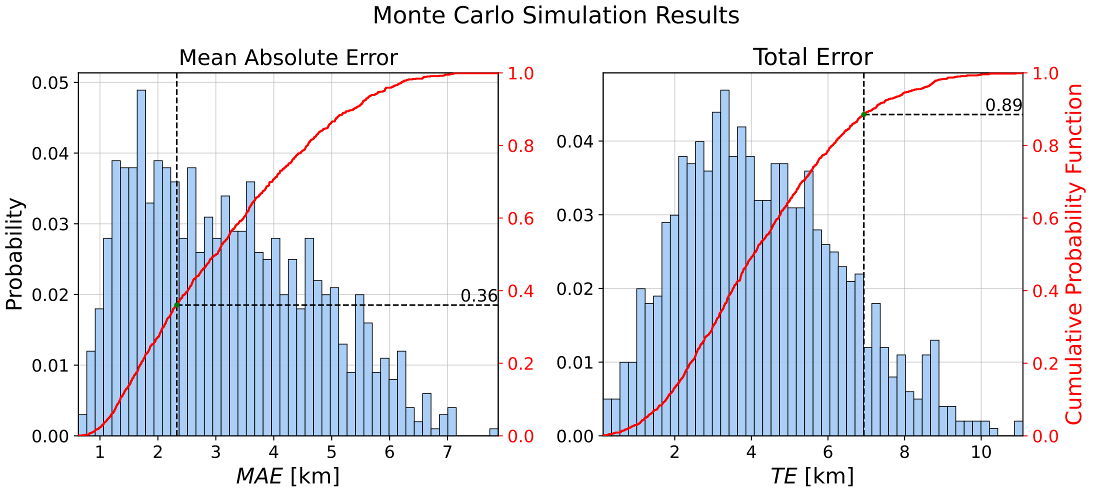

Figure 4.10: Histograms and the respective cumulative probability function from the conducted Monte Carlo simulations: (*Left*) Mean Absolute Error between the true trajectory and the navigation-aided trajectory. (*Right*) Total Position Error at the end of the navigation.

The resulting histograms for the *MAE* and *TE* for Simulation Case A are shown in Figure 4.10. Further, along with the histograms, the cumulative probability functions are depicted. This allows for determining the percentage of simulations that outperformed the pure INS navigation. Looking at the distributions in the histograms, the peak values of both measures, the *MAE* and the *TE*, are smaller than the average INS error across the simulations. Looking at the cumulative probability function of the *TE*, it is visible that around 89% of the simulations stay below the value of the pure INS estimate. The cumulative probability function of the *MAE* shows that only about 39% of the aided navigation runs outperform the pure INS in terms of position error along the trajectory. This leads to the conclusion that, even though the final position estimate of the aided navigation is more accurate for most of the simulations, the overall navigation performance along the trajectory of the majority of simulations is worse. This is also reflected in the mean error plots along the trajectory, which are accumulated and averaged over different *MAE* values, which are depicted in Figure 4.11 with different colors. Further, Table 4.3 lists the corresponding probabilities of the selected *MAE* intervals. However, looking at the error plot of the best simulation with the lowest *MAE*

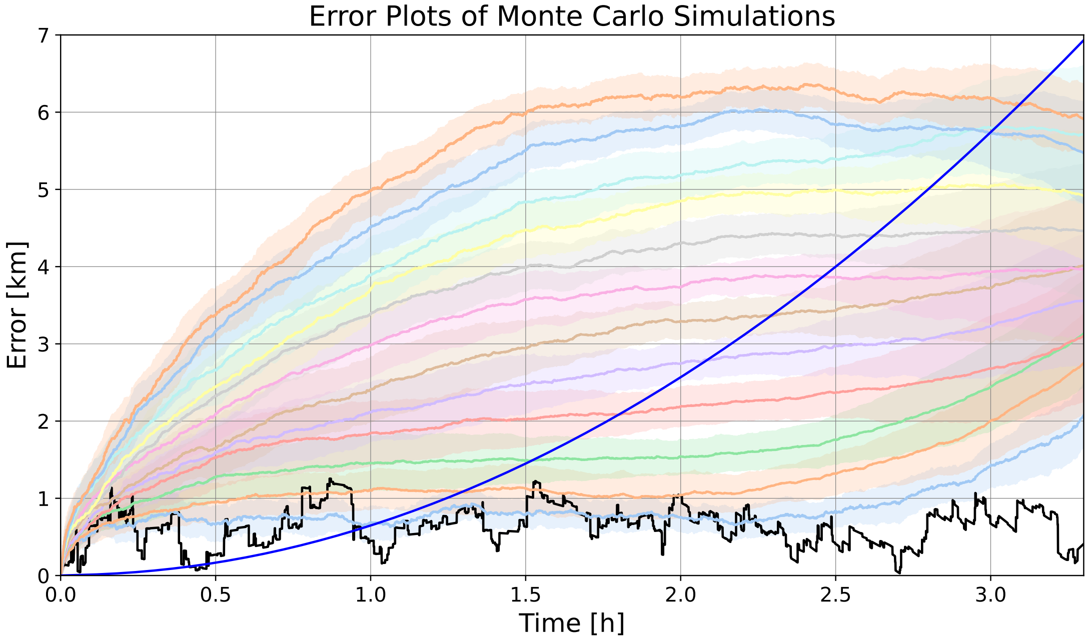

Figure 4.11: Resulting error plots from the Monte Carlo simulations. *Dark blue solid line*: Diverging error curve of the pure INS position estimate. *Colored solid lines with shaded areas*: Mean and standard deviation of simulations that fall within specified MAE intervals. *Black solid line*: Error plot of the best simulation from the Monte Carlo runs.

value (solid black line), it is visible that position error can be bound within maximal position error of $1.2\mathrm{km}$.

Table 4.3: Probability over the plotted *MAE* $[\mathrm{km}]$ intervals.

$p(0.6 < MAE < 1.0)$ = 2.3%	$p(3.0 < MAE < 3.4)$ = 8.9%
$p(1.0 < MAE < 1.4)$ = 9.1%	$p(3.4 < MAE < 3.8)$ = 8.2%
$p(1.4 < MAE < 1.8)$ = 11.3%	$p(3.8 < MAE < 4.2)$ = 7.0%
$p(1.8 < MAE < 2.2)$ = 10.8%	$p(4.2 < MAE < 4.6)$ = 6.6%
$p(2.2 < MAE < 2.6)$ = 9.6%	$p(4.6 < MAE < 5.0)$ = 5.9%
$p(2.6 < MAE < 3.0)$ = 7.4%	$p(5.0 < MAE < 5.4)$ = 3.8%

Discussion: The results of the Monte Carlo simulations using the optimized parameter set from the previous section have been presented. The simulation revealed mixed navigation performance, with both well-performing and poorly-performing runs. When comparing the MAE of pure INS navigation to that of magnetic field-aided navigation, it is evident that in most cases, the aided navigation performs worse overall. This is in contrast to the optimization step, where the aiding algorithm appeared capable of bounding the position estimate. This leads to the conclusion that further optimization will require a larger number of simulations, as previously mentioned. Nevertheless, the best outcomes demonstrate that position correction is possible.

This leads to the conclusion that further work on the algorithm and the covariance estimation is necessary, or alternatively, that additional optimization of the UKF parameters and other variables, such as batch length, search radius, and measurement bounds, is required. When comparing the results to similar simulations by Wang *et al.* (2023) [10], it becomes evident that their algorithm, which also uses a magnetic anomaly map in a similar region of Australia, performs better. Although the overall scheme of map matching and the PDA approach in this work is based on their methodology, a similar level of navigation performance could not be replicated. However, it is unclear in their work whether the magnetic field map also accounts for additional noise. In this simulation, *Gaussian* white noise was added to the map to model environmental noise. This was done following the work of Canciani [28], who notes that map errors must be taken into account, as they can arise from both the recording process and map interpolation, which can be as high as $2\mathrm{nT}$. A noise level of $0.5\mathrm{nT}$ was chosen here based on the mentioned maximal expected deviations.

Further, noteworthy is that the algorithm by Wang *et al.* [10] implements smoothing and refines the position estimate by incorporating both forward and backward filtering, while iterating multiple times along the whole trajectory to improve the navigation accuracy.

4.2 Experimental Laboratory Data

This section presents the experimental results recorded in the laboratory. The evaluation begins with the IMU and magnetometer drift and noise analysis, followed by an analysis of the recorded magnetic field maps and their stability over time. The section concludes with the presentation of the magnetic navigation attempts conducted within the laboratory.

4.2.1 Noise and Drift Analysis

IMU Performance Quantification

For the characterization and quantification of the IMU noise processes, an overview of the time series recorded for each sensor type (accelerometer and gyroscope) is presented. This overview includes the *PSD plot*, the *AD plot*, the raw data with a linear regression, and the low-pass filtered raw data (averaged over $10\mathrm{s}$) along with the the respective linear regression.

The overview of the accelerometer data is shown in Figure 4.12. By examining the AD plot, it is evident that all three accelerometer contain *Gaussian* white noise, as indicated by a slope of $m = -0.5$ in the region of $\tau \in [0.1, 1]$ in the AD graph. Additionally, the accelerometers exhibit correlated noise, visible as slight humps in the AD graph for $\tau < 3 \times 10^3$ between the downsloping section and the minimum region, which distorts the Bias Instability (BI) quantification. The minimum region quantifies the BI for all three axes within the range of $\tau \in [2 \cdot 10^3, 9 \cdot 10^3]$. Moreover, the acceleration random walk process dominates the noise for $\tau > 3 \times 10^4\mathrm{s}$, as the *rate random walk* and *drift rate random walk* σ_{AD} increase rapidly. By evaluating the value at $\tau = 1\mathrm{s}$ of the linear fitted line (dashed), the corresponding *Velocity Random Walk (VRW)* value can be determined. The BI, which quantifies random variations in sensor bias over shorter time intervals, is identified in the region with a slope of $m = 0$, within the interval $\tau \in [10^1\mathrm{s}, 10^3\mathrm{s}]$, where the Allan deviation curve reaches its minimum. Furthermore, since the AD plots does not shows an upward slope with $m = 1$ for longer integration times τ, no drift rate can be quantified from the data. The computed values are listed in Table 4.4. Additionally, the sensor drifts, as indicated by the slopes of the linear regressions of the measurement series, are found in the same Table. Similarly, the same analysis can be done for the gyroscopes of the IMU. Figure 4.13 shows an overview of the gyroscope measurements. Additionally, *Gaussian* white noise is present in the sensor measurements of all three axes. Furthermore, the x and y-axes show correlated noise, visible as slight humps before the minimum region is reached. The minima are reached at slightly

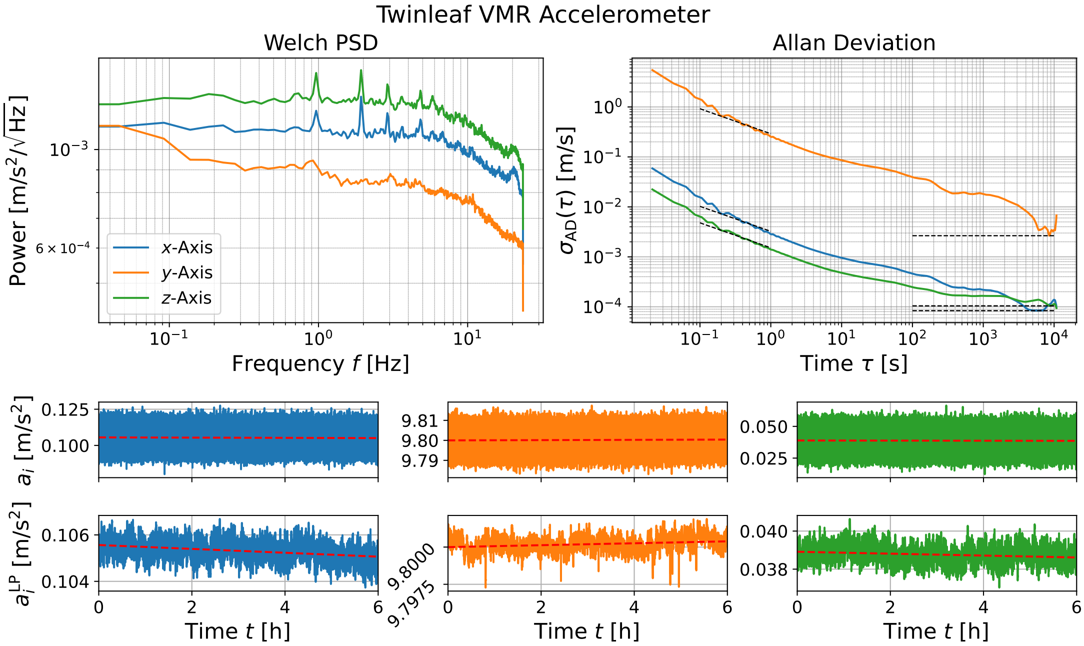

Figure 4.12: Accelerometer Noise and Drift Overview: (*Upper row, left*) Power Spectral Density. (*Upper row, right*) Allan Deviation. (*Middle row*) Raw time series data of the accelerometer recordings, including a linear fit for each axis. (*Bottom row*) Low-pass filter applied to the raw data of each axis, including the same linear fit.

smaller τ values, within the interval $\tau \in [7 \cdot 10^2\mathrm{s}, 4 \cdot 10^3\mathrm{s}]$. Again, all three sensors rapidly slope upwards, indicating noise characterized as *rate random walk* and *drift rate random walk* σ_{AD}, which quantifies that measurement drift at longer time scales are apparent. The values for *Angle Random Walk (ARW)* and *BI* are listed in Table 4.4. Further, the sensor drifts, determined by linear regression fitting of the measurement series are also listed in the same Table.

Discussion: No datasheet or detailed specifications for the integrated IMU were available to direct compare with the obtained results. However, based on the observed performance metrics, especially the obtained random walk values, which correspond to a noise amplitude of the order of $10^{-3}\frac{\mathrm{m/s^2}}{\sqrt{\mathrm{Hz}}}$ for the accelerometer and $10^{-3}\frac{\mathrm{deg/s}}{\sqrt{\mathrm{Hz}}}$ for the gyroscopes suggest that the device is a simple consumer-grade IMU based on a comparison with the values in the datasheet of the *TDK MPU-9250* IMU [43]. These type of IMU's are typically used for detecting motion and not for navigation tasks. Additionally, the accelerometer measurements in the y-direction show a noticeable deviation compared to the other axes, which can not be explained.

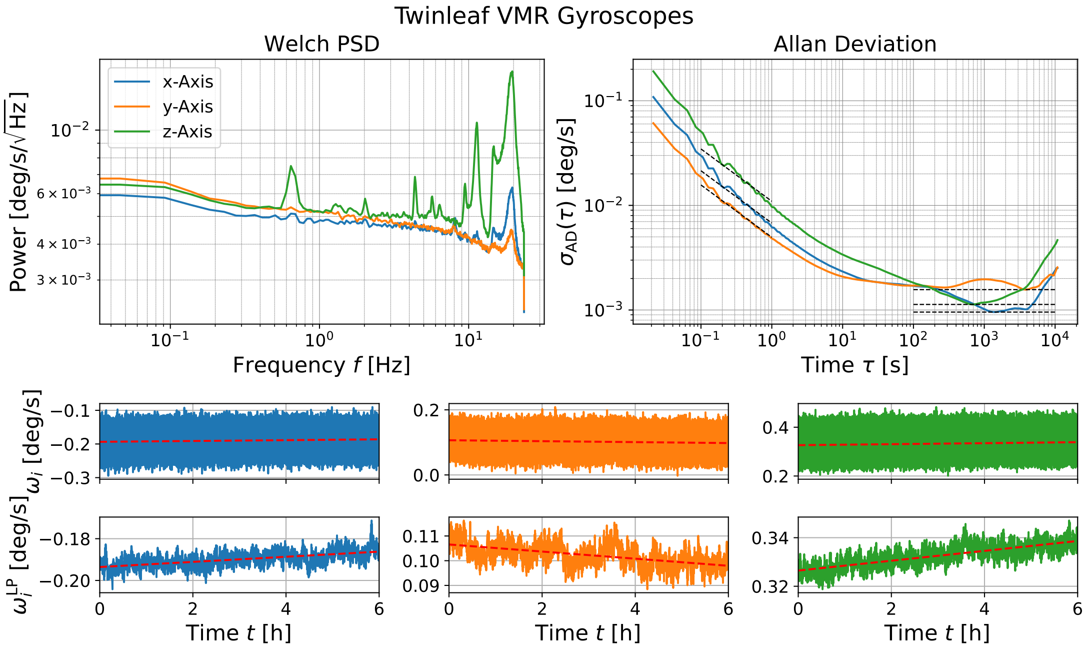

Figure 4.13: Gyroscope Noise and Drift Overview: (*Upper row, left*) Power Spectral Density. (*Upper row, right*) Allan Deviation. (*Middle row*) Raw time series data of the accelerometer recordings, including a linear fit for each axis. (*Bottom row*) Low-pass filter applied to the raw data of each axis, including a linear regression.

Table 4.4: Accelerometer and Gyroscope Noise and Drift

	Accelerometer			**Gyroscopes**		
Axis	*VRW* $\left[\frac{\mathrm{m/s}}{\sqrt{\mathrm{h}}}\right]$	*BI* $\left[\frac{\mathrm{m/s}}{\mathrm{h}}\right]$	$m\left[\frac{\mu\mathrm{m/s}^2}{\mathrm{h}}\right]$ (R^2)	*ARW* $\left[\frac{deg}{\sqrt{\mathrm{h}}}\right]$	*BI* $\left[\frac{deg}{\mathrm{h}}\right]$	$m\left[\frac{\mathrm{mdeg/s}}{\mathrm{h}}\right]$ (R^2)
x	0.19	0.45	$49.7\ (0.13)$	0.41	5.18	$1.22\ (0.35)$
y	17.46	14.38	$-83.2\ (0.05)$	0.30	8.49	$-1.45\ (0.31)$
z	0.57	0.57	$50.1\ (0.04)$	0.66	6.13	$2.02\ (0.65)$

Magnetometer Noise and Drift Quantification

Prior to conducting long time series and carrying out the planned laboratory experiment, the environmental noise in different rooms was analyzed. Therefore, environmental noise in various rooms within the building was measured. Short time series with duration of $5\mathrm{min}$ were recorded in these rooms to identify the one with the lowest environmental noise. In total, measurements were taken in eight different rooms.

In Figure 4.14, a comparative overview of both the magnetometers at hand of the recording in the laboratory room and in the basement room with the lowest noise is shown. In the overview, the PSD plots, the time series is plotted and further the histograms of the time series are shown.

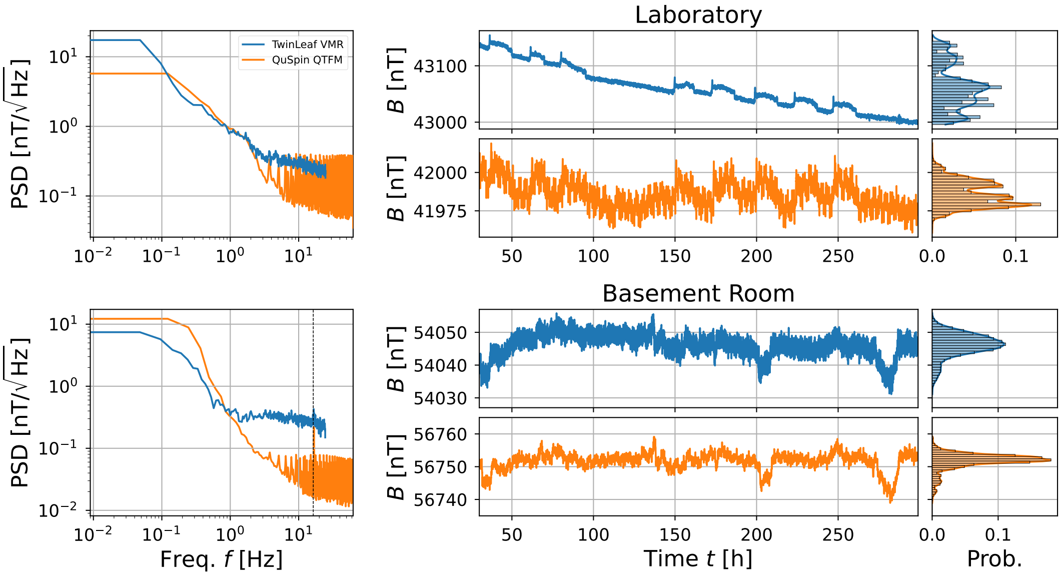

Figure 4.14: (*Upper row*) Recording in the laboratory. (*Lower row*) Recording in the basement room with the lowest noise. (*First column*) PSD plots of both magnetometers. (*Middle column*) Time series plots. (*Last column*) Histograms of the time series.

Examining the PSD plots for both magnetometers in the laboratory room reveals similar noise levels for both magnetometers. The primary difference between them arises from their differing sampling rates, which affect the maximum frequency shown in the PSD due to the Nyquist limit. The time series plots also show similar patterns, indicating that both magnetometers are capturing the same environmental magnetic noise. Additionally, both magnetometer measurement series have a slight downward trend in their signals. However, the slope of this trend in the *TwinLeaf VMR* is approximately five times greater than that observed in the *QuSpin QTFM*.

In the basement room, where the lowest noise floor was recorded, the *QuSpin QTFM* demonstrates a noise floor roughly one order of magnitude lower than in the laboratory environment. In contrast, the *TwinLeaf VMR* shows a similar noise level to that measured in the laboratory. The time series plots again confirm that both sensors are detecting the same environmental noise, but with noticeably reduced short-term fluctuations in the *QuSpin QTFM*. This difference is further illustrated in the histograms of the time series, where the *QuSpin QTFM* has a much sharper and narrower distribution, with a spread of approximately $5\mathrm{nT}$.

Similar to the noise and drift quantification of the IMU sensors, an analysis of the magnetometers was conducted. Comparable overviews containing the *PSD plot*, the *AD plot*, the raw data with a linear regression, and the low-pass filtered raw data (averaged over $10\mathrm{s}$) along with the same linear regression were prepared for each of the magnetometers. Figure 4.15 shows the overview for the *TwinLeaf VMR*. Focusing on the AD plot, it is evident that the magnetometers in the x and z-directions, which are not aligned with the main magnetic field direction, exhibit *Gaussian* white noise. Furthermore, the magnetometer in the y-direction also contains white noise, as it initially slopes with $m = -0.5$ in the log-log plot. However, this noise is overpowered by another process that induces additional noise, causing a turning point with an upward slope. This noise is especially due to the deviation in the first two hours of recording, which can not be explained. By calculating the AD deviation from time $t \in [2\mathrm{h}, 6\mathrm{h}]$ and plotting them over τ (dashed orange line in the AD plot) it can be seen that the hump can be minimized.
The minimum region with slope $m = 0$ for the x and z magnetometers is reached for $\tau \in [4 \cdot 10^1\mathrm{s}, 6 \cdot 10^1\mathrm{s}]$. Following this region, both axes slope rapidly upwards, characterizing *rate random walk* and *drift random walk*. This early drift rate from both magnetometers is also visible in the raw data time series and the linear fit. Both magnetometers exhibit faster drift rates, which increase the magnetic field strength compared to the magnetometer in the y-direction. In contrast, the minimum region of the magnetometer in the y-direction is reached at $\tau = 1.5 \cdot 10^3\mathrm{s}$.
The values obtained from the AD plot, such as the random walk value and the *drift rate*, are listed in Table 4.6. Hereby, the drift rate is calculated by linear fitting a slope with $m = 1$ to the values above time $\tau > 5 \cdot 10^3$. Additionally, the drift term $m_lin.$ obtained through linear regression is also included in the same table with its respective R^2 value. Looking at the PSD there are no visible peaks in any frequency except to small ones at frequency $f = 1\mathrm{Hz}$ for the magnetometers in x and z-direction.

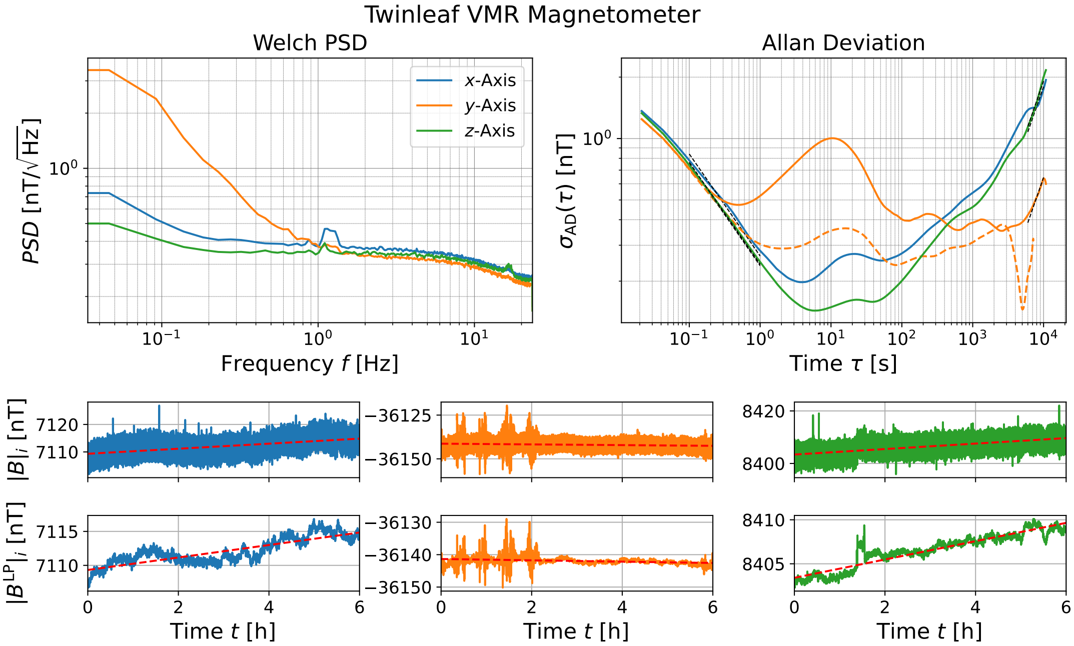

Figure 4.15: *TwinLeaf VMR* Noise and Drift Overview: (*Upper row, left*) Power Spectral Density. (*Upper row, right*) Allan Deviation. (*Middle row*) Raw time series data of the accelerometer recordings, including a linear fit for each axis. (*Bottom row*) Low-pass filter applied to the raw data of each axis, including the same linear fit.

Table 4.5: *TwinLeaf VMR* Noise and Drift Performance Measures

	Allan Deviation		**Lin. Regression**	
Axis	*RW* $\left[\frac{\text{nT}}{\sqrt{\text{Hz}}}\right]$	*DR* $\left[\frac{\text{nT}}{\text{h}}\right]$	m_{lin} $\left[\frac{\text{nT}}{\text{h}}\right]$	(R^2)
x	0.266	0.689	0.919	(0.69)
y	0.238	$(-)0.232$	-0.204	(0.07)
z	0.242	0.689	1.041	(0.87)

The noise and drift analysis overview for the *QuSpin QTFM* is shown in Figure 4.16. In addition, the same analysis as described previously was conducted using only the total magnetic field intensity of the *TwinLeaf VMR*, enabling a direct comparison between the two magnetometers.

Looking at the AD plot, no clear *Gaussian* white noise is apparent. For $\tau < 1 \cdot 10^{-2}$, the

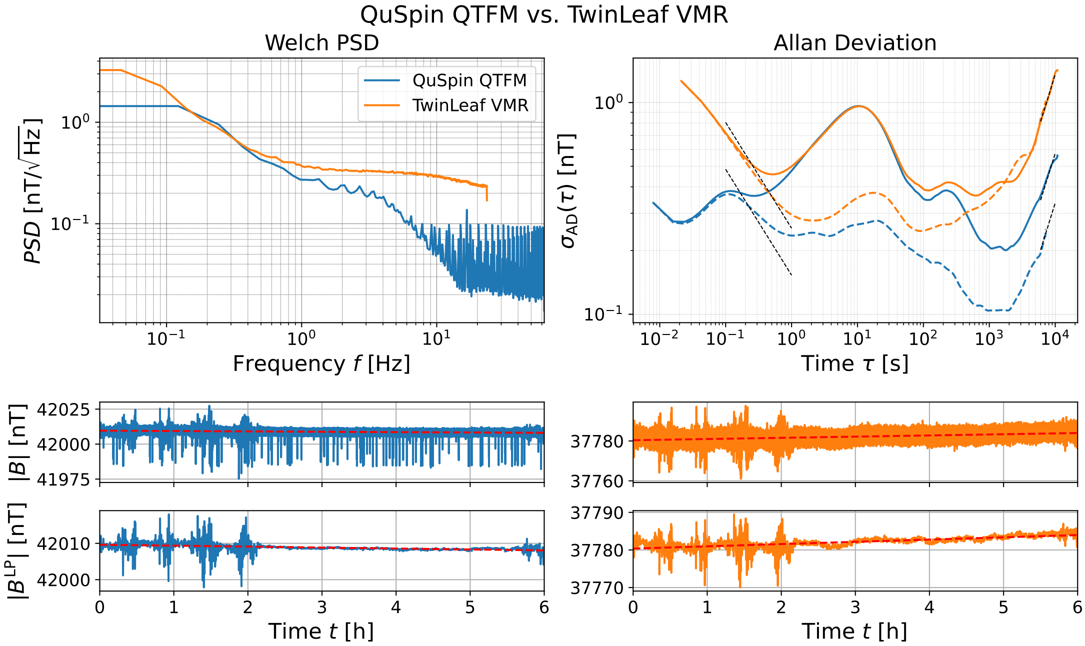

Figure 4.16: *QuSpin QTFM* Noise and Drift Overview with side-by-side comparison to the total measurement *TwinLeaf VMR*: (*Upper row, left*) Power Spectral Density. (*Upper row, right*) Allan Deviation. (*Middle row*) Raw time series data of the accelerometer recordings, including a linear fit for each axis. (*Bottom row*) Low-pass filter applied to the raw data of each axis, including the same linear fit.

Table 4.6: *TwinLeaf VMR* vs. *QuSpin QTFM* Noise and Drift Performance Measures

	Allan Deviation		**Lin. Regression**	
Magnetometer	*RW* $\left[\frac{\mathrm{nT}}{\sqrt{\mathrm{Hz}}}\right]$	*DR* $\left[\frac{\mathrm{nT}}{\mathrm{h}}\right]$	m_{lin} $\left[\frac{\mathrm{nT}}{\mathrm{h}}\right]$	(R^2)
TwinLeaf VMR	0.266	0.489	0.600	(0.42)
QuSpin QTFM	-	$(-)0.208$	-0.261	(0.14)

slope appears to be $m = -0.5$, but this behavior is disturbed by the same type of noise that was also observed in the *TwinLeaf VMR*. This is evident from the overlapping curves in the range $\tau \in [1\text{s}, 4 \cdot 10^2\text{s}]$, where both magnetometers behave identically. It was found that the deviation causing this disturbance originates from variations within the first two hours of recording, which is visible in the time series plots of both magnetometers. Since the

accelerations were recorded simultaneously, it can be ruled out that the cause is vibrations of the setup or other kinds of motion.
At higher averaging times, the *QuSpin QTFM* reaches its minimum region (slope $m = 0$) at a later time, around $\tau = 0.8 \cdot 10^3\mathrm{s}$, and exhibits a lower Allan deviation value σ_{AD} compared to the *TwinLeaf VMR*, which reaches its minimum at $\tau = 7 \cdot 10^2\mathrm{s}$ with a higher deviation. Furthermore, based on the drift rates obtained from linear regression of the raw data, it is apparent that the drift rate of the *TwinLeaf VMR* is higher than that of the *QuSpin QTFM*.

Comparing the raw time series of both magnetometers reveals that they detect the same noise patterns within the first two hours of recording. However, the raw measurements from the *QuSpin QTFM* also show additional outliers, which periodically decrease the magnetic field measurement by approximately $\Delta B = 30\mathrm{nT}$. These outliers are not present in the *TwinLeaf VMR* data. Applying a low-pass filter with a window of $10\mathrm{s}$ effectively removes these outliers.
Finally, examining the PSD plots of both magnetometers shows that the *QuSpin QTFM* has a significantly lower noise floor for frequencies above $f > 1\mathrm{Hz}$.

Discussion: Noise and drift analysis of the magnetometers was conducted in indoor environments without any active compensation for electromagnetic interference. Time series measurements were taken in different rooms within the building to identify the location with the lowest environmental noise levels. This was done not only to select the room with the lowest noise for the drift and noise comparison between the classical magnetometer and the quantum-based one but also to find a suitable space for conducting the laboratory experiment.

As briefly mentioned in the theory section, indoor environments tend to be electromagnetically noisy due to the presence of conduits, electronic devices, and other sources of magnetic disturbances. This was evident in both the short- and long-term measurement series. As a result, it was not possible to fully isolate sensor intrinsic noise as specified by the manufacturers and drift, as the environmental noise tended to be of higher magnitude. Typically intrinsic noise characterization of magnetometers is conducted in highly shielded environments, often using mu-metal chambers to shield from external magnetic field. Further methods consist of Helmholtz coils, where these setups incorporate reference magnetometers and feedback-controller to actively compensate for environmental magnetic noise. For more accurate noise analysis and performance evaluation, a controlled and shielded environment is essential.

Furthermore, while Allan deviation plots are commonly used for characterizing inertial sensors, they are less frequently applied to magnetometers. However, work from 2014 [44] proposed the use of Allan deviation analysis for magnetometers, especially as low-cost MEMS magnetometers have become more widespread due to their integration into MEMSs IMUs. The Allan deviation plot provides a useful overview of the stochastic processes present in the measurement series.

Comparing the drifts of both magnetometers at hand, it is clearly evident that the classical magnetometers exhibit drift, especially in the axis perpendicular to the direction of the main magnetic field. However, further examination of the quantum-based magnetometers reveals that the Allan deviation plot also shows typical drift rates for high τ values, but with much lower magnitude. Additionally, a slope linear regression of the measurement series shows a slight drift rate, yet with a very low R^2 value, indicating that the linear fit does not capture the measurement trend very well. Furthermore, this drift cannot be distinctly separated from other low-frequency drift of the magnetic field it is in.

4.2.2 Constructed Magnetic Field Maps

The recorded and constructed magnetic field maps for use in magnetic field aided navigation are presented in this section. As noted in the previous section, the influence of conduits, electronic devices emitting electromagnetic fields, and the high noise levels in the laboratory room were found to be negatively affecting the magnetic field aiding navigation. To mitigate this, the laboratory experiment was conducted in the basement room of the building, where lower environmental noise was detected. Further, as still noises are apparent in the basement room to enhance the navigation ability the planned variability of the map was increased by adding more magnets than planned.

As the room chosen is a formal engine testing room and made up of visible steal beams in the near proximity of the setup the magnetization of the room was recorded first. The resulting magnetic field map without any magnets is shown in Figure 4.17 (*left*). Several different magnet arrangements were recorded. Figure 4.17 (*right*) shows one such map as an example. Further mapped and recorded magnetic field arrangements are shown in the Appendix. In all cases, the magnetic fields were sparsely recorded, as described in Section 3.4.4, and *Kriging* interpolation was applied to estimate the missing values. The experimental variogram and the fitted theoretical variogram for interpolation to construct the presented map of Figure 4.17 (*right*) are presented in the Appendix.

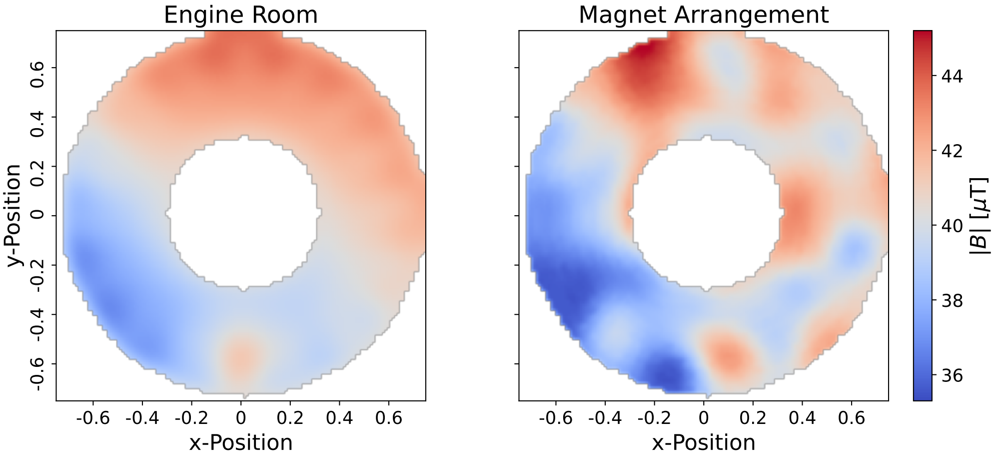

Figure 4.17: (*Left*) Constructed magnetic field map without any magnets. (*Right*) Example of a constructed magnetic field map (20250305_0921).

Further analysis is performed on if and how the magnetic field map changes over time. Figures 4.18 show the maps recorded from the same magnet arrangement, with a 6 hour time difference between them. The first column shows the initially recorded map, while the second column shows the map of the second recording. The first row represents the recorded magnetic field measurements, while the second row illustrated the fully constructed magnetic field.

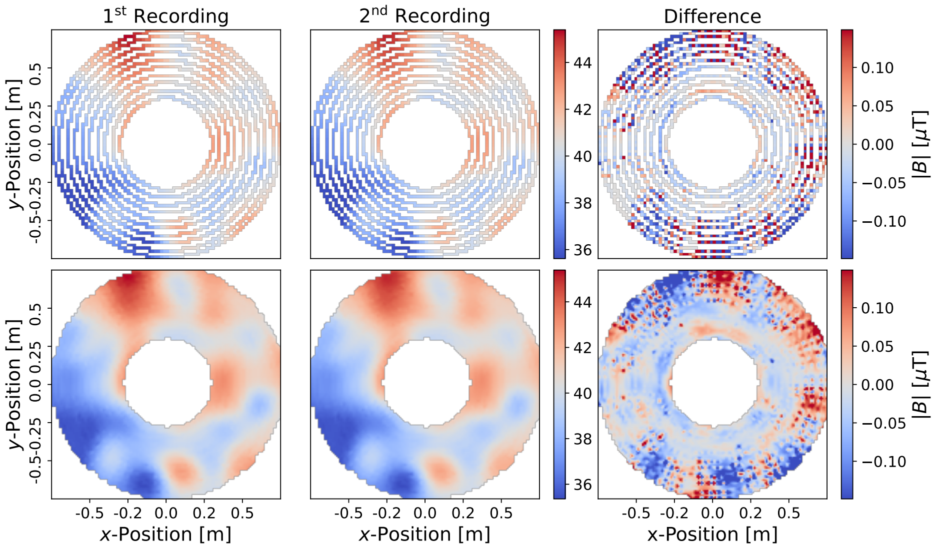

Figure 4.18: (*Left Column*) Initial map recording and the resulting interpolated map. (*Middle Column*) Second recording of the same map, taken six hours after the first. (*Right Column*) Difference in magnetic field strength between the two recordings.

Visually, the two magnetic field maps of the first and second recording appear very similar. However, when the difference between the two maps is computed, deviations become apparent. The difference between the two recordings are depicted in Figure 4.18 (*right column*). It is found that deviations within the center of the ROI are in the range of $\pm 50\mathrm{nT}$ in this magnetic arrangement. At the edges of the ROI the deviations become more extreme to with also regions of the map that deviate more than $\pm 150\mathrm{nT}$. Similar magnitudes of deviation between different recordings of the same magnet arrangements were observed across multiple maps, some of which are included in the Appendix. However, no consistent patterns in the appearance of these deviations were found.

Additionally, Figure 4.19 presents the standard deviation of the measurements that fall within each pixel. Figure 4.19 (*left*) shows the standard deviation from the first map recording, and Figure 4.19 (*right*) shows the standard deviation from the second recording. When comparing the two, the standard deviations exhibit a similar pattern. This pattern also correlates with the difference between the two recordings shown in the previous figure, Figure 4.18 (*right column*).

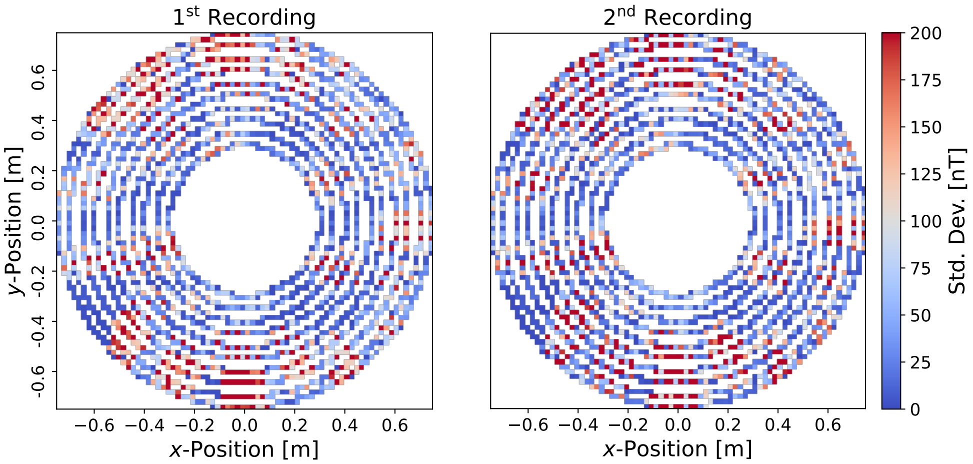

Figure 4.19: (*Left*) Standard deviation of the magnetic field measurements that fall within the same pixel of the first map recording. (*Right*) Standard deviation of the measurements that fall within the same pixel of the second map recording.

Discussion: An initial magnetic field map of the room's structural magnetization, as well as a map showing the magnetic field of a magnet arrangement, were presented. The baseline field of the considered ROI was visualized and shows a gradient magnetic field towards the steel beams of the room. The added permanent magnets successfully introduced some more variation into the magnetic field. This variations are used to gain position information for the magnetic navigation.

Despite the fact that magnetic field data for map construction was downsampled and low-pass filtered before averaging measurements within each pixel, significant variance between two recordings of the same magnet arrangement was still observed. Unfortunately, the exact magnet configurations were not documented photographically. It appears that standard deviation within individual pixels increases in regions with higher field gradients, suggesting a potential sensitivity to these regions. Additionally, deviations between the recorded maps may result from shifts in the room's structural magnetization or other environmental influences. In particular, ongoing construction near the recording area, including the movement of forklifts, pipes, and large metal beams, possibly contributed to fluctuations in the magnetic environment during data collection.

4.2.3 Magnetic Field-aided Navigation

This section presents the attempts for magnetic field aided navigation within the laboratory experiment. The magnetic field map used in the further course is depicted in the Appendix.

Figure 4.20 illustrates the results of the pure INS navigation estimate and the magnetic field aided navigation algorithm using raw IMU measurements. The raw IMU measurements incorporate the static calibration as described in the Section 3.4.3. Looking at position estimate of the pure INS, position drift occurs rapidly. A position error of approximately $1\mathrm{m}$ is reached within the first 20 seconds.

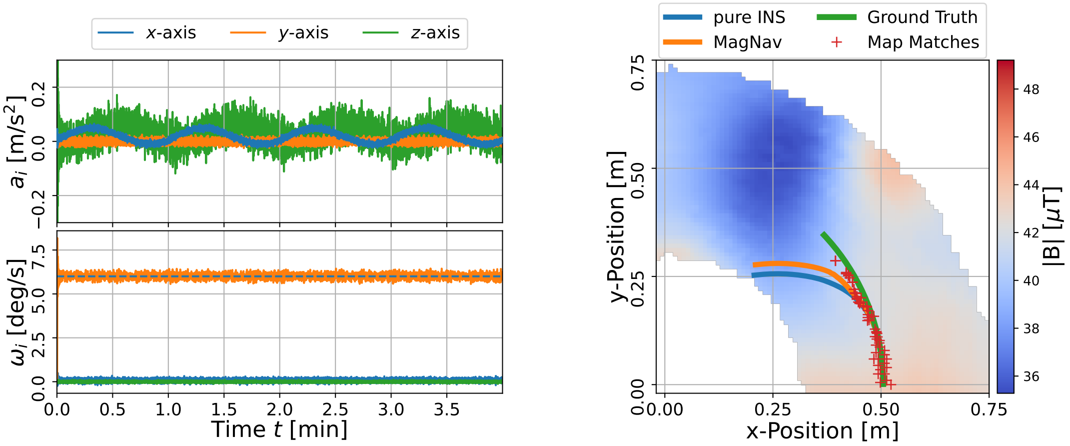

Figure 4.20: (*Left*) Raw IMU measurements in the body frame, after static bias removal. (*Right*) Magnetic field-aided navigation attempt using the raw IMU measurements.

The attempt to implement magnetic field-aided navigation with these accelerations is also depicted also in the same Figure 4.20 (*right*). To address the high position drift observed in the IMU, the batch length was set to 1, and the algorithm was adapted setting the map matching frequency to a maximum to compensate for the high drift rate. While the algorithm initially tries to correct the drift, the measured accelerations are too high, causing the estimated velocity to diverge from the true velocity. As a result, the position drift becomes too severe for the algorithm to correct the position effectively.

Examining the raw IMU data, depicted in Figure 4.20 (*left*), it is evident that the accelerations exhibit cyclic variations, leading to much higher velocities than expected. The expected accelerations in the body frame should be constant for the body-axis, in this case the x-axis of the IMU, that is aligned radially towards the axis of rotation. This is because only centripetal force should be acting on the body in the horizontal plane. Furthermore, the centripetal acceleration corresponding to a rotational speed of $1\mathrm{RPM}$ with a radius of $r = 0.55\mathrm{m}$ is $a_c = 0.0055\frac{\mathrm{m}}{\mathrm{s}^2}$.

These cyclic deviations are caused by changes in roll and pitch angles during the circular movement, which allow gravity to affect the accelerometers in the horizontal plane. This was found by taking stationary acceleration measurements along the circular trajectory. The angle of roll θ and pitch ϕ can be calculated by using the following equations:

$$\theta = \arctan\left(\frac{-a_x^b}{a_y^b}\right), \phi = \arcsin\left(\frac{-a_z^b}{9.81}\right) \tag{4.3}$$

Figure 4.21 (*bottom left*) shows the recovered roll and pitch angles along the recorded rotations, derived from the measured static accelerations. It can be seen that these angle deviations perfectly coincide with the cyclic deviation of the measured accelerations. To compensate for roll and pitch changes, three different approaches were tested. The first in-

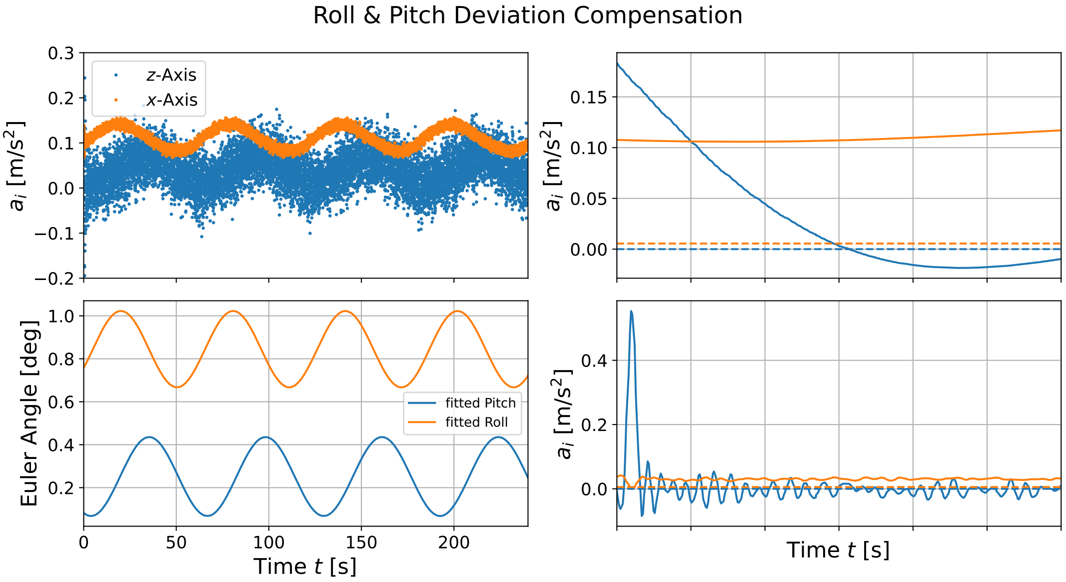

Figure 4.21: (*Upper left*) Raw body accelerations in the horizontal plane, incorporating static calibration. (*Bottom left*) Recovered and fitted roll and pitch angle deviations along the circular trajectory. By synchronizing the yaw angle with these deviations, angle variation over time can be recovered. (*Upper right*) Accelerations after applying notch and low-pass filters. (*Bottom right*) Accelerations after removal of the gravitational component due to roll and pitch angle deviations.

volved applying a notch bandpass filter to remove frequency components around the rotation frequency corresponding to $1\mathrm{RPM}$. Additionally, to mitigate vibrational artifacts, a high-pass filter was employed. The results of the filtered accelerations are shown in Figure 4.21 (*upper right*). The filter effectively removes both low- and high-frequency components from the acceleration signals, as the cyclic behavior is no longer present. However, the resulting acceleration for the x-axis is approximately 200 times greater than the expected centripetal acceleration, still leading to excessive position drift.

The second approach involved tracking the initial roll and pitch angles by incorporating gyroscope measurements, depicted in Figure 4.20 (*bottom left*) to dynamically calculate and correct for roll and pitch deviations while in motion. However, this method proved not viable, as the gyroscope measurements even after static calibration still exhibit small biases, leading to diverging Euler angles after integration. Furthermore, the gyroscope measurements do not show the sinusoidal graph necessary to explain the roll and pitch angle fluctuations.

The third approach involved using the recovered roll and pitch angle deviations along the trajectory and linking them to the heading angle. By knowing the yaw position, which is already tracked in the INS, roll and pitch can be compensated. The resulting accelerations of this approach are shown in Figure 4.21 (*bottom right*). This approach successfully remove the cyclic behavior of the accelerations and downscaled them toward the expected centripetal acceleration. However, the resulting acceleration is still approximately a factor of 10 higher than expected.

To overcome the issues associated with acceleration measurements and to focus on magnetic field-aided navigation, accelerations were derived from rotation stage angle measurements. Furthermore, additional noise was introduced into the derived accelerations to simulate noisy IMU measurements for the subsequent analysis. Acceleration noise of about $a_{\text{Noise}} = 1 \cdot 10^{-4}\mathrm{m/s^2/\sqrt{Hz}}$ was introduced, as noise levels of the accelerometers at hand, with about $a_{\text{Noise}} = 1 \cdot 10^{-3}\mathrm{m/s^2/\sqrt{Hz}}$ identified in Section 4.2.1 are at the same order as the expected acceleration.

Firstly, magnetic field measurements along the true trajectory were evaluated using map matching. For this, the measurement bound, which sets the interval for when a map match is found, was set to $\sigma = 30\mathrm{nT}$, and a fixed search radius of $r_s = 3\mathrm{cm}$ was used. Map matching was performed for each magnetometer measurement. Figure 4.22 presents the results of this map matching evaluation. It is apparent that map matches were not found at every point along the trajectory with the given set of parameters and measurements. Furthermore, looking at the deviations between the true position and the resulting PDA position estimate, most position estimates have a deviation within $0.75\mathrm{cm}$ and $1.25\mathrm{cm}$. However, there are

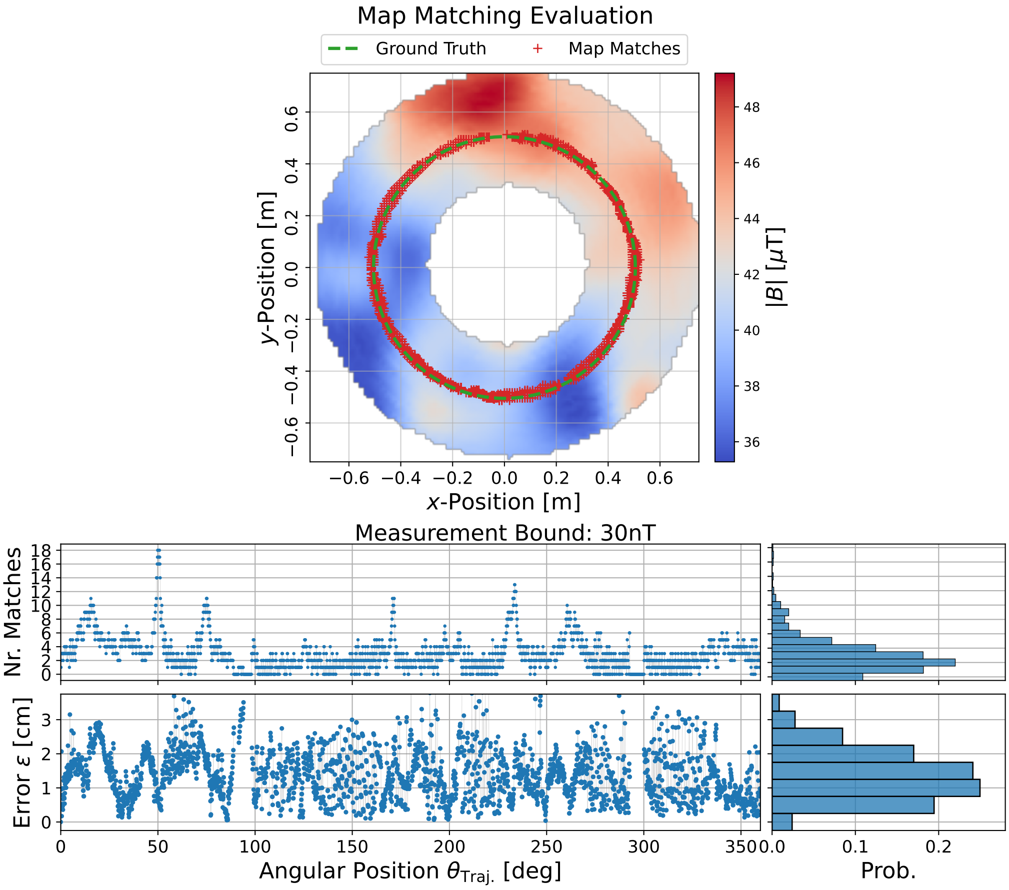

Figure 4.22: (*Upper*) Map Matches found along the true trajectory. (*Bottom*) Respective number of matches and the error of calculated PDA position estimate.

considerable share of estimates where the error exceeds $2\mathrm{cm}$.

Similar figures to Figure 4.22, showing results for varying measurement bounds, are provided in the Appendix. As expected, a lower bound results in fewer map matches, which tends to lead to higher map matching errors. In contrast, a higher bound yields more map matches, but the error distribution remains similar to that shown for $\sigma = 30\mathrm{nT}$.

Magnetic field navigation was attempted using simulated IMU measurements, magnetic field data from the *QuSpin QTFM*, and the corresponding constructed magnetic field map. Following the approach used in the previous laboratory simulation experiments, a batch length of 20 and a map matching rate of $20\mathrm{Hz}$ were selected. The optimal parameter set of the UKF identified in the simulations in Section 4.1.1 were used. The first half of the rotation was omitted, as this phase includes a ramp-up period of the rotation stage coming up to the set speed of $1\mathrm{RPM}$, during which the accelerations fluctuate significantly. As a result, the navigation attempts do not begin at the '3 o'clock' position but instead start at '9 o'clock'.

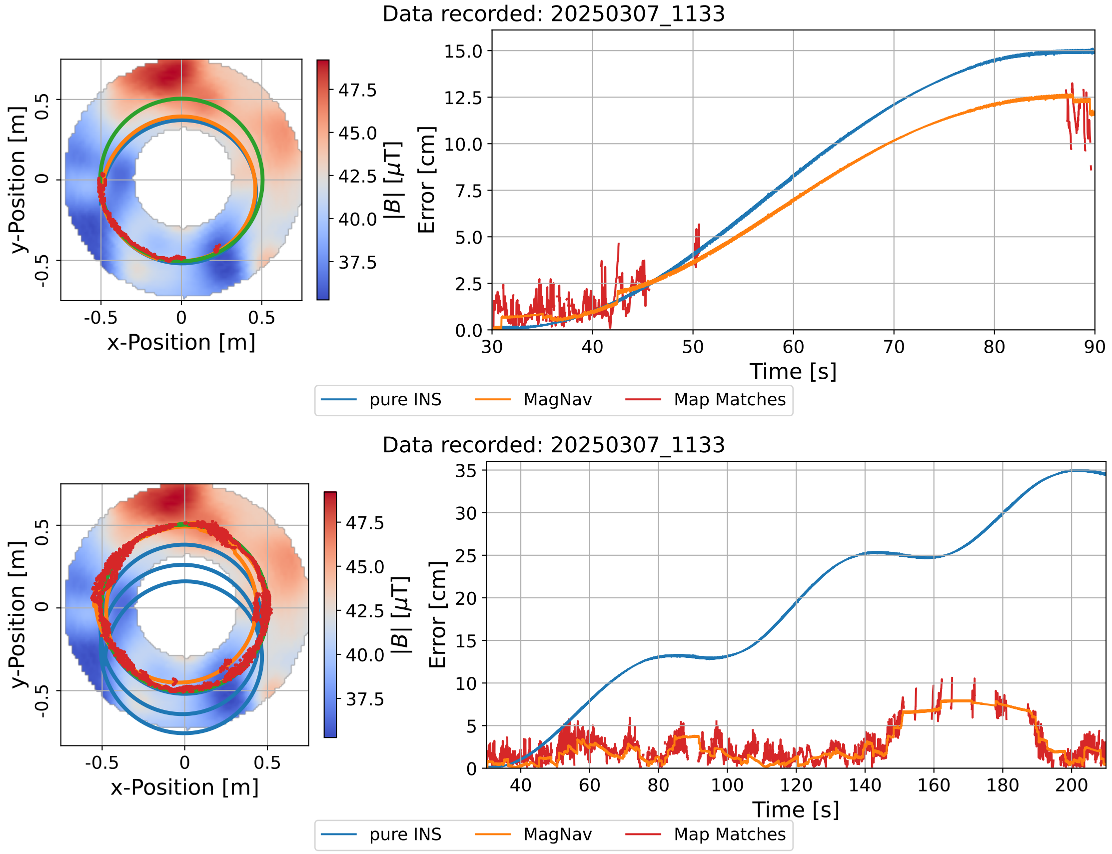

Figure 4.23: Example results of magnetic field-aided navigation attempts within the laboratory experiment. (*Top row*) Batch length set to 20. (*Bottom row*) Batch length set to 5. (*Left column*) Navigation result. (*Right column*) Respective error plots.

Examining the navigation results of the selected recording 20250307_1133, it is evident that the algorithm identifies matches within $2.5\mathrm{cm}$ of the true position during the first quarter of rotation. However, no substantial correction occurs, as the position error diverges at a rate similar to that of the pure INS position estimate. This is visualized in Figure 4.23 (*right*). The map matches, visualized as red dots, show a mix of both accurate matches with low error and incorrect matches with higher position error.

By decreasing the batch length from 20 to 5, which results in a higher navigation correction rate, the navigation performance of this recording can be improved. The navigation result is shown in Figure 4.23 (*bottom row*). During the first two rotation, $t \in [30\mathrm{s}, 140\mathrm{s}]$, the maximum position error of the magnetic field-aided navigation is bounded to approximately $4\mathrm{cm}$. The mean absolute error within this time interval is approximately $1.2\mathrm{cm}$, which is close to the resolution of the magnetic field map. In comparison, unaided navigation results in a diverging position error of about $25\mathrm{cm}$ after the same duration. Furthermore, starting from the third rotation, corresponding to the time interval $t > 150\ \mathrm{s}$, the position error begins to increase. This increase is due to map matches with higher position errors, leading to a maximum navigation error of $8\mathrm{cm}$. However, this error is recovered in the last third of the third rotation, when $t \in [190\mathrm{s}, 210\mathrm{s}]$. During this period, map matches closer to the ground truth help recover the position, and the third rotation ends with a position error of about $1\mathrm{cm}$. In contrast, the pure INS position has an error of about $35\mathrm{cm}$ by that time.

A different result, where navigation aiding is successful for only the first half of the first rotation is observed in a recording taken approximately $10\mathrm{min}$ later. The corresponding error plot is provided in the Appendix under the title 20250307_1142.
Furthermore, the recording 20250307_1219 shows another different result, where magnetic field aided navigation position diverges early, resulting in a higher position error than the pure INS, due to incorrect position estimates of the map matching step. The result of this recording is also presented in the Appendix.

A total of 15 separate recordings were taken to evaluate navigation performance for this specific magnet arrangement. Each recording contains 3.5 rotations at a speed of $1\mathrm{RPM}$. The evaluation revealed mixed outcomes, with results similar to those presented, where some recordings showed bounded navigation errors for multiple full rotation or only partial rotations, while others diverge faster than the pure INS solution. Further examples are provided in the Appendix, where also results of the measurements taken from another magnetic field arrangement are presented. These examples further show the mixed outcomes of the magnetic field-aided navigation in the laboratory experiment.

Discussion: Magnetic field-aided navigation was attempted by fusing IMU measurements with magnetometer data in the planned real-world laboratory experiment.
Results from the first trial using raw sensor data showed that achieving accurate position estimates using only accelerometer and gyroscope measurements is challenging. It was also found that the laboratory setup had some flaws. A slight varying tilt in the IMU's angle along the circular trajectory caused deviations in the pitch and roll angles, resulting in the measurement of gravitational acceleration components. These excess accelerations led to fast divergence of the position estimate, which the map-matching algorithm could not effectively correct. Additionally, vibrations from the stepper motor of the rotating stage caused by

its stepwise, non-continuous motion introduced noise into the acceleration measurements. These vibrations were further amplified by the use of a carbon fiber rod on which the sensor were mounted. While this high-frequency noise from vibrations could be mitigated through low-pass filtering, correcting for angle deviations along the circular trajectory proved more challenging. By fitting the roll and pitch deviations, which were obtained from static acceleration measurements, to each position on the circular trajectory and removing these effects, the cyclic deviation in angles was successfully eliminated. However, the retrieved accelerations remained an order of magnitude higher than expected.

Therefore, accelerations were simulated using the angle measurements obtained from the rotation stage. Emulating the noise of the IMU was not feasible, as the expected SNR for the accelerations and the quantified rate random walk of the IMU is less than $SNR = 1$ for the IMU sampling rate of $50\mathrm{Hz}$, which was is too low for initial position estimates of the navigation aiding algorithm.

Evaluating the map-matching performance using the magnetic measurements and the constructed maps showed that significantly higher measurement bounds were required compared to the earlier simulations to achieve consistent matches along most of the trajectory. Furthermore, these map matches still showed deviations from the true trajectory, with a mean of about $1\mathrm{cm}$, which is the resolution of the constructed map. However, a considerable number of map matches have high errors, indicating that some of them actually cause greater divergence in position due to incorrect matching. The need for high sigma bounds, along with persistent map-matching errors, suggests that the environment is too noisy.

Despite a significant number of high-error matches identified during the map-matching evaluation, magnetic field-aided navigation was attempted using the recorded measurements for the magnetic field map presented. As demonstrated in the example, the magnetic field-aided navigation algorithm was able to correct the position reasonably well for more than one rotation for some recordings using the optimal found UKF parameters α and β from the previous simulations made. Further, it was found that a shorter batch length was needed for the real life implementation to correct for the position drift. Multiple examples demonstrated successful position correction for one or more rotations, leading to the conclusion that the implemented magnetic field-aided navigation algorithm is capable of compensating for positional drift. Some recordings performed better than others, and cases where navigation failed were also observed.

Multiple measurements using different magnetic field arrangements further demonstrated the sensitivity of the experimental setup. This sensitivity is probably due to the noisy indoor environment in which the experiment was conducted, where no shielding was used to mitigate electromagnetic interference. Additionally, mechanical vibrations may have introduced deviations in the magnetic field measurements, due to the presence of strong gradients over short distances caused by the use of permanent magnets. Moreover, the small spatial extent of the experiment could also have contributed to measurement deviations. The OPM utilizes a vapor cell containing rubidium atoms, which itself has a spatial extent. When magnetic field gradients are present across this extent, the magnetometer's sensitivity decreases, potentially leading to discrepancies between measurements at same locations.

Future work should focus on conducting experiments outside of indoor environments or in more controlled settings to further reduce electromagnetic interference. Additionally, noise mitigation techniques should be explored and implemented in future work, as magnetic field signatures of the anomaly field are on the order of a few nT, while disturbances can be of the same order of magnitude or even higher. It would also be beneficial to design experiments with a specific application in mind. This would enable more targeted evaluation of the feasibility of magnetic navigation within that specific context.

5 Conclusion

Initial steps toward magnetic field-aided navigation have been taken. Two simulation scenarios and the results of magnetic field-aided navigation in a laboratory experiment were presented.

The simulation of the laboratory experiment demonstrated that magnetic navigation is feasible in the planned scenario. Furthermore, the simulation included an evaluation of how map noise influences the algorithm's ability to correct for it. An increase in map deviations led to a decrease in the overall performance of the magnetic navigation algorithm. Additionally, the simulations conducted based on using all three vector components of the magnetic field outperformed the total field simulations, which leads to the conclusion that using more than just one magnetic field map can enhance the navigation performance.

Furthermore, a simulation of the flight path using an available anomaly map of the were conducted to evaluate the algorithm's performance in a real world application. Initial parameter optimization demonstrated how the choice of UKF parameters influences the algorithm's navigation performance. It was observed that optimal parameters appeared to help bound the position error. A Monte Carlo simulation showed that, although the majority of simulations ended with a lower total error, the overall error along the trajectory was generally worse compared to pure INS navigation for the optimized parameter set evaluated. However, examining the best-performing simulations revealed that position correction is achievable, which suggests that further advancements of the algorithm is needed.

The laboratory experiment conducted showed that the implemented algorithm was able to successfully perform magnetic field-aided navigation for single and also multiple rotations. Although, the indoor environment presented electromagnetic interference that challenged real-world implementation and the IMU measurements had to be simulated because the measured accelerations significantly exceeded the theoretically expected values. The results are promising for further development, and future work should focus on conducting experiments that more accurately reflect real-world application scenarios.

Further improvements and advancements to the algorithm are both possible and necessary. The current approach, which relies on probabilistically fusing position estimates, depends on accurate covariance estimation of the map-matching locations. One potential solution could involve applying machine learning techniques to learn optimal covariances based on sensor measurements, map variability, and match quality. This could potentially eliminate the need for the UKF optimization step. Alternatively, machine learning could be used to learn not only the UKF parameters but also other key parameters such as search window sizes, measurement bounds, batch length, and more. Also interesting is the deployment of magnetic field-aided navigation using more components than just the total field intensity, such as the vector components or the gradients of the magnetic field. This is especially true given the plan in the department of Quantum Nano Physics, where this Master thesis takes place, to build a magnetometer array with multiple OPM magnetometers, which could enable gradiometer-based measurements for navigation and potentially allow the use of magnetic field signatures for velocity correction as well [45]. In addition, this approach minimizes temporal variations in the gradient magnetic field measurements, which are present in the scalar magnetic field data, as these deviations are canceled out when computing the spatial gradient [42]. Future work should focus on implementing magnetic field aiding within specific applications to further evaluate its feasibility and performance in context-specific scenarios.

Bibliography

[1] K. Wu and R. He. “Perspective: Magnetic quantum sensors for biomedical applications”. In: *Nanotechnology* 36.15 (2025), p. 152501. DOI: `10.1088/1361-6528/adb635`.

[2] J. S. Bennett et al. “Precision Magnetometers for Aerospace Applications: A Review”. In: *Sensors* 21.16 (2021), p. 5568. DOI: `10.3390/s21165568`. URL: `https://doi.org/10.3390/s21165568`.

[3] S. C. Bose. “GPS spoofing detection by Neural Network Machine Learning”. In: *IEEE Aerospace and Electronic Systems Magazine* 37.6 (2022), pp. 18–31. DOI: `10.1109/maes.2021.3100844`.

[4] T. Westbrook. “Aircraft vulnerability to politically motivated radio frequency interference (RFI) in Eastern Europe”. In: *Security and Defence Quarterly* (2024). DOI: `10.35467/sdq/178249`.

[5] A. Jafarnia-Jahromi et al. “GPS vulnerability to spoofing threats and a review of antispoofing techniques”. In: *International Journal of Navigation and Observation* 2012 (2012), pp. 1–16. DOI: `10.1155/2012/127072`.

[6] N. Priestley. “Terrain referenced navigation”. In: *IEEE Symposium on Position Location and Navigation. A Decade of Excellence in the Navigation Sciences*. 1990, pp. 482–489. DOI: `10.1109/PLANS.1990.66218`.

[7] Yurong Han et al. “An Improved TERCOM-Based Algorithm for Gravity-Aided Navigation”. In: *IEEE Sensors Journal* 16.8 (2016), pp. 2537–2544. DOI: `10.1109/JSEN.2016.2518686`.

[8] A. J. Canciani. “Absolute Positioning Using the Earth’s Magnetic Anomaly Field”. PhD Thesis. Air Force Institute of Technology, 2016.

[9] Anne Fabricant, Irina Novikova, and Georg Bison. “How to build a magnetometer with thermal atomic vapor: A tutorial”. In: *New Journal of Physics* 25.2 (2023), p. 025001. DOI: `10.1088/1367-2630/acb840`.

[10] X. Wang et al. "Quantum Diamond Magnetometry for Navigation in GNSS Denied Environments". In: *Gravity, Positioning and Reference Frames*. Ed. by Jeffrey T. Freymueller and Laura Sánchez. Cham: Springer Nature Switzerland, 2024, pp. 87–92. ISBN: 978-3-031-63855-8.

[11] J. Quintas, F. C. Teixeira, and A. Pascoal. "AUV geophysical navigation using magnetic data – the Medusa GN System". In: *2018 IEEE/ION Position, Location and Navigation Symposium (PLANS)*. 2018, pp. 1122–1130. DOI: `10.1109/PLANS.2018.8373495`.

[12] J. M. D. Coey. *Magnetism and Magnetic Materials*. Cambridge University Press, 2010.

[13] Peter Balch. *Flux Gate Magnetometer Experiments*. Accessed: 2025-03-26. 2021. URL: `https://www.instructables.com/Flux-Gate-Magnetometer-Experiments/`.

[14] S. Wei et al. "Recent Progress of Fluxgate Magnetic Sensors: Basic Research and Application". In: *Sensors* 21.4 (2021), p. 1500. DOI: `10.3390/s21041500`.

[15] Pavel F. Baranov, Vitalia E. Baranova, and Tamara G. Nesterenko. "Mathematical Model of a Fluxgate Magnetometer". In: *MATEC Web of Conferences*. VI International Forum for Young Scientists "Space Engineering 2018". Vol. 158. EDP Sciences, 2018, p. 01006. DOI: `10.1051/matecconf/201815801006`.

[16] B. B. Narod and J. R. Bennest. "Ring-core fluxgate magnetometers for use as observatory variometers". In: *Physics of the Earth and Planetary Interiors* 59.1–2 (1990), pp. 23–28. DOI: `10.1016/0031-9201(90)90205-c`.

[17] S. Yang and J. Zhang. "Current Progress of Magnetoresistance Sensors". In: *Chemosensors* 9.8 (2021), p. 211. DOI: `10.3390/chemosensors9080211`.

[18] Honeywell International Inc. *HMC1001 Single-Axis Magnetic Sensor Datasheet*. Datasheet, Honeywell International Inc. Accessed: 2025-03-15. 2005. URL: `https://www.sparkfun.com/datasheets/Sensors/Magneto/HMC1001-2.pdf`.

[19] Junwen Zou and Stephen D. Hogan. "Absolute static-field magnetometry, magnetic gradiometry, and vector electrometry with circular Rydberg atoms". In: *Phys. Rev. A* 107 (6 2023), p. 062820. DOI: `10.1103/PhysRevA.107.062820`. URL: `https://link.aps.org/doi/10.1103/PhysRevA.107.062820`.

[20] QuSpin. *QuSpin QTFM Gen-2*. Accessed: 2025-03-10. n.d. URL: `https://quspin.com/qtfm-gen-2/`.

[21] D. Hunter et al. "Free-induction-decay magnetometer based on a microfabricated CS Vapor Cell". In: *Physical Review Applied* 10.1 (2018). DOI: `10.1103/physrevapplied.10.014002`.

[22] Z.D. Grujić et al. "A sensitive and accurate atomic magnetometer based on free spin precession". In: *Eur. Phys. J. D* 69.135 (2015). DOI: `10.1140/epjd/e2015-50875-3`. URL: `https://doi.org/10.1140/epjd/e2015-50875-3`.

[23] H. Clevenson et al. "Robust high-dynamic-range vector magnetometry with nitrogen-vacancy centers in Diamond". In: *Applied Physics Letters* 112.25 (2018), p. 252403. DOI: `10.1063/1.5034216`.

[24] Aaron Kraft, Christoph Rupprecht, and Yau-Chuen Yam. "Superconducting quantum interference device (squid)". In: *UBC Phys* (2017).

[25] NASA's Scientific Visualization Studio. *Earth's Magnetosphere*. `https://svs.gsfc.nasa.gov/4663/`. Accessed: 2025-03-27. 2018. URL: `https://svs.gsfc.nasa.gov/4663/`.

[26] P. Alken, E. Thébault, C.D. Beggan, et al. "International Geomagnetic Reference Field: the thirteenth generation". In: *Earth, Planets and Space* 73 (2021), p. 49. DOI: `10.1186/s40623-020-01288-x`.

[27] R. Lanza and A. Meloni. *The Earth's Magnetism: An Introduction for Geologists*. Berlin: Springer, 2011.

[28] Aaron Canciani and John Raquet. "Absolute Positioning Using the Earth's Magnetic Anomaly Field: Magnetic Anomaly Navigation". In: *Navigation* 63.2 (June 2016), pp. 111–126. ISSN: 00281522. DOI: `10.1002/navi.138`. URL: `https://onlinelibrary.wiley.com/doi/10.1002/navi.138` (visited on 01/29/2025).

[29] Jacob Hollebon and Filippo Fazi. *Efficient HRTF Representation Using Compact Mode HRTFs*. Oct. 2020.

[30] Brian Meyer, Richard Saltus, and Arnaud Chulliat. *EMAG2v3: Earth Magnetic Anomaly Grid (2-arc-minute resolution)*. Version 3. 2017. DOI: `10.7289/V5H70CVX`. URL: `https://doi.org/10.7289/V5H70CVX`.

[31] D. K. Shaeffer. "MEMS inertial sensors: A tutorial overview". In: *IEEE Communications Magazine* 51.4 (2013), pp. 100–109. DOI: `10.1109/MCOM.2013.6495768`.

[32] Neil R. Claussen et al. *Magnetic Navigation for GPS-Denied Airborne Applications*. Tech. rep. Sandia National Lab. (SNL-NM), Albuquerque, NM (United States), Oct. 2020. DOI: `10.2172/1817974`. URL: `https://www.osti.gov/biblio/1817974`.

[33] Simon Haykin. "Kalman Filtering and Neural Networks". In: *Kalman Filtering and Neural Networks*. 2001. DOI: `10.1002/0471221546.ch1`.

[34] K. Nielsen et al. “UKF Parameter Tuning for Local Variation Smoothing”. In: *2021 IEEE International Conference on Multisensor Fusion and Integration for Intelligent Systems (MFI)*. 2021, pp. 1–8. DOI: `10.1109/MFI52462.2021.9591188`.

[35] Deokjin Lee. “Nonlinear Bayesian filtering with applications to estimation and navigation”. In: (Jan. 2005).

[36] H. Li et al. “Enhancing Precision in Magnetic Map Interpolation for Regions with Sparse Data”. In: *Applied Sciences* 14.2 (2024), p. 756. URL: `https://www.mdpi.com/2076-3417/14/2/756`.

[37] M. B. Marinov et al. “Analysis of Sensors Noise Performance Using Allan Deviation”. In: *2019 IEEE XXVIII International Scientific Conference Electronics (ET)*. 2019, pp. 1–4. DOI: `10.1109/ET.2019.8878552`.

[38] J. W. Mooney. “A biomagnetic field mapping system for detection of heart disease in a clinical environment”. PhD thesis. Great Britain: University of Leeds, 2018.

[39] J. Hidalgo et al. “Improving planetary rover attitude estimation via MEMS sensor characterization”. In: *Sensors* 12.2 (2012), pp. 2219–2235. DOI: `10.3390/s120202219`.

[40] Michael Ortner and Lucas Gabriel Coliado Bandeira. “Magpylib: A free Python package for magnetic field computation”. In: *SoftwareX* 11 (2020), p. 100466. URL: `https://doi.org/10.1016/j.softx.2020.100466`.

[41] W. F. Storms. “Magnetic Field Aided Indoor Navigation”. Master Thesis. Air Force Institute of Technology, 2009.

[42] Lauren A. Mount. “Navigation using Vector and Tensor Measurements of the Earth’s Magnetic Anomaly Field”. Theses and Dissertations. 1817. Master’s Thesis. Air Force Institute of Technology, 2018. URL: `https://scholar.afit.edu/etd/1817`.

[43] InvenSense Inc. *MPU-9250 Product Specification*. `https://product.tdk.com/system/files/dam/doc/product/sensor/mortion-inertial/imu/data_sheet/ps-mpu-9250a-01-v1.1.pdf`. 2016.

[44] Katarína Draganová et al. “Noise analysis of magnetic sensors using Allan variance”. In: *Acta Physica Polonica A* 126.1 (2014), pp. 394–395.

[45] M. Zmitri, H. Fourati, and C. Prieur. “Magnetic Field Gradient-Based EKF for Velocity Estimation in Indoor Navigation”. In: *Sensors* 20.19 (2020), p. 5726. DOI: `10.3390/s20205726`. URL: `https://doi.org/10.3390/s20205726`.

Appendix

A.1 Laboratory Simulation Examples

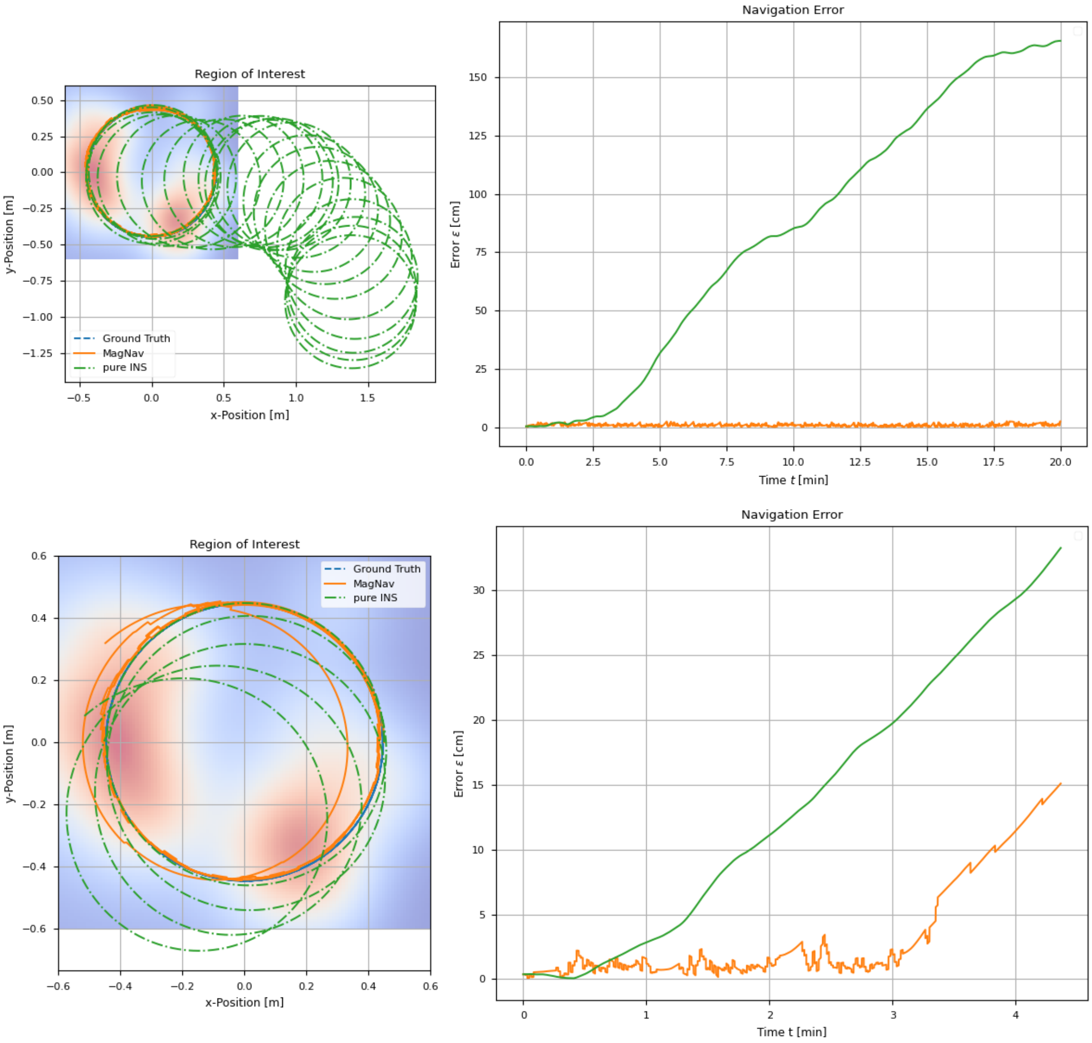

Figure A.1: Two examples of the laboratory simulation scenarios. (*Left*) Resulting trajectories. (*Right*) Respective error plots.

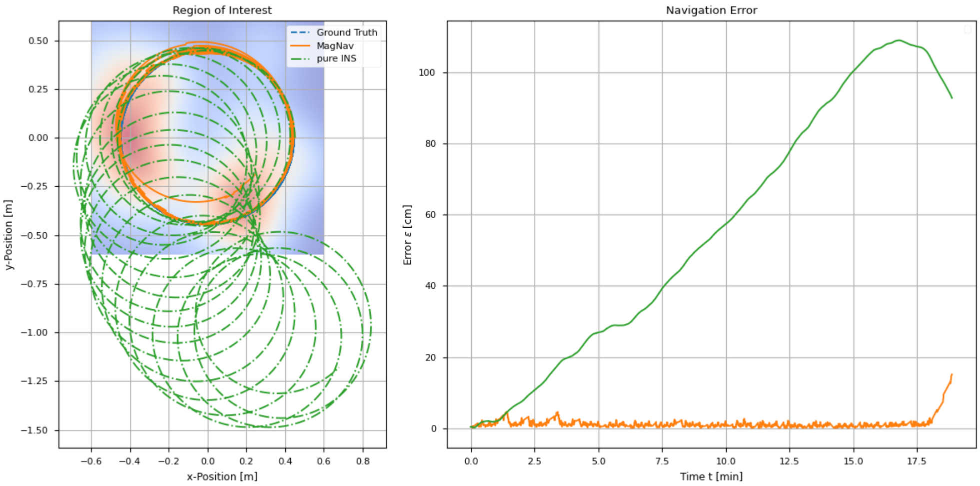

Figure A.2: Example of the laboratory simulation scenarios. (*Left*) Resulting trajectories. (*Right*) Respective error plots.

A.2 Flight Path Simulation Results: Simulation Case B

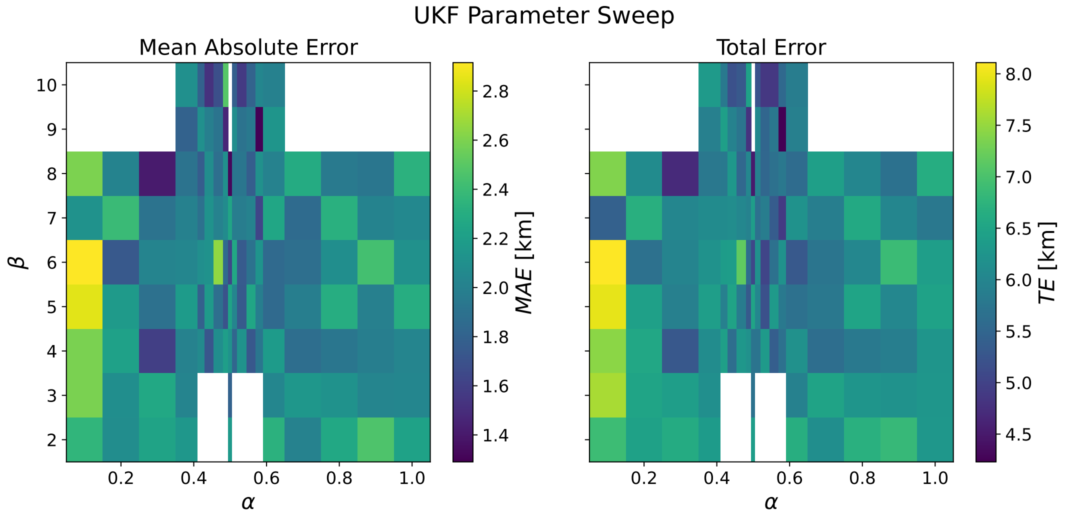

Figure A.3: Heat plots of the resulting mean Mean Absolute Error and Total Error for Simulation Case B of the UKF parameter sweep, which uses a magnetometer sampling rate of $1\ \mathrm{Hz}$ and a batch length of 25.

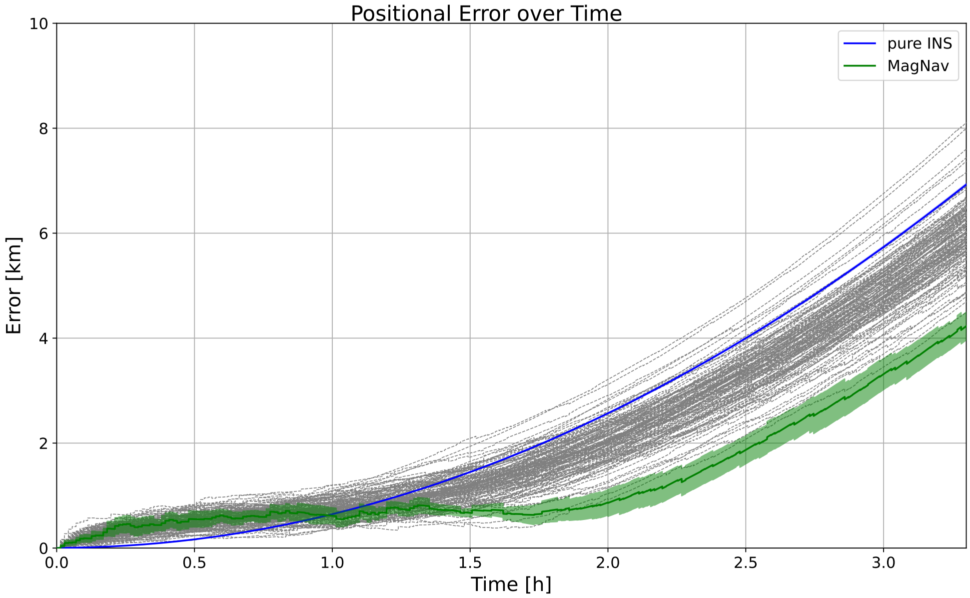

Figure A.4: Error plots of the different UKF parameter sets, showing the mean of all simulations that use the same UKF parameter sets for Simulation Case B. The green line with the shaded area represents the error plot with the respective $\pm\sigma$ region of the optimal UKF parameter set.

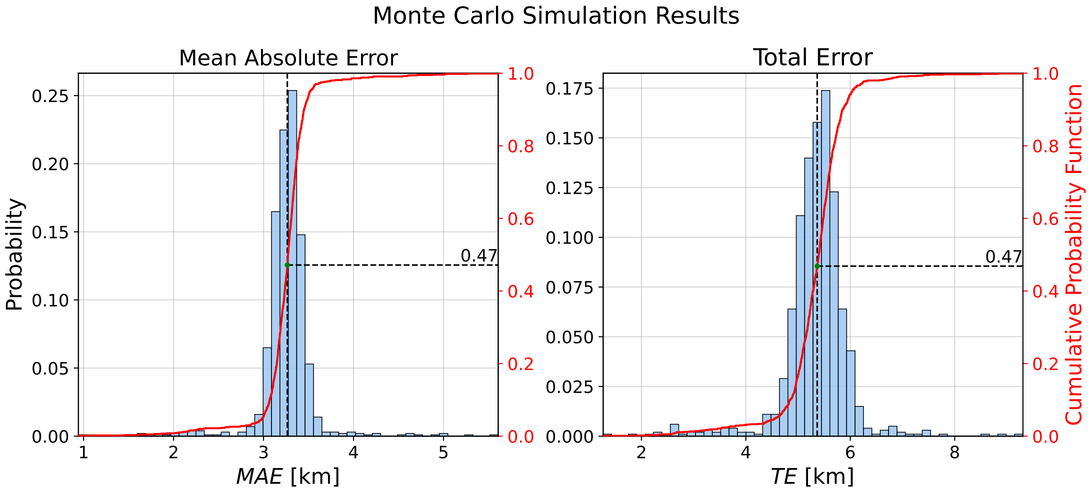

Figure A.5: Histograms of the Monte Carlo simulations for Simulation Case B are shown. The histograms display a narrow distribution around the mean of the errors from the pure INS solution for both the mean absolute error and the total error. This leads to the conclusion that the navigation-aiding algorithm, with the chosen parameters, does not significantly influence the navigation performance.

A.3 Recorded Magnetic Field Maps

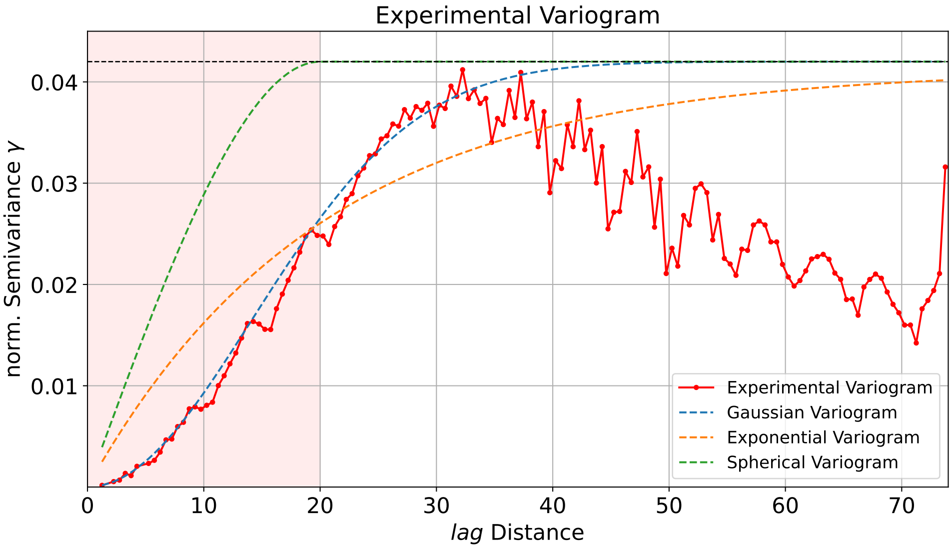

Figure A.6: Experimental variogram used in the *Kriging* interpolation step for map construction of the map 20250307_0827. A *Gaussian* variogram was found optimal, with a range of 20 and a normalized range of 0.04.

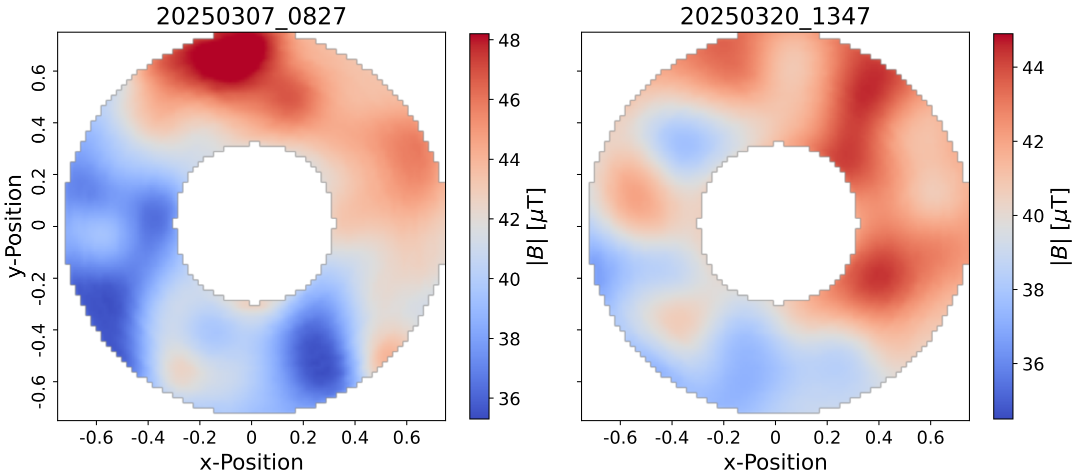

Figure A.7: Two magnetic field maps constructed for use in magnetic field-aided navigation experiments conducted in the laboratory. (*Left*) Map recorded at 20250307_0827. (*Right*) Map recorded at 20250320_1347

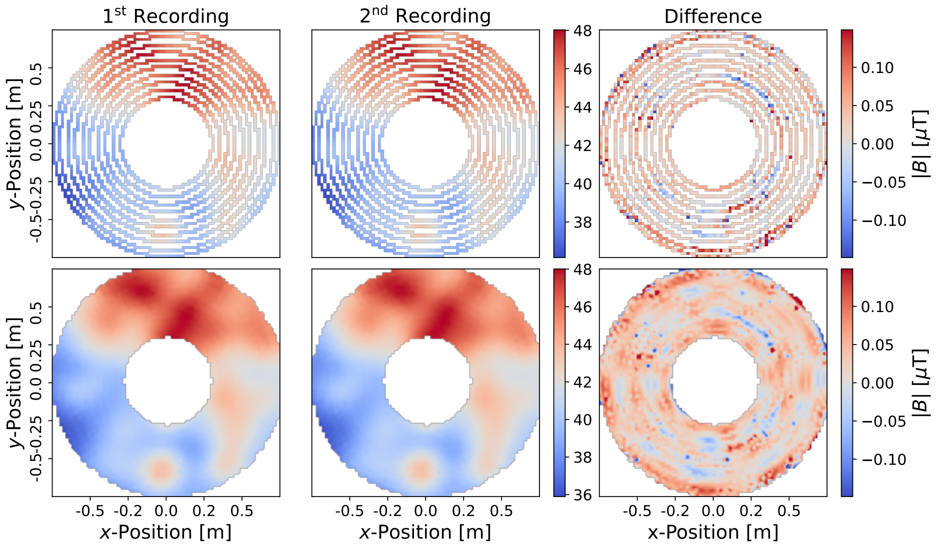

Figure A.8: (*Left Column*) Initial map recording and the resulting interpolated map (20250305_1155). (*Middle Column*) Second recording of the same map, taken five hours after the first recording (20250305_1650). (*Right Column*) Difference in magnetic field strength between the two recordings.

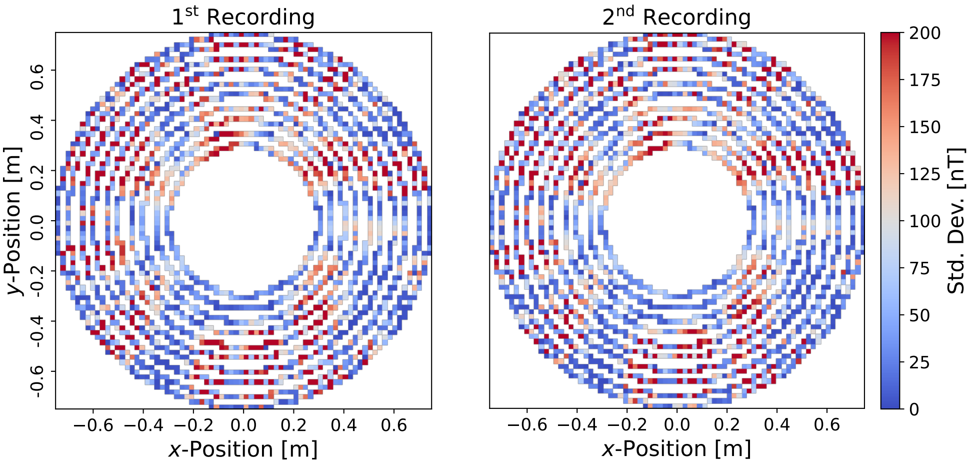

Figure A.9: (*Left*) Standard deviation of the magnetic field measurements that fall within the same pixel of the first map recording (20250305_1155). (*Right*) Standard deviation of the measurements that fall within the same pixel of the second map recording (20250305_1650).

A.4 Magnetic Field-aided Navigation Results

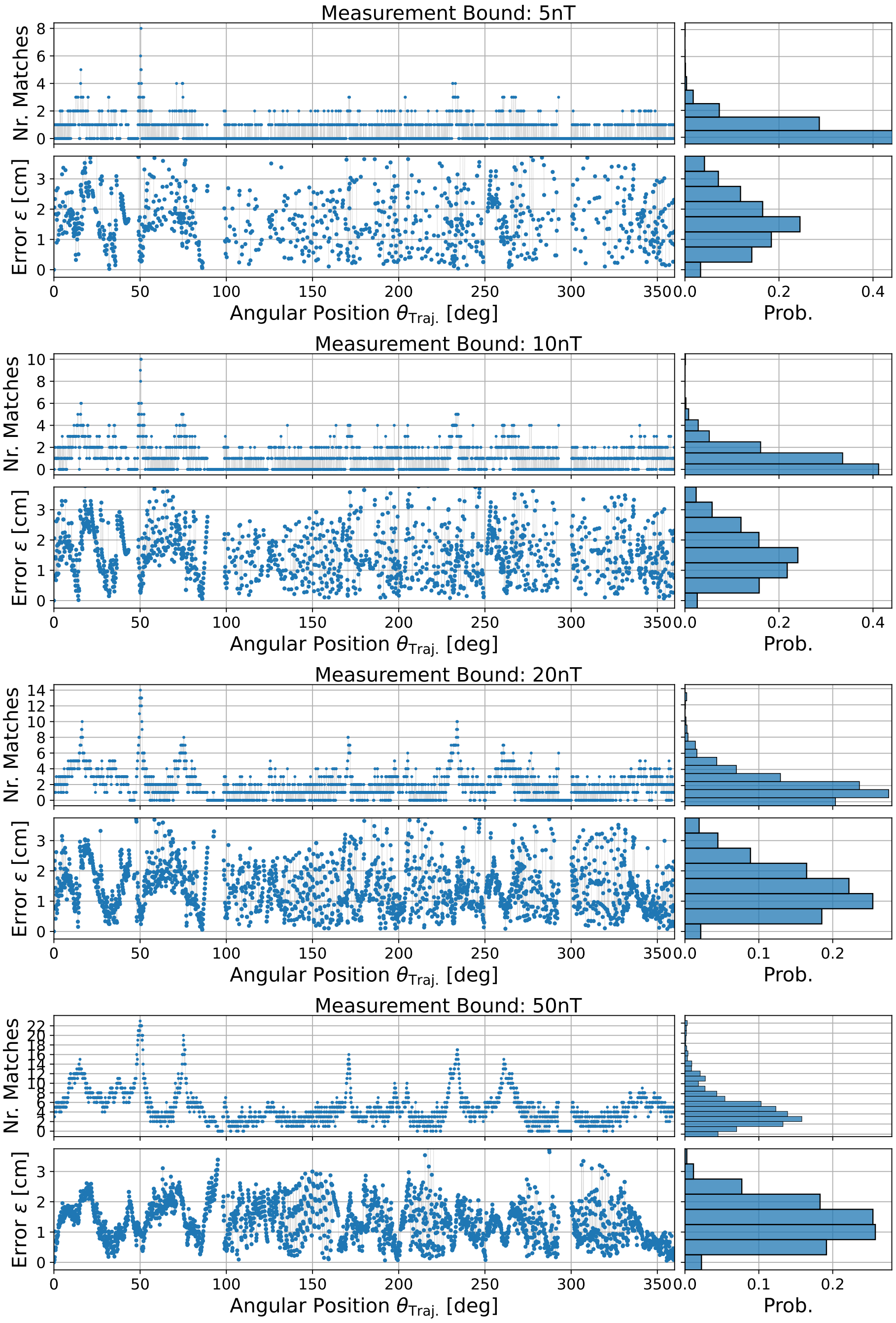

Figure A.10: Results of map matching and the error of the calculated PDA position estimate using real magnetic measurements and the constructed magnetic field map '20250307_0827' under different measurement bounds.

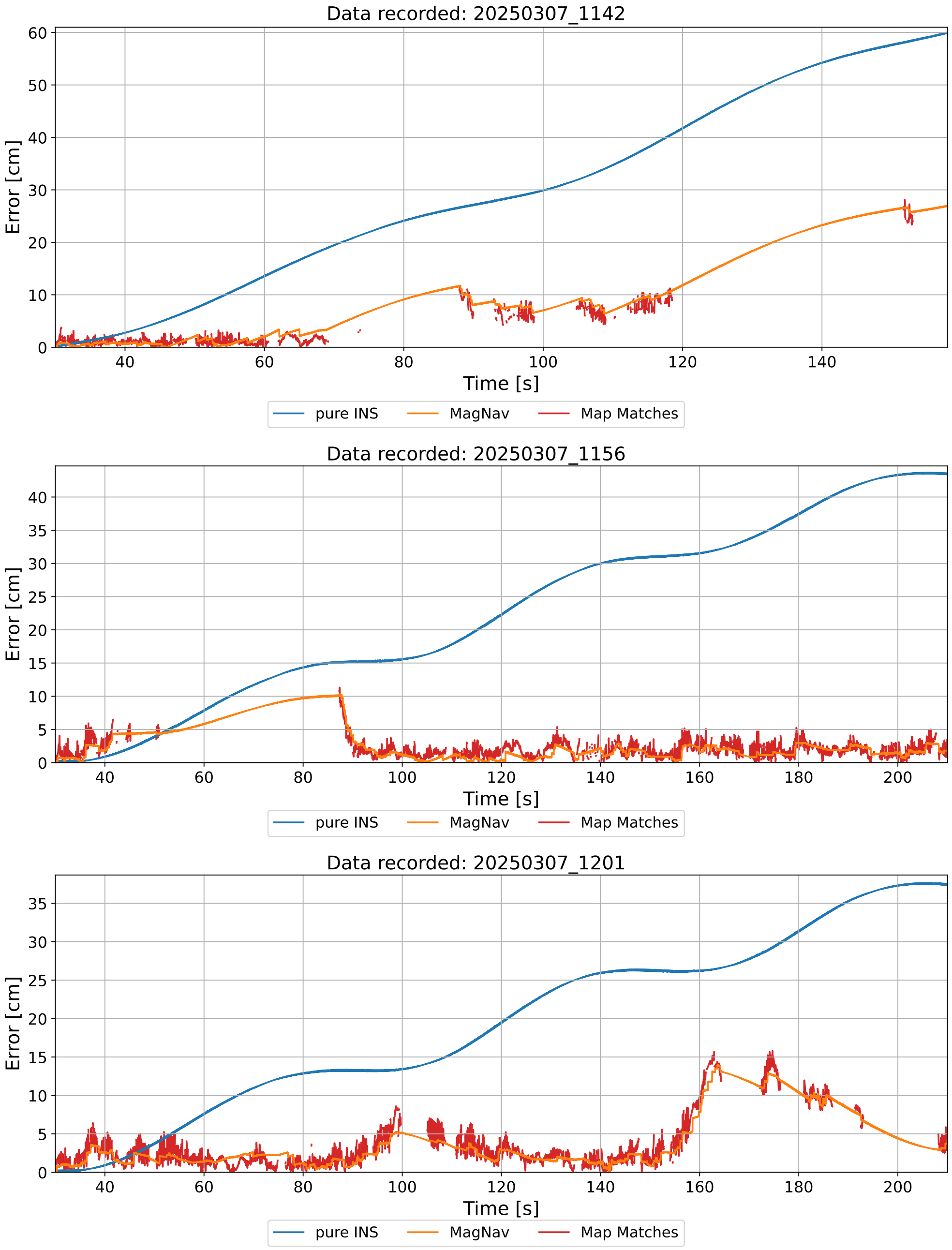

Figure A.11: Error plots of examples using the implemented magnetic field-aided navigation algorithm versus pure INS. The measurements were recorded using the magnet arrangement corresponding to the magnetic field map 20250307_0827.

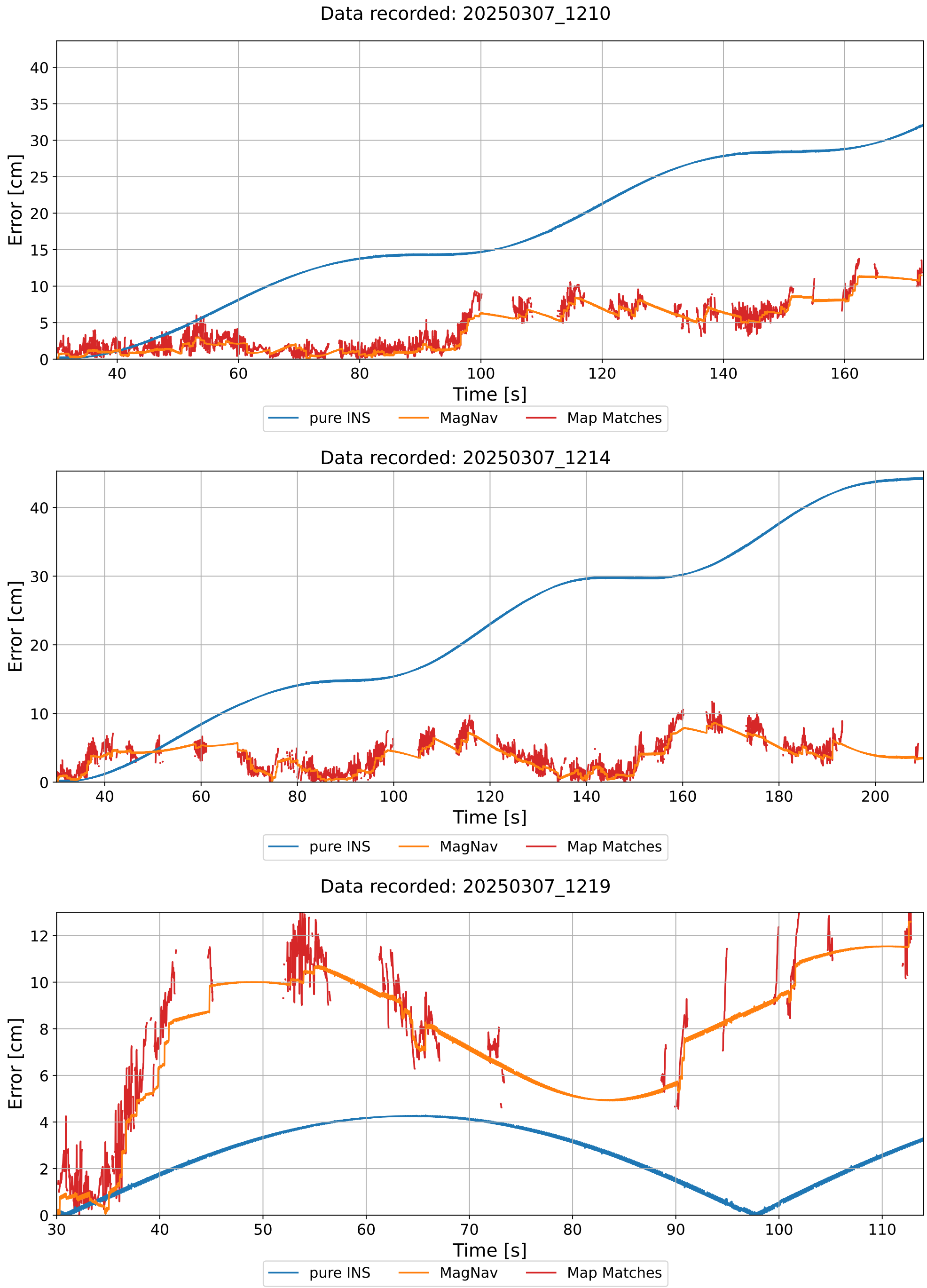

Figure A.12: Error plots of examples using the implemented magnetic field-aided navigation algorithm versus pure INS. The measurements were recorded using the magnet arrangement corresponding to the magnetic field map 20250307_0827.

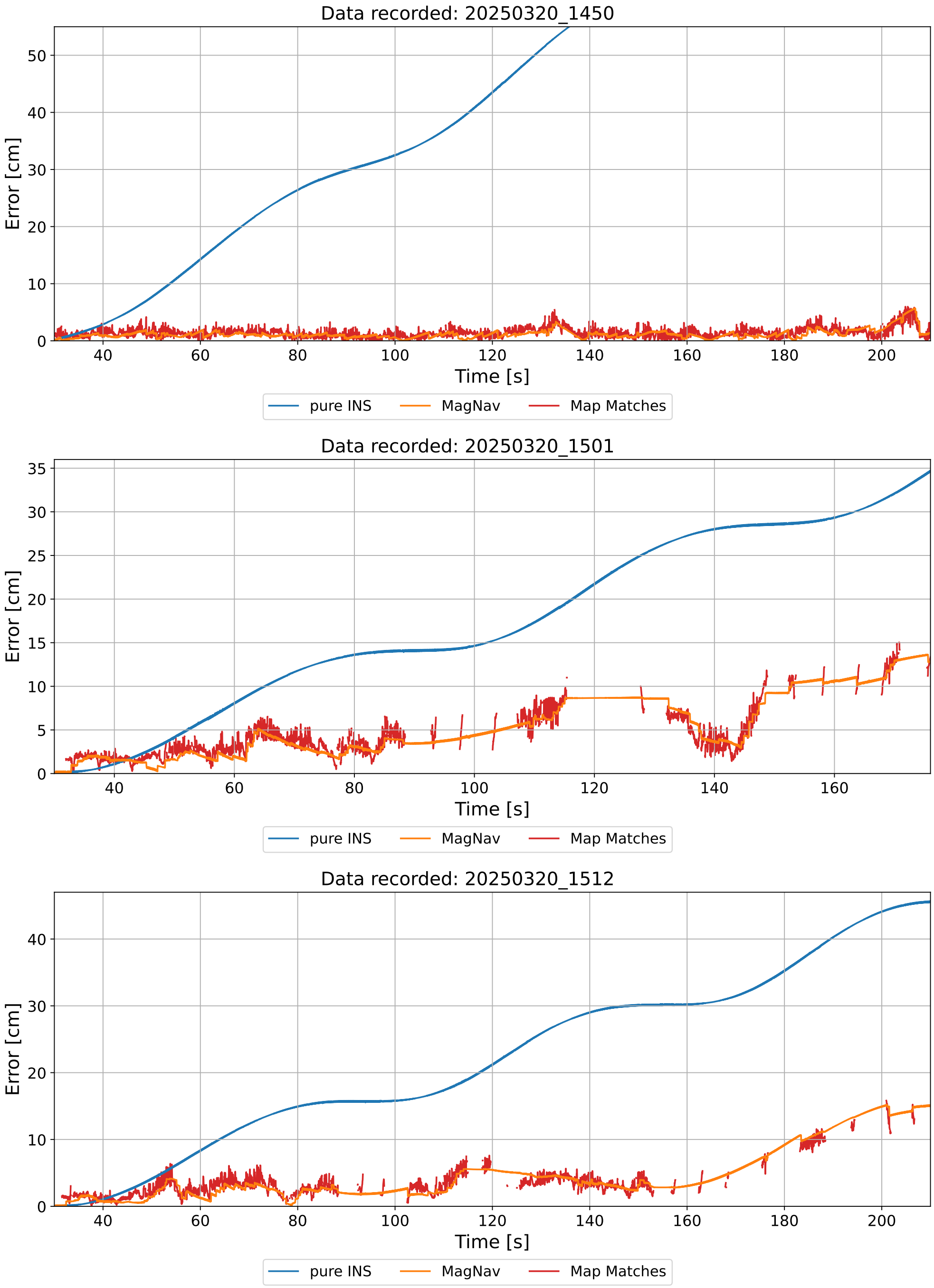

Figure A.13: Error plots of examples using the implemented magnetic field-aided navigation algorithm versus pure INS. The measurements were recorded using the magnet arrangement corresponding to the magnetic field map 20250320_1347.

universität ulm

Eigenständigkeitserklärung für schriftliche Hausarbeiten, insbesondere Abschlussarbeiten

Eigenständigkeitserklärung

Hiermit versichere ich
Name, Vorname: Papadopoulos, Christos,
dass ich die vorliegende Arbeit mit dem Titel

Quantum-Enhanced Correction for Improved Magnetic Field-Aided Navigation
selbständig und ohne unerlaubte fremde Hilfe angefertigt und alle für die Arbeit verwendeten Quellen und Hilfsmittel in der Arbeit vollständig angegeben habe.
Bezüglich der Nutzung von auf künstlicher Intelligenz basierenden Hilfsmitteln (z.B. ChatGPT) versichere ich Folgendes:

Bitte ankreuzen

- ☒ Die Nutzung von KI-basierten Hilfsmitteln wurde von den Prüfenden erlaubt; dabei wurde meine Prüfungsleistung bzw. Teile derselben durch diese Hilfsmittel nicht ersetzt; ich bin darauf vorbereitet, meine etwaige Nutzung von KI-basierten Hilfsmitteln mit entsprechenden dokumentierten Unterlagen wie von den Prüfenden gefordert (z.B. Chatprotokolle) darzulegen, sollte es Klärungsbedarf geben.

- ○ Es ist keine Nutzung von KI basierten Hilfsmitteln erfolgt.

89537 Giengen, 07.05.2025
Ort, Datum

Unterschrift